2020

Quantum Monte Carlo studies of phase transitions

BOSTON UNIVERSITY

GRADUATE SCHOOL OF ARTS AND SCIENCES

Dissertation

QUANTUM MONTE CARLO STUDIES OF PHASE TRANSITIONS

by

PRANAY M. PATIL

B.S., Indian Institute of Technology Madras, India, 2014
M.S., Indian Institute of Technology Madras, India, 2014

Submitted in partial fulfillment of the

requirements for the degree of

Doctor of Philosophy

2020

Approved by

First Reader

Anders W. Sandvik, PhD
Professor of Physics

Second Reader

Claudio Chamon, PhD
Professor of Physics

Acknowledgments

I would like to express immense gratitude towards my advisor Prof. Anders W. Sandvik for guiding me throughout the entirety of my PhD tenure and providing me with plenty of opportunities to present my work. I would also like to thank all my collaborators and thesis committee members, especially Prof. Claudio Chamon, for guiding me on some of the research presented in this thesis. In addition to this, I would like to thank the entire Boston University physics community for their small acts of kindness, which should not go unnoticed. I would like to extend my gratitude to my previous mentor, Prof. Kedar Damle, whose continued guidance throughout the period of my PhD was invaluable, and who was crucial in igniting my interest in this field along with my Master's thesis advisor, Prof. Rajesh Narayanan. Other key members of the condensed matter community who have been kind enough to host me at their respective institutions are Prof. Ribhu Kaul, Prof. Zi-Yang Meng and Prof. Eduardo Mucciolo. I would also like to thank the Sandvik group, which during my stay in Boston, comprised of Adam, Na, Phil, Bowen, Hui, Nvsen, Lu, Jun, Sibin, Kai and Yu-Rong. Of these, Jun, Bowen, Hui, and Nvsen deserve a special thanks for going out of their way in helping me have a comfortable time in China. Beijing was also made ever more pleasant due to Chen and the warm hospitality extended by his mother.

I want to express my special appreciation for my parents, who have always stood by me and understood the knotted and obscure path which many a PhD needs to take. My time in Boston would have been quite lonely without a large group of friends, comprising first and foremost of Nithin, who has also been my faltmate throughout,

Michael and Kaitlyn, who have been great hosts for numerous parties, Alex, Ching-Hao, and Chris, for many meaningful conversations, and Tamiro, Pieter, Matteo, Peco and Shiyu, for the constant companionship. An added acknowledgement must be extended to Nithin and Mohit, who helped me recover from a knee injury, and without whom, that period of my life would have been quite difficult. In addition, I would also like to thank Veronica Funk and the entire team at Boston University physical therapy center for getting me back on my feet after knee surgery, along with Debarati for continuously checking up on me. Instrumental in keeping me in a jovial mood from halfway around the world were my college friends, Manish, Satrajit and Tiru, who have always reminded me of the timelessness of friendship, as well as Shashi, whose constant chatter always created a comfortable sense of warmth. Deserving of mention also is Karthi, who has always made an effort to stay in contact, and was an excellent host in San José. For many honest conversations and shared meals, I would also like to thank Anirudh, Yuki and Mithun. Graduate student life at Boston University was also made more eventful by being a teaching fellow, through which I spent many enjoyable hours working with Nathan and Yilin.

And last but far from the least, I would like to thank Ayushi for being a loyal companion through the final chapter of my graduate school life.

QUANTUM MONTE CARLO STUDIES OF PHASE TRANSITIONS

PRANAY M. PATIL

Boston University, Graduate school of arts and sciences, 2020

Major Professor: Anders W. Sandvik, PhD
Professor of Physics

ABSTRACT

Phase transitions have been an active area of research in statistical mechanics for almost a century and have recently been integrated into quantum mechanics. Many phenomena such as superconductivity and unconventional magnetism are understood to arise from exotic quantum phases and at points describing quantum phase transitions. A detailed understanding of these phase transitions requires numerical simulations of models which benchmark realistic models against theoretical frameworks. The topic of this thesis is the implementation of Quantum Monte Carlo simulation, which is a powerful technique to understand quantum condensed matter, in interesting models to illustrate novel phenomena in magnetic systems. The novel features of condensed matter systems described in this thesis consist of emergent symmetries at critical points, interesting dynamical features of such systems and the drastic effects of defects in spin systems used in the field of adiabatic quantum computing. Emergent symmetries are shown by condensed matter systems especially at critical points and are features which cannot be shown by individual or a small number of spins. Examples of this in one and two dimensions are presented in an early chapter of this thesis. In addition to this, spin systems can show excitations which have an

interesting spatial structure as a consequence of restricted dynamics which only allow the excitations to spread in a particular region. This is presented in the context of a simple model in the following chapter along with numerical support. The following chapter contains a description of adiabatic quantum computing along with a particular model which we study. The phase transition and the effects on the performance of adiabatic quantum computing are studied in this context.

Contents

1 Introduction **1**

1.1 Phase transitions and scaling relations 1

1.2 Overview of spin systems 5

1.3 Basics of Monte Carlo sampling 7

1.4 Extensions to quantum Monte Carlo 9

1.5 Specialization to Heisenberg and Ising systems 12

2 Conformal Field Theory and Emergent Symmetry in 1D **16**

2.1 CFT in 1+1D and predictive power 16

2.2 Ising CFT and benchmarking of features 18

2.3 Verification in trial wavefunction 20

2.4 Emergent symmetry in the Heisenberg antiferromagnetic chain 30

2.5 Measuring Operator Expectation Values in QMC 44

3 Emergent Symmetry in 2D and Unconventional Scaling Behavior **48**

3.1 Continuous symmetries and effects of anisotropy 48

3.2 Quantum Clock Model 50

3.3 Robustness and variants 62

3.4 Details of the Monte Carlo method 66

4 Relationship to Coupled Ising models and Restricted Dynamics **69**

4.1 Fluctuation Coupled Ising Models and Fragmentation 69

4.1.1 Arbitrary Lattice 69

4.1.2 Periodic Chain 74

4.1.3 Fluctuations between blocks and block mixing 79
4.2 Perturbations and Ashkin-Teller Criticality 80
4.3 Relation to Pseudo-first Order Behavior 84
4.4 Using symmetries to design ergodic updates 88

5 Obstacles to Adiabatic Quantum Computing 92

5.1 Quantum adiabatic annealing algorithm: outline and general considerations 92
5.2 k-regular k-XORSAT and lattice embedding 96
5.2.1 The XORSAT problem 96
5.2.2 Lattice embedding 97
5.3 Analytic results: limiting cases and weak-field perturbation theory . . 101
5.3.1 Dilute constraint limit and 2-XORSAT 101
5.3.2 Weak-field perturbation theory: absence of gap collapse 105
5.4 Numerical results 109
5.5 Mapping to the vertex model 115

6 Conclusions 117

A Other Numerical Methods 121

A.1 Exact Diagonalization 121
A.2 Parallel Tempering 122

References 124

Curriculum Vitae 131

List of Tables

2.1 Different loop configurations and their contributions 45

List of Figures

1·1 The behavior of free energy as function of the order parameter for (left) a first order transition and (right) a continuous transition with $t_2 < t_1 < 0$. 3

1·2 The spins on the diamond lattice are traced out first, following which the lattice is redefined. 5

2·1 Scaled spin correlation function, Eq. (2.6), for the critical TFIM on chains of different lengths ($x/L = 0.5$ is the largest separation on a periodic chain). Here we have used $\Delta_\sigma = 1/8$ as that is the scaling dimension of the Ising spin operator (Knizhnik and Zamolodchikov, 1984). 21

2·2 The scaled three-point function for the critical periodic TFIM chain as defined in Eq. (2.8) flows to a constant for $x = L/8$ (left) and $x = L/2$ (right). The line is a guide to the eye and for $x = L/2$, we only exclude data around $y/L = 0.5$ for large sizes as the correlation function vanishes quickly as $x \sim y \sim L/2$ and this means the numerical signal is very weak. 22

2·3 Three point function for the critical TFIM periodic chain scaled using the lattice distance rather than the conformal distance, here for $x = L/8$. 23

2·4 Phase diagram of the APS with a critical curve separating the Néel phase and the VBS phase; this matches well the phase diagram previously reported in Ref. (Lin et al., 2012). 24

2·5 Flow of the Binder cumulant of the APS with κ for different system sizes at $\lambda = 3$. We see here the crossing points for three sets of $(L, 2L)$ (example of extrapolation to critical point shown in inset of Fig. 2·13) and also that B_c becomes negative for large sizes after the crossing point. 25

2·6 EE of the 1D critical APS at $\lambda = 1$ for a periodic chain of $L = 64$ sites. A fit to the form predicted by Eq. (2.12), along with finite size corrections (Xavier and Alcaraz, 2012) causing the visible even-odd oscillations, gave $c = 1.08(4)$. Error bars are of the order of the symbol size. The inset shows the extrapolation of the Binder cumulant crossings points (examples of which are seen in Fig. 2·12), which we have used to extract the critical κ for the infinite system. Here κ_{crit} is 1.519(5). 26

2·7 EE for the 1D critical APS versus the parameter λ, extracted as illustrated in Fig. 2·13. 27

2·8 Dimension of the spin operator in the 1D critical APS graphed vs the short-bond parameter λ. The values were deduced using two- and four-point functions calculated on the critical curve. 28

2·9 Scaled spin correlation functions, defined in Eq.(2.6), plotted against the separation as a fraction of the system size for the critical APS at $\lambda = 1$ (where $\kappa_{\text{crit}} = 1.519$). The inset shows the ratio $R(0.5, 0.2)$ Eq. (2.13), of the correlations at two distances. 29

2·10 Scaled dimer two-point function for the critical JQ_2 periodic chain as defined in Eq. (2.38). The results flow to a constant with increasing size. The Horizontal axis only extends to $x/L = 0.5$ as two-point functions are symmetric about $y = L/2$. 37

2·11 Spin two-point function for the critical JQ_2 chain scaled with the first term of Eq. (2.35) [as explicitly shown in Eq. (2.39)]. The approach to a constant for large sizes confirms the expected form. 38

2·12 Spin two-point function for the critical JQ_2 chain with the first term of Eq. (2.35) subtracted out and scaled with the second term, as in Eq. (2.40). We see improving agreement with the expected form with increasing L. 39

2·13 The Dimer three-point function for the critical JQ_2 chain vanishes for large enough system size, which agreement with Eq. (2.33), here shown for $x = L/4$ and $x = L/2$. 40

2·14 The scaled dimer-spin-spin three-point function, Eq. (2.41), for the critical JQ_2 flows to a constant, here demonstrated for $x = L/4$ and $x = L/2$. In the upper panel, the divergence at $y = 3L/4$ is due to the exact vanishing of the correlation function at this point. In the lower panel, data for even y values in the range $y/L \in (0.3, 0.7)$ have been excluded as $\langle \mathbb{D}_0 \vec{\mathbb{S}}_x \cdot \vec{\mathbb{S}}_y \rangle$ tends to a "0/0" form and, thus, the scaled correlation function is very noisy. 41

2·15 Overlap of two singlet states (left and right projection) creates a loop diagram. 45

2·16 Loop diagrams for six site correlation function with sites represented by crosses, different permutations of site numbers lead to different contributions 47

3·1 Histograms for the magnetization as a function of tuning parameter s. The critical value is $s_c = 0.2402(1)$. These simulations were carried out on a 48×48 square lattice. 49

3·2 Binder Cumulant U_m for $q = 3$. The negative peak shows a potential first order transition. The inset shows the scaling of the negative peak value with $1/L$ fit to the form $f(L) = a/L^b$ with $b = 1.95(4)$. 54

3·3 Binder Cumulant U_m for $q = 4$ shows a weak first order transition. The negative peak appears at sizes larger than 16x16. 55

3·4 Binder Cumulant U_m for $q = 5$. The monotonic behavior of U_m is evidence of a continuous transition. 56

3·5 Binder Cumulant U_m for $q = 6$. The monotonic behavior of U_m is evidence of a continuous transition similar to the $q = 5$ case and the crossing points for different sizes can be seen here. 57

3·6 Flow diagram for $q = 6$ (ϕ_q vs U_m) showing flows approaching the XY fixed point followed by the Z_q fixed point. The stable point (0,0) is marked here along with the unstable points (0.532,0) and (1,0). . . . 59

3·7 ν calculated using the Binder Cumulant crossing method as a function of $1/L$. Fit to $f(x) = aL^{-\omega} + 1/\nu(\infty)$ with values for ω and $1/\nu(\infty)$ taken to be the 3D XY values. 61

3·8 $1+\eta$ calculated using the Binder Cumulant crossing method as a function of $1/L$. Fit to $f(x) = a/L^b + c$ leads to $\eta(\infty) = 0.07(1)$ for $q = 5$ and 6. 62

3·9 Δ_ϕ calculated using the Binder Cumulant crossing method as a function of $1/L$. Fit to $f(x) = a/L^b + c$ leads to $\Delta_\phi(\infty) = 2.3(3)$ for $q = 6$ and $\Delta_\phi(\infty) = 1.4(4)$ for $q = 5$. 63

3·10 Δ_{dw} calculated using the ratio of domain wall energies for pairs of sizes $(L, 2L)$ for varying L. We see that the $\Delta_{dw}(\infty) = 2.17(6)$ for $q = 6$ and $\Delta_{dw}(\infty) = 2.27(5)$ for $q = 5$. 64

3·11 s_c calculated using the Binder Cumulant crossing method as a function of $1/L$. Fit to $f(x) = aL^{-\omega} + s_c(\infty)$ leads to $s_c(\infty) = 0.14087(4)$ using $\omega = 0.8$ for the 3D Ising model. 65

3·12 Orientational order parameter u as a function of inverse size at the critical point for soft clock model with 8 background states. 66

3·13 Updates which are local in space switch the states along a particular imaginary time string. Filled squares denote the transverse field operator and and the unfilled squares denote the identity operator. Rectangles are ferromagnetic operators. 67

4·1 The four states at a particular site break into two non-communicating axes as shown above, leading to the Hilbert space breaking into many distinct axis arrangements. 70

4·2 An axis arrangement for the square lattice with interacting sites connected by dotted lines. 71

4·3 Axis arrangements sorted by energy with reference blocks making up the lowest energy region and energy increasing bottom to top. 74

4·4 Average size of the largest piece in a block plotted as a function of the system size N and fit to the form $\langle n \rangle \approx a + b \log(N)$ with $b = 1.33(1)$. Inset: The probability distribution of the size of the largest piece, which shows an exponential tail. 75

4·5 Energy levels for the Hamiltonian defined in Eq. (4.1), as a function of tuning parameter s, seen to converge in $s = 0$ limit and approach the spectrum of the classical Ising chain in $s = 1$ limit. Inset: The level diagram around $s = 0.5$ shows a minimum gap of ≈ 0.34. 77

4·6 Binder cumulant as a function of s with crossing points showing approximate locations of the two transitions at $p = 0.95$. P stands for the polarization and M for the magnetization. Crossing points of U for large sizes approximate critical points for these transitions. 82

4·7 Phase diagram of the model described by Eq. (4.3) with phases I. paramagnet, II. polarization ordered and III. ferromagnet with the AT line of continuously varying exponents from $p = 0$ to $p \approx 0.75$. Inset: Polarization exponent $\Delta_{\sigma\tau}(1/L)$ for $p = 0.5$ extrapolated to $\Delta_{\sigma\tau}(0) = 0.20(1)$. 84

4·8 The minimum value of U_m at $p = 0.95$ as a function of N fit to the form $a + bL^{-c}$ converges to 1.02(3). Inset: U_M as a function of tuning parameter s for various system sizes. The thermodynamic from of U_M is shown by the dashed line. 87

4·9 Order parameter histogram as a function of the tuning parameter s. Top: The 2D histogram of M_x and M_y. Bottom: Marginal probability distribution of M_x at corresponding values of s. 88

4·10 Binder ratio for the 2D $q = 4$ Potts model shows a peak at the transition, as shown here for a 256×256 system. Inset: Value of the peak as a function of inverse size fit to a function of the from $f(x) = 3 - ax^b$. 89

4·11 Cluster size as a function of s shows the development of large clusters in the ordered phase. 90

5·1 Cartoon phase diagrams in the temperature-transverse field parameter space for two scenarios that may occur in the application of the SA and QAA algorithms to the solution of computational problems. In the scenario of panel (a), SA meets a transition to a glassy phase at $T = T_g$, whereas QAA encounters a first-order quantum phase transition at $h = h_g$. Dashed line indicates a putative phase boundary that terminates at the two critical points on the axes. Panel (b) depicts the case where there is no bulk classical thermodynamic phase transition to a glass phase, but the obstruction of a first-order quantum phase transition nevertheless remains. 94

5·2 (a) Lattice representation of 3-regular 3-XORSAT instance with 8 variables and 8 clauses as a 8×8 lattice of CNOT and SWAP gates. There are 4 bits coupled by a gate at each position of the lattice, as shown in (b). The variable bits x_i record the solution of the problem upon termination of a protocol that reaches the ground state. Upper and lower boundary states are forced by a strong field that favors the uniform bit states shown. (b) Sketch of couplings between bits in each of the gates. Lines denote ferromagnetic bonds in the spin representation and grey triangle represents the 3-spin term in Eq. (5.5b). The formula for the 3-XORSAT instance shown here is $(x_2 \oplus x_3 \oplus x_6) \wedge (x_5 \oplus x_7 \oplus x_8) \wedge (x_1 \oplus x_2 \oplus x_6) \wedge (x_3 \oplus x_4 \oplus x_7) \wedge (x_1 \oplus x_5 \oplus x_8) \wedge (x_3 \oplus x_4 \oplus x_6) \wedge (x_1 \oplus x_2 \oplus x_8) \wedge (x_4 \oplus x_5 \oplus x_7)$. 100

5·3 (a) "Backbone" loop for a $k = 2$ instance of k-regular k-XORSAT in the lattice representation. SWAP gates are omitted and CNOT gates are denoted by $\times$ symbols. Arrows indicate the "unraveling" procedure described in the text. (b) The corresponding unraveled loop picture with spin chains radiating out of CNOT gates. Domain walls are sketched as | symbols and their movement, indicated by the arrows, heals broken bonds and reduces energy. 104

5·4 (a) Lattice representation of 3-regular 3-XORSAT instance with the same backbone as the one shown in Fig. 5·3(a). The backbone cannot independently fluctuate between positive and negative values, due to constraining couplings to spins outside the backbone (example shown in red), and hence the backbone cannot be isolated as in the $k = 2$ case. (b) Loop equivalent for the $k = 3$ realization, with arrows showing domain wall movement that in this case involves branching of domain walls at CNOT gates. 105

5·5 (a) Sketch of y-bond connecting the spins of two gates. The state of this bond only affects the four perturbation correction terms corresponding to the spins shown as filled circles. (b) Flipping the control spin (X) of a CNOT gate switches the state of the bonds marked with a cut. Along the vertical line, either the upper or lower bond can be broken (upper bond shown here). 106

5·6 Illustration of two TFI chains coupled at their center by a CNOT gate. The boundary spins of the vertical chain are fixed. 111

5·7 Magnetization histograms for the transverse field system shown in Fig. 5·6 with 81 spins per chain (crosses) and 321 spins per chain (stars), as obtained from QMC calculations at $h = 1$. As J increases (a-f), the average magnetization switches values without developing a strong double peak structure even for large size. 112

5·8 (a-f) Magnetization histograms for a single realization of the 2-XORSAT lattice with size 6×6 (crosses) and another with size 16×16 (stars) for increasing J. The slight asymmetry in the two peaks of the histograms may be caused by non-ergodicity issues in the QMC simulation. (g) Binder cumulant for 20 realizations of size 16×16. In all panels $h = 1$. 113

5·9 (a-f) Magnetization histograms for a single realization of the 3-regular 3-XORSAT lattice with size 6×6 (crosses) and another with size 16×16 (stars) for increasing J. (g) Binder cumulant for 20 realizations of size 16×16. In all panels $h = 1$. 114

5·10 Illustration of the mapping of the lattice formulation of k-XORSAT onto the general vertex model framework for computational problems introduced in (Chamon et al., 2017), here shown for a 4×4 lattice. The grey shaded area is the placeholder in which a lattice like the one shown in Fig. 5·2(a) plugs into after a $\pi/4$ rotation. In this embedding, clause bits (blue) are fixed and variable bits (red) are left free at both left and right boundaries, whereas all bit lines are "reflected" at the top and bottom boundaries (dashed lines). 115

Chapter 1

Introduction

1.1 Phase transitions and scaling relations

Collections of identical interacting entities form much of the world which we engage with on a daily basis. Most of these systems share common universal features which are especially evident in the physics governing changes in phase. Universal behavior of physical quantities at phase transitions helps us gain a concise understanding of the relevant features. Perhaps the most common examples of this phenomenon are seen in the phase changes of water, the development of charge or magnetic order in solid state materials, the onset of superconductivity and transitioning behavior of bacteria in changing environments. For a large set of phase transitions, a particular symmetry can be identified which differentiates between different phases. For example, in the case of water changing phase from liquid to solid, continuous translation and rotation symmetries are broken as ice forms a lattice structure which can only be rotated or translated by discrete quantities to get back the same structure. This phenomenon is called symmetry breaking and can be quantified using a quantity called the order parameter which is sensitive to development of a symmetry broken phase. In addition to the order parameter, clear signatures of the phase transition can also be detected in quantities such as the energy, correlation length and susceptibility or compressibility. An understanding of phase transitions is generally developed using the concept of thermodynamic free energy, which is formulated as a functional over the possible configurations which the system can host. The configurations which minimize this

functional dictate the phase of the system as they would have the highest Boltzmann weights. For a thermodynamic system, the free energy is defined in continuous space and the detailed functional form of the order parameter which minimizes it can be calculated in some cases. Once this is done, the particular function of the order parameter can be plugged into the free energy functional which leads to a free energy function which now depends on external parameters such as temperature T and pressure P. We illustrate this process for a sample case under the mean field approximation. This approximation assumes that the order parameter has no dependence on space, which reduces the free energy functional to just a function, and allows us to perform calculations in a very simple manner. Assuming for simplicity that the phase transition is only tuned by T and using the knowledge that the order parameter ψ is small at the critical temperature T_c and should vanish for $T > T_c$, the free energy density, or the Landau-Ginzburg functional (Landau, 1937), can now be written as

$$\Phi(T, \psi) = \Phi_0(T) + (a(T)\psi^2 + b(T)\psi^4 + c(T)\psi^6 + ...). \tag{1.1}$$

There are two types of commonly observed phase transitions, namely first-order and continuous, which derive their names from the behavior of the free energy at the critical point. First order transitions show a jump in the order parameter value as a consequence of structure of the free energy. In the context of Eq. (1.1), a possible way to generate these two cases is as follows. For a continuous transition, using $b(T_c) > 0$ and $a \propto (T - T_c)$, the location of the free energy minimum moves smoothly away from zero and thus the order parameter is continuous in T. For a first order transition, we use $b(T_c) < 0$ and $a(T_c) > 0$, such that there are three minima and T tunes the free energy values at these minima. In this way, the location of the global minima jumps from zero to a finite value without passing through intermediate values. Both of these scenarios are made explicit in Fig. 1·1. It is important to note that the first

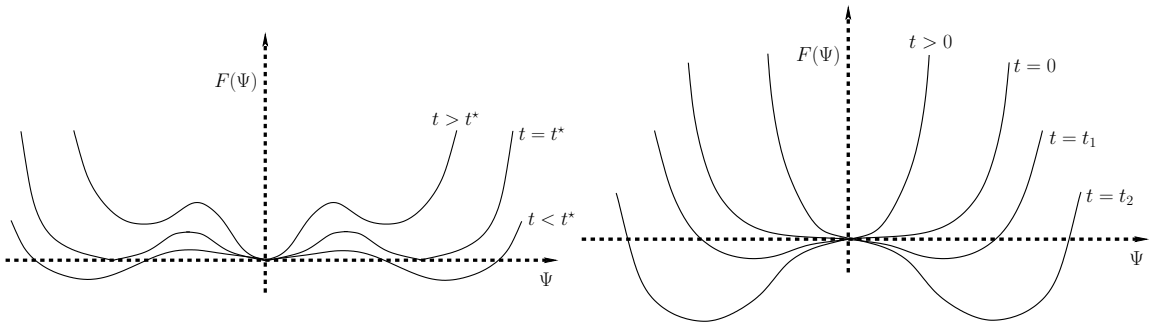

Figure 1·1: The behavior of free energy as function of the order parameter for (left) a first order transition and (right) a continuous transition with $t_2 < t_1 < 0$.

order transition does not occur at T_c, but at $T < T_c$, leading to a finite t as shown in Fig. 1·1. The term critical temperature is usually used only for continuous transitions.

The Landau-Ginzburg functional can be solved to get the behavior of ψ as a function of temperature. This yields the correct behavior in the mean field limit, which means that we ignore spatial correlations. For large dimensional systems the mean field approximation works well as all to all connections between sites on a lattice can be perfectly represented by an average field. The lowest dimension up to which the mean field approximation yields accurate results is called the upper critical dimension. In dimensions below this limit, this analysis provides a qualitative understanding but more sophisticated methods are required to work out exact details. Continuous phase transitions are of special interest as they show exotic scale invariant behavior and are characterized by scaling exponents which control various quantities which can be studied experimentally. These are called critical exponents and sets of these sort varied systems into a relatively small number of universality classes. Some of the critical exponents which are generally used to identify these classes are

$$\xi \approx t^{-\nu}, \tag{1.2}$$

$$M \approx t^{\beta}, \tag{1.3}$$

$$\chi \approx t^{-\gamma}, \tag{1.4}$$

$$C \approx t^{-\alpha}, \tag{1.5}$$

where $t = (T - T_c)/T_c$ is the reduced temperature, which is defined with respect to the critical temperature T_c, ξ is the correlation length, M is the order parameter, χ is the susceptibility and C stands for the specific heat. Of the properties discussed above the one most relevant to numerical simulations is the scaling of the correlation length, as it sets a natural length scale in the system. As simulations must be carried out on finite systems, a technique must be developed to read critical exponents at finite size. This is done by arguing that a finite system can only access physics which occurs at a length scale shorter than the system size L. From this size, an equivalent correlation length can be calculated by using $\xi \sim L$ and $t \sim L^{-1/\nu}$. This leads to a rewriting of the criticality equations as a function of L and this can then be used to extract exponents from finite size scaling analysis.

Another crucial idea used to understand critical phenomena is called renormalization group analysis (Wilson, 1971). This analysis is used to understand the behavior of systems at very large scale by building it up from the smallest scales. An example is presented here for the classical Ising model on a square lattice where each site hosts a spin which can take two possible values, +1 and -1, and a Hamiltonian given by

$$H = -J \sum_{\langle i,j \rangle} \sigma_i \sigma_j, \tag{1.6}$$

where J is the relevant energy scale with respect to $k_B T$, which is set to unity. The partition function is given by $Z = \sum_c e^{-H(c)}$, where c runs over all possible configurations. We can perform a sequential calculation of the partition function by summing over certain sites in the square lattice (as shown in Fig. 1·2). The renormalization step involves rewriting the Hamiltonian in terms of the remaining

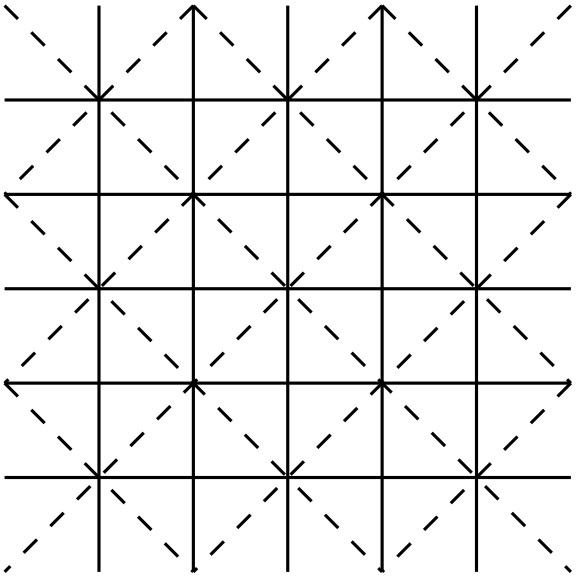

Figure 1·2: The spins on the diamond lattice are traced out first, following which the lattice is redefined.

spins at a new energy scale J'. This is achieved by first expressing the sum over configurations as $\sum_{\sigma_1}\sum_{\sigma_2}\sum_{\sigma_3}...$ and then performing the sums for the spins on the diamond-like lattice shown in Fig. 1·2. Following this, the Hamiltonian can be written again as in Eq. (1.6) where the interactions are now between nearest neighbors on the remaining diamond-like lattice with a $J' = \frac{1}{2}\ln(\cosh(4J))$ under the Migdal-Kadanoff approximation which ignores longer range interactions which are created under this process as well.

1.2 Overview of spin systems

In this thesis, we are going to focus on phase transitions seen in magnetic systems which are made of spin-1/2 magnetic moments. These are relevant models for insulating magnetics where the electronic degrees of freedom are frozen. The non-commuting nature of the Pauli matrices which describe a spin-1/2 magnets leads to interesting competition between phases hosted by many body systems made out of these entities.

We are interested in studying ground state phase transitions for these models where the physics is driven by quantum fluctuations.

The first class of models which we use in this thesis are called antiferromagnetic Heisenberg models, which have Hamiltonians made out of terms of the form $-\vec{S}_i \cdot \vec{S}_j$ where (i, j) represent lattice sites. These Hamiltonians have an SU(2) symmetry associated with them as all the spins in the systems can be rotated through an arbitrary angle in 3D without altering any of the terms as they are all dot products. When we consider just one such term between two sites which are isolated from the rest of the system, it is easy to see that the state that minimizes the Hamiltonian is a singlet given by $\frac{1}{\sqrt{2}}(|\uparrow_i\downarrow_j\rangle - |\downarrow_i\uparrow_j\rangle)$. It is instructive to compare this to the classical ground state which would be expected from this Hamiltonian, which would require both spins to point in opposite directions and the direction can be chosen arbitrarily. At the level of just two spins, it is easy to see the stark difference between the classical and quantum ground states and appreciate the effects of quantum fluctuations. These ground states are significantly altered once a competition is included by considering a large number of interacting sites. An easy illustration of this would be the case of three sites labeled 0,1 and 2 with a Hamiltonian $H = \vec{S}_0 \cdot \vec{S}_1 + \vec{S}_1 \cdot \vec{S}_2$ which cannot be minimized term by term due to a shared site between the terms. Many such competing terms make up many body magnetic systems and in many cases there is no clear way to determine the ground state properties of such systems. These are relevant experimentally as well because many magnets are described by these Hamiltonians. A couple of examples of simple ground states which we discuss in this thesis are the Néel state and the Valence Bond Solid (VBS). The Néel state is similar to a classical antiferromagnetic state where neighboring spins align in opposite directions and this is seen for some lattice arrangements where the geometry allows this state to partially satisfy all bonds. The VBS state is a product state of singlets

where each site participates in one and only one singlet and which leads to a lack of magnetic order. There are a plethora of interesting states other than these and we study some of these in the following chapters.

The second class of models we consider are transverse field Ising models, which are generally made out of a classical piece encoding a two body term of the form $\sigma_i^z \sigma_j^z$ and quantum fluctuations generated by σ_i^x. Depending on the lattice and the coefficients chosen for the classical terms, the ground state in the classical limit can show long range magnetic order. In the presence of a strong transverse field this order is washed out and we get a quantum paramagnet. The Hamiltonian usually has a two fold (Z_2) symmetry which is broken by the ordered phase as the system spontaneously chooses one of the two directions to order in. These kinds of Hamiltonians describe systems which have strong anisotropy along a particular direction, defined as the z-axis, leading to interactions along that direction. In many cases, there are complete theoretical descriptions of the phase transitions in these models and the phenomena seen in these models can be mapped on to classical Ising models in one higher dimension.

1.3 Basics of Monte Carlo sampling

Monte Carlo simulations are used to calculate averages from complex probability distributions which are difficult or impossible to handle analytically. They are used widely in science and engineering disciplines. The Monte Carlo algorithm (Newman and Barkema, 1999) starts with the system in some given initial state, which is specified by the user and will be irrelevant for simulations with large number of steps. At each step the system transits from the current state to a new state chosen using a fixed transition probability. If the transition probabilities are chosen correctly, as shown in the next paragraph, the Monte Carlo process will visit each state with the

correct probability for that state. The probability of a state S in a system evolving with time can be defined as the ratio of the number of steps for which the state was S to the total number of steps taken during the simulation (P(S)=n_s/n_{tot}).

To calculate averages, we do appropriate measurements at each step of the simulation and calculate the average. As each state is generated with the correct probability, the Monte Carlo average must be equal to the statistical average for large number of steps as shown below for some observable O, i.e, $\lim_{n\to\infty} \langle O \rangle_{MC} = \langle O \rangle$.

We start with some initial state μ, and transit to a new state ν using some mechanism which is specific to the model we are studying with some probability $P(\mu \to \nu)$. This probability must satisfy

$$\sum_{\nu} P(\mu \to \nu) = 1. \tag{1.7}$$

As the probabilities of individual configurations is fixed by the Boltzmann distribution, we can say that this is a stable probability distribution, i.e the probabilities do not change with time. If the Monte Carlo engine is working correctly, every configuration produced must have its correct Boltzmann weight. The two conditions above imply that for any given state, the net flux out of that state must equal the net flux in to ensure that the probability density for that state remains unchanged. This reduces to a condition of the form

$$\sum_{\nu} [P(\mu \to \nu)p(\mu) - P(\nu \to \mu)p(\nu)] = 0. \tag{1.8}$$

One of the simpler solutions to this equation called the detailed balance condition and is given by the following constraint relation between the transition probabilities and the Boltzmann probabilities;

$$\frac{P(\mu \to \nu)}{P(\nu \to \mu)} = \frac{p(\nu)}{p(\mu)}. \tag{1.9}$$

The Monte Carlo simulation uses this relation to fix the transition probabilities. For our Monte Carlo simulations to be truly trustworthy, the results should be completely independent of the initial state in which the simulation was started. To ensure this we allow the Monte Carlo engine to warm up a little before we actually start doing measurements. During this warm up, the algorithm goes through a predetermined number of steps which are sufficient to lose all memory of the initial state.

In general, it is not practical to propose transitions form a particular state to all possible other states as most states have a relatively small probability in the stable probability distribution. Instead, specific moves may be proposed to ensure that the system samples all high probability states. In the case of the Ising model described in the previous section, a popular updating method used in the Metropolis update, which picks a particular spin to flip with a probability given by the detailed balance condition. This update proposes a new state which is similar to the current state and thus ensures that its probability is not drastically different.

1.4 Extensions to quantum Monte Carlo

Quantum systems host highly non-intuitive states due to the non-commuting nature of the operators involved. The path integral formalism developed by Feynmann is a powerful tool to extract the properties of these states. For small systems it is usually possible to calculate the path integral exactly but various approximations need to be used to treat many body systems. Quantum Monte Carlo simulation provides a powerful method to numerically calculate the path integral to high accuracy using stochastic sampling of the space time configurations which make up the path integral. Here we describe formulations of this method which make no approximations and are used to extract ground state and thermodynamic behavior as well as a QMC method to calculate observable expectation values for variational wavefunctions.

We first review the stochastic series expansion (SSE) method (Sandvik, 2010b) for carrying out QMC simulations. This method is capable of accessing the complete path integral encompassing all quantum and thermal fluctuations and in this way is well suited to study thermal and quantum phase transitions. Calculating observable expectation values requires us to evaluate $\langle O \rangle = \mathrm{Tr}[Oe^{-\beta H}]/Z$, which can be extracted directly while sampling the space time configurations making the partition function $Z = \mathrm{Tr}[e^{-\beta H}]$. This can be achieved by first expanding the exponential in the form

$$e^{-\beta H} = \sum_{n=0}^{\infty} \frac{(-\beta)^n}{n!} H^n \tag{1.10}$$

and inserting complete sets of states ($\sum_\alpha |\alpha\rangle \langle\alpha|$) using an orthonormal basis of choice. This results in an expression for the partition function of the form

$$Z = \sum_{n=0}^{\infty} \frac{(-\beta)^n}{n!} \sum_{\alpha_0} \sum_{\alpha_1} \sum_{\alpha_2} ... \langle\alpha_0| H |\alpha_1\rangle \langle\alpha_1| H |\alpha_2\rangle ... \langle\alpha_{n-1}| H |\alpha_0\rangle . \tag{1.11}$$

A particular term in the above summation is often called a space-time configuration as $e^{-\beta H}$ is similar to evolution in imaginary time. As H itself is made out of a collection of operators, each term in $\langle\alpha_i| H |\alpha_{i+1}\rangle$ takes each of these operators and each term within the summations over n and $\{\alpha\}$ can be seen as an operator string which evaluates to a particular number. Exact enumeration of these operator strings is not possible and can be done using stochastic sampling under the Monte Carlo method. This yields high quality results for a variety of systems. For any system with a finite spectrum and for a finite value of β, the length of the operator strings converge due to the factorial suppression in longer strings. This implies that there are no approximations to the partition function evaluation under this scheme. The SSE method treats general β but can also be used to extract ground state features of finite systems by choosing $\beta \gg 1/\Delta$, where Δ is the energy gap between the ground state and the first excited state. The gap is in general expected to be finite for any

finite system size.

A slightly simpler formulation of SSE has been developed for studying ground state physics called projector QMC which works by projecting the ground state out of a trial wavefunction $|\psi_t\rangle$. For this procedure to work, one must ensure that all the eigenenergies have the same sign with the ground state having the largest magnitude. This is easy to do for most finite systems by globally shifting the Hamiltonian through a constant. Once the Hamiltonian has been modified in this manner, the ground state can be written as $|\psi_0\rangle = \lim_{m\to\infty} H^m |\psi_t\rangle$ for the purpose of calculating observable expectation values. In practice, the value of m which is used depends on the gap. These statements can be substantiated by expressing the trial state as $|\psi_t\rangle = \sum_i c_i |\phi_i\rangle$, where $\{\phi\}$ denotes the eigenbasis with eigenenergies $\{E\}$, and observing that

$$\frac{\langle\psi_0|O|\psi_0\rangle}{\langle\psi_0|\psi_0\rangle} = \frac{\langle\psi_t|H^m O H^m|\psi_t\rangle}{\langle\psi_t|H^m H^m|\psi_t\rangle} = \frac{\sum_i \sum_j c_i c_j O_{ij} E_i^m E_j^m}{\sum_i c_i^2 E_i^{2m}} = \frac{\sum_i \sum_j c_i c_j O_{ij} \left(\frac{E_i}{E_0}\right)^m \left(\frac{E_j}{E_0}\right)^m}{\sum_i c_i^2 \left(\frac{E_i}{E_0}\right)^{2m}}. \tag{1.12}$$

As we have already set the ground state energy to be the largest in magnitude, the only terms that survive the summations for large m in the right most term of Eq. (1.12) are the ones with $i = 0, j = 0$. In this way the calculated quantity equals O_{00}, which is the expectation value in the ground state.

QMC methods are also used to understand the accuracy of trial wavefunctions developed for highly complex many body systems. As it is often impossible to analytically or numerically extract the exact ground state wavefunction and properties for such systems, trial wavefunctions are proposed which can be further fine tunes based on how well they describe the true properties of the ground state. In many cases, the trial wavefunctions themselves are not tractable and their features may be extracted using stochastic sampling. The trial wavefunction can be written as $|\psi_t\rangle = \sum_i c_i |\phi_i\rangle$ in some basis of choice $\{\phi\}$. The expectation value of some observable can be now

written as

$$\langle O \rangle = \frac{\sum_i \sum_j c_i c_j O_{ij}}{\sum_i c_i^2}, \tag{1.13}$$

and can be calculated stochastically as exact enumeration would be too time consuming.

Many Hamiltonians and trial wavefunctions used in the field of frustrated magnetism cannot be efficiently simulated using the procedures described above due to a complication called the sign problem. This condition arises when the coefficients preceding the operator strings have mixed sign structure and the distribution cannot be directly interpreted as a probability distribution. In this case, the average sign needs to be factored out to get the actual operator expectation values. This process usually requires a number of Monte Carlo steps exponential in the system size and quickly becomes impractical. In some cases, the sign problem can be completely eliminated or drastically reduced by choosing an appropriate basis to represent the system in. Trivial ways of eliminating the sign problem can also be implemented by adding constants to the Hamiltonian and this procedure must be carried out during the design of the QMC simulation.

1.5 Specialization to Heisenberg and Ising systems

Most of the Hamiltonians studied in this thesis fall in the Heisenberg or Ising symmetry classes. For the simple Heisenberg and transverse Ising model, we review the details of implementing QMC techniques described in the previous section. We begin with Heisenberg systems on bipartite lattices as these simulations can be tackled without the sign problem. The analysis presented here is in the context of spin-1/2 local moments but can be generalized to higher spin as well. SSE is developed usually in the z-basis, as it provides a convenient orthogonal basis in which operators are easy to express. In this formalism it is difficult or impossible to measure expectation values

of certain important operators which are not diagonal in the z-basis. An example of this would be the correlations of the singlet projection operator $(1/4 - \vec{S}_i \cdot \vec{S}_j)$, which is essential to diagnose valence bond solid order. In the ground state, a different basis can be used to access such off-diagonal operators through projector QMC. This is the basis of all bipartite singlet covers, where each state is a product state of singlets such that each site belongs to a singlet. Expressing this state in the z-basis and evaluating inner products between different singlet covers reveals that this basis is overcomplete and thus cannot be used in a method such as SSE. In projector QMC, we can begin with any state which has a non-zero overlap with the ground state and in the case of the singlet basis, we begin with a uniform superposition of all singlet covers and carry out the QMC in a combined singlet-z basis. The operators in the Hamiltonian must now be formulated in this singlet language so that their action on the singlet covers is clear. Consider an antiferromagnetic Heisenberg model with Hamiltonian $H = \sum_{\langle i,j \rangle} \vec{S}_i \cdot \vec{S}_j$, where $\langle i, j \rangle$ are some predefined pairs of lattice sites. To build an operator string with a pair of states sandwiching it, a z-basis state is chosen which is consistent with the projection boundary singlet cover states and operators in the string are chosen based on the z-basis state. For example, the diagonal operator $(S_i^z S_j^z + 1/4)$ only acts on sites i and j if they have opposite spins. The off-diagonal operator $(S_i^+ S_j^- + S_i^- S_j^+)$ also enforces the same condition and flips both spins. The Monte Carlo simulation begins from a valid operator string and updates it based on moves which move the diagonal operators and implement exchanges between diagonal and off-diagonal operators through flipping operations along closed loops as this respects the constraints for a valid operator string configuration. This process generates operator configurations with the appropriate weights in an ergodic manner leading to efficient sampling. Diagonal operators can be directly measured now from the configurations in the z-basis without considering the singlet basis. It is important

to note that in the singlet basis, only the operator $\vec{S}_i \cdot \vec{S}_j$ occurs, as it is the SU(2) invariant version. This operator acts as a singlet projection operator, generating a singlet between sites i and j. For off-diagonal operators, we construct left and right states starting from the singlet configurations on the ends using $\langle\psi_l| H^m$ and $H^m |\psi_r\rangle$ respectively. The state is built by following the operators along the operator string and making appropriate changes to the state when an operator is passed in the string. In the event that the operator acts on sites i and j which are already connected by a singlet, the singlet projection operator does not change the state. Sites that belong to different singlets get connected by a singlet and their partner spins form another singlet. This can be seen by observing the action of $\vec{S}_i \cdot \vec{S}_j$ on a state having singlets on pairs $\{i,k\},\{l,j\}$:

$$P_{ij} \left|...\{i,k\},\{l,j\}...\right\rangle = \frac{1}{2} \left|...\{i,j\},\{l,k\}...\right\rangle . \tag{1.14}$$

Here $P_{ij} = 1/4 - \vec{S}_i \cdot \vec{S}_j$ is the exact projection operator and the above relationship can be confirmed by expanding both sides in the z-basis. After traversing the operator string from the left and right ends, the projected singlet states can be assumed to be drawn from the ground state manifold, and measurements can be carried out using these. To calculate quantities such as spin correlation functions, the singlet states must be first expressed in the z-basis and an overlap calculated, which lists the z-basis states permitted by both states. This set of z-basis states can then be used to calculate expectation values in the z-basis, such as $S_i^z S_j^z$. For off-diagonal operators, more complicated manipulations of the overlap diagram between the singlet states must be carried out and this is illustrated in chapter 2.

Next we turn to the transverse field Ising model, where the QMC algorithm closely mimics the treatment of the classical Ising model. Our basis of choice for this model

is the z-basis, and the Hamiltonian is this basis can be written as

$$H = -J \sum_{\langle i,j \rangle} \sigma_i^z \sigma_j^z - h \sum_i \sigma_i^x. \tag{1.15}$$

σ_i^x acts on a z-basis by just flipping the spin at site i. This Hamiltonian is studied on various lattices, and in some cases it is difficult to find efficient updates for the QMC simulation. One way of designing the operator string in this model is by adding $-h \sum_i I_i$, which is the identity operator acting on site i, to the Hamiltonian. Now the operator string can be built using combinations of these three types of operators. A particular operator string can be broken up into clusters, which are defined in the following manner. If two sites in the space-time configuration are connected by $\sigma_i^z \sigma_j^z$, they must be part of the same cluster and if two points are on opposite sides of the σ_i^x or I_i operators, then they are uncorrelated. Using these rules, one can construct clusters of spins and operators which can be flipped independent of other clusters. This method along with metropolis style updates for operators which are diagonal in the z-basis, allow us to efficiently sample space-time configurations for some simple lattices. For frustrated lattices or operators made out of more than two σ^z operators, this cluster building algorithm leads to clusters which are either too small or too big, thus leading to inefficient sampling. We will discuss some methods of getting around this in later chapters.

Chapter 2

Conformal Field Theory and Emergent Symmetry in 1D

2.1 CFT in 1+1D and predictive power

Field theories are in general useful descriptions for large scale features at phase transitions. In the case of classical phase transitions they result from a coarse graining in momentum space using renormalization group flows. For quantum phase transitions, field theories can be written down in a space which is one dimension higher than the quantum system, using a coarse graining of the path integral. In this chapter, we will restrict ourselves to 1+1D quantum systems, where the +1 stands for the extra dimension associated with the path integral, or 2D classical systems. For such systems, conformal field theory (CFT) proves to be a powerful analytical technique. Conformal symmetry requires translation, scaling, rotational and inversion symmetries. In 2D, the first three automatically guarantee the fourth. 2D classical systems which possess the above properties and 1D quantum systems with a dynamic exponent of 1, which implies that imaginary time scales in the same manner as space, qualify for conformal symmetry at the critical point. It is also important to note that this theory treats local systems, which is in general true for physically relevant systems.

A 2D CFT is defined on the complex plane and the constraints that conformal symmetry requires restricts the two and three-point correlation functions of primary

operators to behave as (Di Francesco et al., 1997):

$$\langle O_i O_j \rangle \sim \frac{\delta_{ij}}{|z_{ij}|^{\Lambda_i \Lambda_j}}, \tag{2.1a}$$

$$\langle O_i O_j O_k \rangle \sim \frac{1}{|z_{ij}|^{\Delta_{ij}} |z_{jk}|^{\Delta_{jk}} |z_{ki}|^{\Delta_{ki}}}, \tag{2.1b}$$

where O_i are the primary operators of the CFT and Λ_i are their scaling dimensions and $\Delta_{ij} = \Lambda_i + \Lambda_j - \Lambda_k$. The scaling dimension of a primary operator is made up of two numbers h_i and $\bar{h}_i$ which indicate the scaling in z and $\bar{z}$ respectively. These correlation functions can be factorized into two pieces, where one depends on z, and the other on $\bar{z}$ and the Λ_i's are replaced by $h_i(\bar{h}_i)$. This is useful when $h_i \neq \bar{h}_i$, which may be the case for current operators, which generate translations in either z or $\bar{z}$. For operators with $h_i = \bar{h}_i$, we do not mention each of them separately, but only indicate the total scaling dimension $\Lambda_i = h_i + \bar{h}_i$.

As these relations are valid on the infinite complex plane and our simulations are done on a periodic chain, we must use a mapping from the cylinder to the infinite plane to understand the correlation functions. In our simulations, we use ground state projector QMC simulations, which means that we project on a trial state with a large number of Hamiltonians, effectively for a long imaginary time. This implies that we are using a cylinder whose circumference is the system size and length is infinite for all practical purposes. The system can then be mapped to the infinite plane through the transformations $\tau \to r$ and $x \to \theta$ (Calabrese and Cardy, 2004) which results in two spatially separated points on the periodic chain having a conformal distance between them of

$$|z_{ij}| = L \sin\left(\pi \frac{x}{L}\right), \tag{2.2}$$

where x is the separation on the ring. This substitution into the correlation functions on the plane tells us what we should expect on the cylinder. In some cases, the

correlation function on the plane may have different dependence on z and $\bar{z}$ and may not be expressible in $|z|$, but the mapping to the cylinder correlation functions reverses this (Di Francesco et al., 1997; Calabrese and Cardy, 2004) and they only depend on the conformal distance given by Eq. (2.2), which must be the case as they are real. Conformal information has also been used to aid fitting of correlation functions and other numerical quantities for spin systems (Fáth, 2003; Arita and Motegi, 2011; Lake et al., 2005). The conformal structure of Potts models has also been investigated using three-point functions (Delfino et al., 2013). As we will see, the SU(2) spin chains considered here have additional complications when interpreting multi-point functions.

2.2 Ising CFT and benchmarking of features

In this section, we will present the results from 2D CFT in the context of the periodic critical Ising chain, which has a Hamiltonian of the form

$$H = -\sum_i \sigma_i^z \sigma_{i+1}^z - \sum_i \sigma_i^x. \tag{2.3}$$

This Hamiltonian can be written in terms of Majorana fermions in the continuum as follows (Boyanovsky, 1989):

$$H = \frac{1}{2}\Big(- i\frac{\partial \psi_R(x)}{\partial x}\psi_R(x)\Big) - \frac{1}{2}\Big(- i\frac{\partial \psi_L(x)}{\partial x}\psi_L(x)\Big). \tag{2.4}$$

In general this Hamiltonian should also have a mass term, but it disappears at criticality, leaving H invariant under scaling. From the Hamiltonian we see that the equations of motion imply that the two fermions are completely disconnected (due to the absence of a mass term) and thus it is sufficient to study just one of them.

Here we will check that the functional form of the three-point function matches the CFT prediction for the TFIM as we will be using three-point functions in the

next section to point out features of the extended symmetry. The CFT of the TFIM is made up of three primary operators, namely the identity I, the spin σ and the ferromagnetic part of the energy density ϵ, with scaling dimensions 0, 1/8 and 1 respectively (Belavin et al., 1984; Knizhnik and Zamolodchikov, 1984). We can first check the two point correlation function $C_2(s) = \langle \sigma_0 \sigma_x \rangle$, which should behave as

$$C_2(x) \propto \left(\frac{1}{L \sin(\pi x/L)} \right)^{2\Lambda_\sigma}, \tag{2.5}$$

To make the functional dependence expressed there more explicit in graphs, we define the correlator scaled by the conformal distance as

$$C_{sc}(x) = \left(L \sin\left(\pi \frac{x}{L} \right) \right)^{2\Lambda_\sigma} C_2(x). \tag{2.6}$$

If $C_2(x)$ follows Eq. (2.5), the scaled correlation should be a constant with respect to the distance x. As shown in Fig. 2·1, we find that the scaled spin correlation function indeed converges to a constant, even for relatively small system sizes (indicating small scaling corrections in this case), and to good precision except for $x/L \approx 0$ (and signs of convergence even when $x \to 0$ are seen when the system size grows).

For these operators, the non-vanishing three-point function with the smallest scaling dimension is $\langle \epsilon\sigma\sigma \rangle$. We also note here again that the CFT only tells us the behavior of the connected three-point function and due to this, we compare the CFT expectation to $\langle \epsilon\sigma\sigma \rangle_c = \langle \epsilon\sigma\sigma \rangle - \langle \epsilon \rangle \langle \sigma\sigma \rangle$. We will not carry the subscript c for connected correlation functions as they make the symbolic expressions cumbersome.

Using the conformal distance and Eq. (2.1b), the three-point correlation function on the ring should be

$$\langle \epsilon_0 \sigma_x \sigma_y \rangle \sim \frac{\left[L \sin\left(\pi \frac{|y-x|}{L} \right) \right]^{\frac{3}{4}}}{\left[L \sin\left(\pi \frac{x}{L} \right) \right] \left[L \sin\left(\pi \frac{y}{L} \right) \right]}. \tag{2.7}$$

To compare numerical data to this expression, we define a scaled correlation function

$C_{sc}(x, y)$ which is the raw correlation function multiplied by the inverse of the expected form as shown below:

$$C_{sc}(x, y) \sim \langle \epsilon_0 \sigma_x \sigma_y \rangle \times \frac{\left[L \sin\left(\pi \frac{x}{L}\right)\right]\left[L \sin\left(\pi \frac{y}{L}\right)\right]}{\left[L \sin\left(\pi \frac{|y-x|}{L}\right)\right]^{\frac{3}{4}}} \tag{2.8}$$

If the expression matches, we should expect the scaled correlation function to be a constant as a function of x and y. In Fig. 2·2, we plot the scaled correlation function for two different values of x and the whole range of y. For large sizes, we observe an approach to constant behavior, with the deviations occurring when two out of the three operators are close to each other and, therefore, the coarse grained description does not hold.

It is important to note here that we must use the conformal distances when predicting the finite-size functional form due to the cylinder to plane conformal transformation that we have used. We can also define the scaled correlation function using just the lattice distances instead of the conformal distance as

$$C_{sc}(x, y) \sim \langle \epsilon_0 \sigma_x \sigma_y \rangle \times \frac{[s(0, x)][s(0, y)]}{[s(x, y)]^{\frac{3}{4}}}, \tag{2.9}$$

where $s(a, b)$ is the shortest distance between a and b along the ring. This way of defining the scaled correlator results in a disagreement with the expected constant form for the scaled correlation function, as can be seen in Fig. 2·3, although the curves for different sizes still show data collapse as the correct scaling dimension is being used even in this correlator.

2.3 Verification in trial wavefunction

The Amplitude Product State is a wavefunction of the resonating valence bond type on a bipartite lattice (Lin et al., 2012; Liang et al., 1988). Here we define it in 1D,

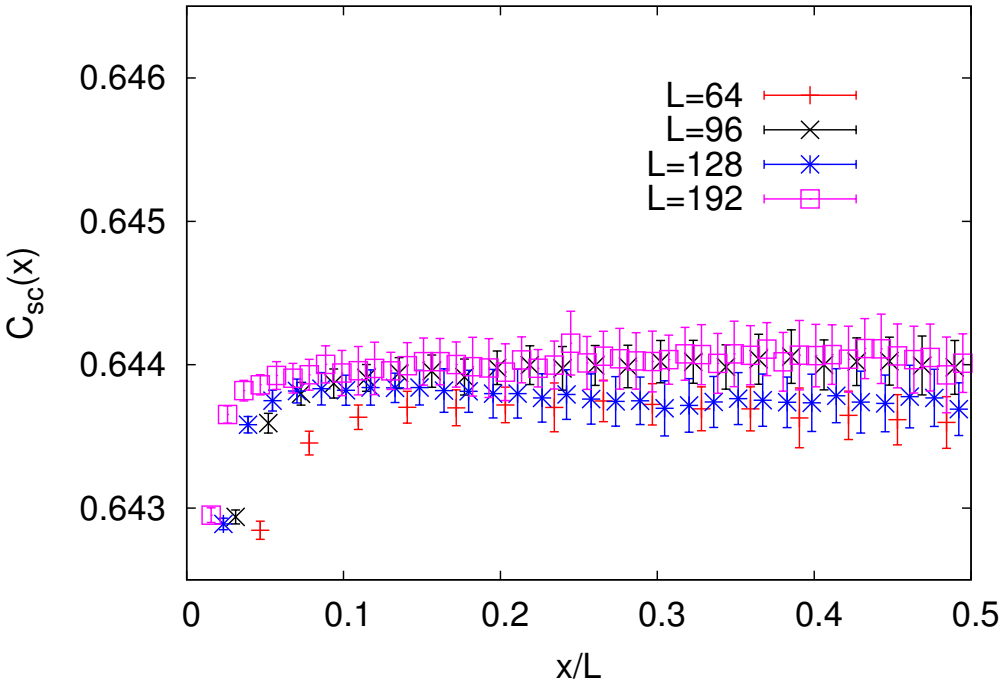

Figure 2·1: Scaled spin correlation function, Eq. (2.6), for the critical TFIM on chains of different lengths ($x/L = 0.5$ is the largest separation on a periodic chain). Here we have used $\Delta_\sigma = 1/8$ as that is the scaling dimension of the Ising spin operator (Knizhnik and Zamolodchikov, 1984).

using parameters λ and κ, as a superposition of valence-bond states as,

$$|\Psi(\lambda,\kappa)\rangle = \sum_i A_i(\lambda,\kappa)|V_i\rangle, \tag{2.10}$$

where $|V_i\rangle$ is a tiling of $N_b = L/2$ two-spin singlets between the A-sites and the B-sites on the 1D periodic chain, and it contributes with a weight A_i to the APS. The weight is given by an amplitude-product depending on the bond-lengths present in $|V_i\rangle$;

$$A_i = \prod_{j=1}^{N_b} h(d_j), \qquad h(d) = \begin{cases} \lambda, & d = 1, \\ d^{-\kappa}, & d > 1. \end{cases} \tag{2.11}$$

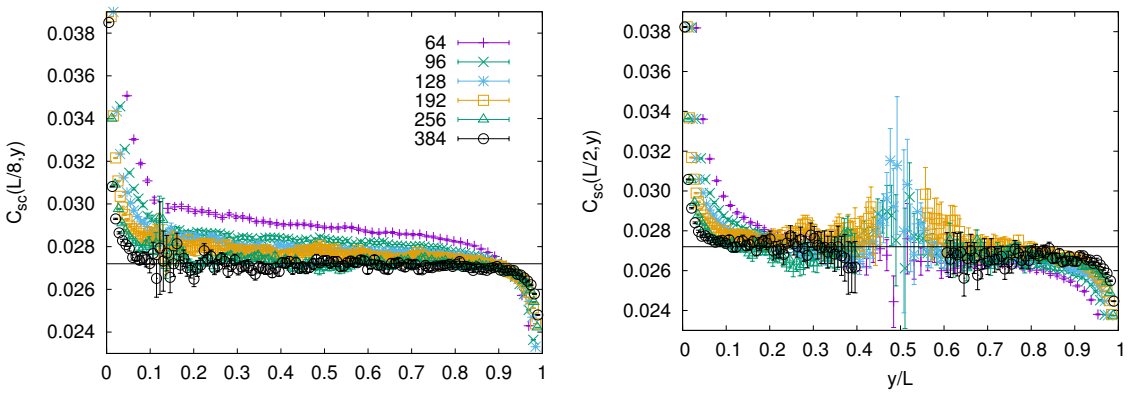

Figure 2·2: The scaled three-point function for the critical periodic TFIM chain as defined in Eq. (2.8) flows to a constant for $x = L/8$ (left) and $x = L/2$ (right). The line is a guide to the eye and for $x = L/2$, we only exclude data around $y/L = 0.5$ for large sizes as the correlation function vanishes quickly as $x \sim y \sim L/2$ and this means the numerical signal is very weak.

It should be noted that the asymptotic properties of the state are not controlled only by the asymptotic power law, as might be naively expected, but also by the short-length weights which are important in this regard (Beach, 2009).

We have here chosen a very simple parameterization that allows us to study the effects of both asymptotic and short-length amplitudes, as in Refs. (Lin et al., 2012; Beach, 2009). For $\kappa \to 0$ and $\lambda \approx 1$ all valence-bond coverings contribute equally and we obtain a long-range ordered Néel state, whereas for $\kappa \to \infty$ we have only two contributing components, each with short bonds on alternating spin pairs, i.e., two degenerate dimerized states. In (λ, κ) space we have a critical curve, $\kappa_{\rm crit}(\lambda)$, separating these two phases, as shown in Fig. 2·4. The critical spin and dimer exponents vary continuously on this curve (Lin et al., 2012). All our scaling results for the correlators were obtained for parameter values falling on this critical curve, and we have improved the estimation of this curve over Ref. (Lin et al., 2012) by going to larger chain lengths. Measurements in the valence-bond basis are done by following the mapping to loop estimators developed in (Beach and Sandvik, 2006). To avoid

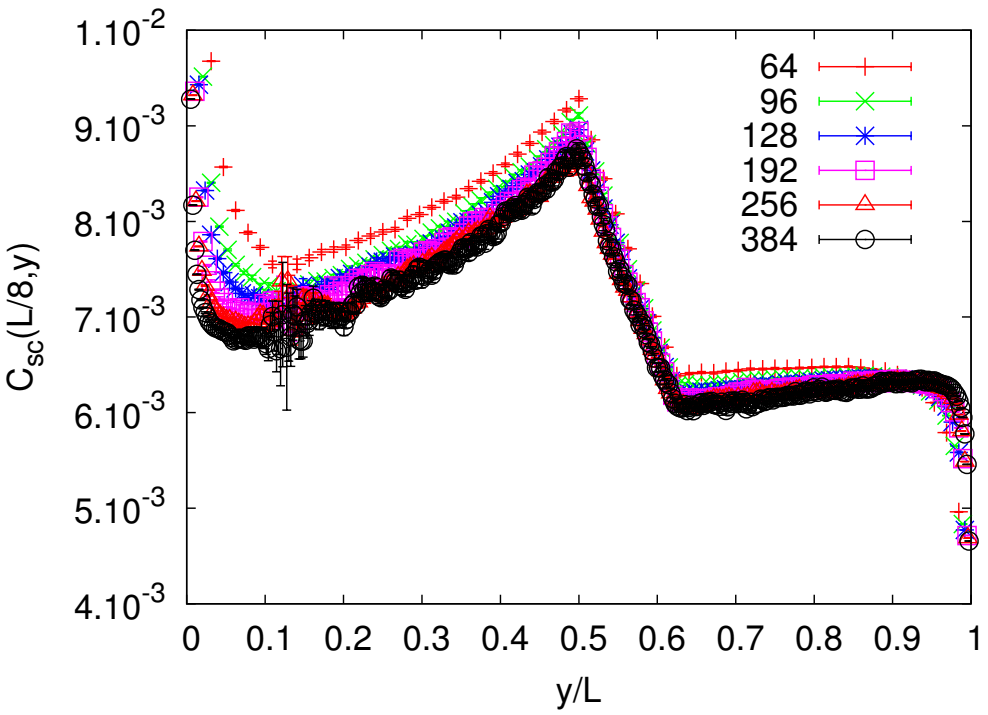

Figure 2·3: Three point function for the critical TFIM periodic chain scaled using the lattice distance rather than the conformal distance, here for $x = L/8$.

getting locked into winding sectors at large λ, we have also introduced simultaneous updates for identical singlets in the bra and ket configurations (Patil et al., 2014) which considerably improves the sampling efficiency.

We extract crossing points using the Binder cumulant at a particular value of λ, as shown in Fig. 2·5, and estimate the critical dimension of the spin operator by looking at the flow of the exponent with chain length. We also see that the Binder cumulant becomes negative for $\kappa \approx \kappa_{\text{crit}}$ and large system sizes (it approaches 0 for larger κ). A negative Binder cumulant is often taken as an indicator of a first-order transition, but for that purpose one also has to check that the negative peak value grows as the system volume. Rigorous examples exist of more slowly divergent negative peaks at continuous transitions Ref. (Jin et al., 2012), and, as indicated by our results, the APS may provide yet another example where this may be the case.

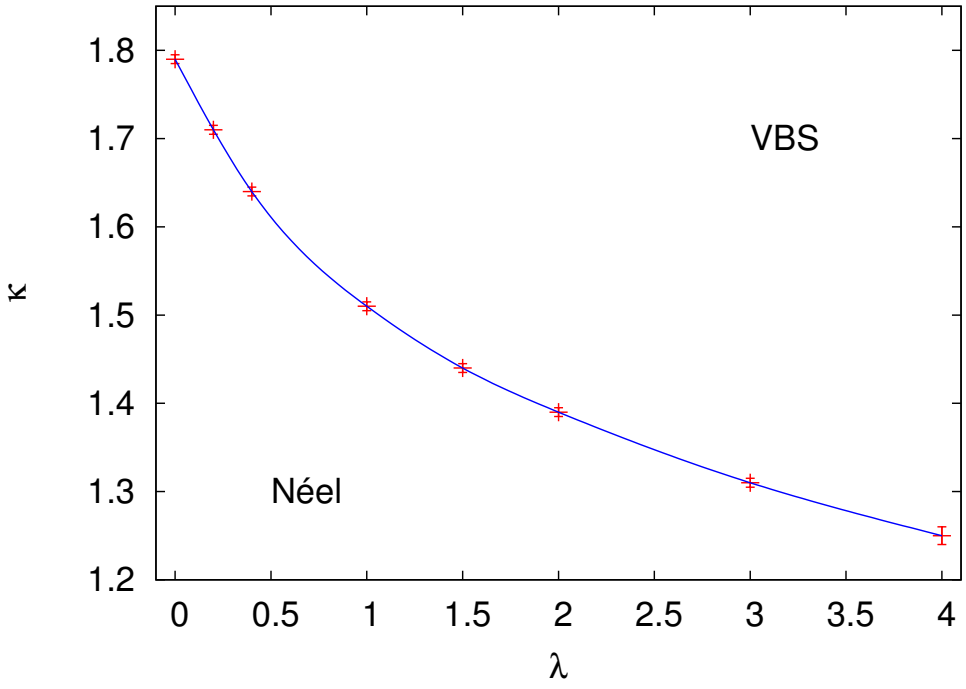

Figure 2·4: Phase diagram of the APS with a critical curve separating the Néel phase and the VBS phase; this matches well the phase diagram previously reported in Ref. (Lin et al., 2012).

Next we consider the entanglement entropy (EE) of the APS, using the second Renyi variant $S^2(l_A)$, which is accessible in simulations using the swap operation and the ratio trick (Hastings et al., 2010). We find that the EE follows a profile identical to what we would expect from a CFT (Calabrese and Cardy, 2004) on a circle (shown for half a periodic chain in Fig. 2·13), i.e., the EE depends on the size of the entangled region (l_A) as follows:

$$S^2(l_A) = \frac{c}{4} \log \left[\frac{L}{\pi a} \sin \left(\frac{\pi l_A}{L} \right) \right] + d, \tag{2.12}$$

where L is the total system size, and a is the nearest-neighbor distance (set to 1 in our case). This form can be derived from the general form for the nth Renyi entropy (Calabrese and Cardy, 2004). The constant d is different for odd and even sizes and

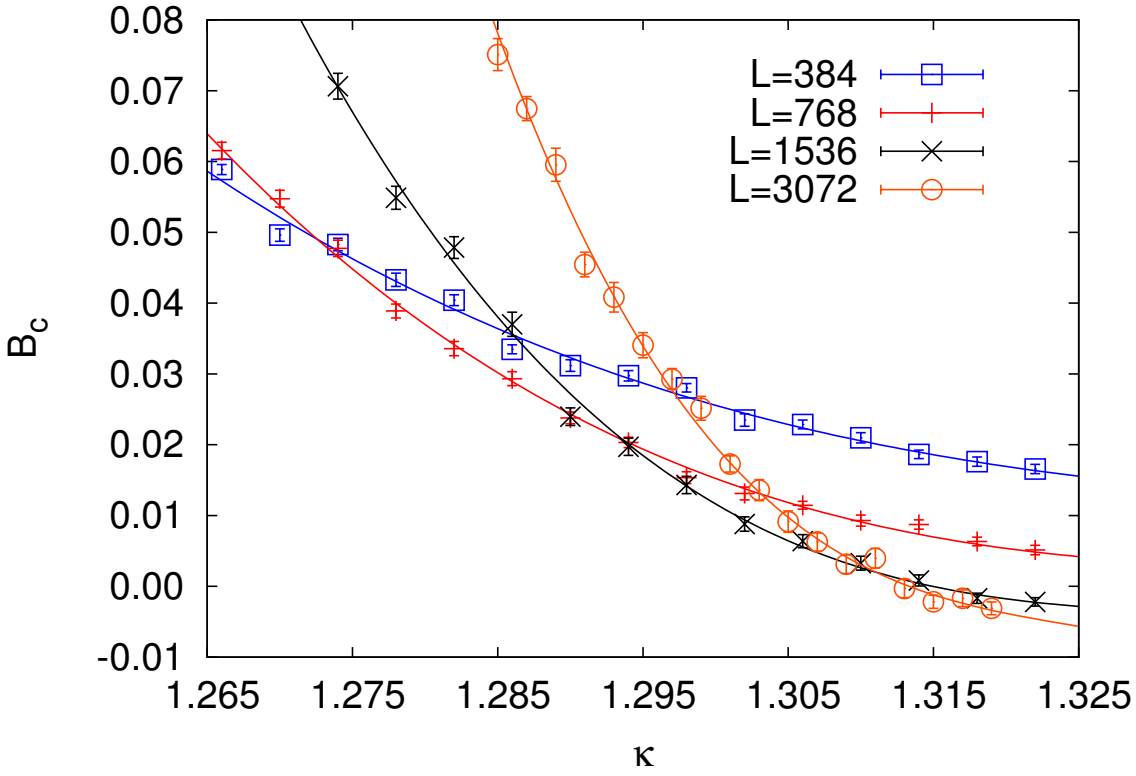

Figure 2·5: Flow of the Binder cumulant of the APS with κ for different system sizes at $\lambda = 3$. We see here the crossing points for three sets of $(L, 2L)$ (example of extrapolation to critical point shown in inset of Fig. 2·13) and also that B_c becomes negative for large sizes after the crossing point.

the constant c corresponds to the central charge of the CFT.

Using this formulation, we can extract the effective central charge of the apparent CFT. We have done this for a set of different λ (shown in Fig. 2·7) for different sizes and find the effective central charge to be close to unity for $\lambda \neq 0$. At $\lambda = 0$, the VBS phase shifts from being composed of bonds of unit length to one made out of bonds of length 3 (as unit-length bonds have null weight), and we find the extracted c to be closer to 3/2 in this case. The values 1 and 3/2 are both possible CFT central charges in the case of SU(2) symmetry, and $c = 1$ is associated with continuously varying exponents. Here we have not studied finite-size effects, due to difficulties in

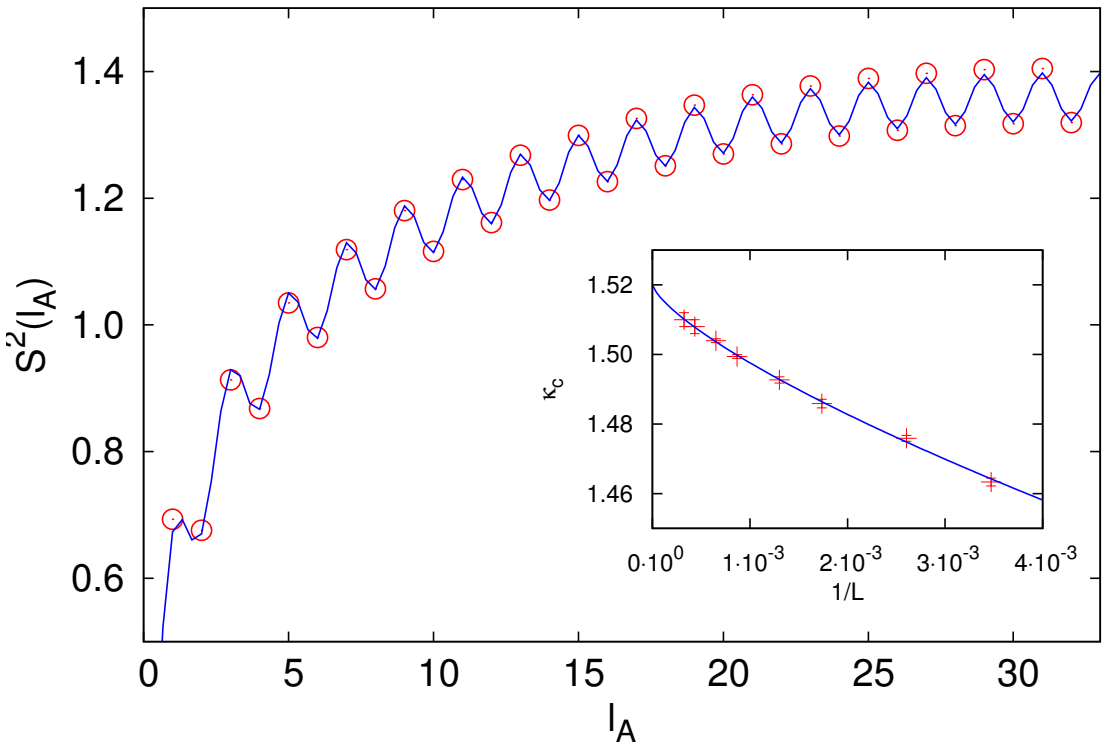

Figure 2·6: EE of the 1D critical APS at $\lambda = 1$ for a periodic chain of $L = 64$ sites. A fit to the form predicted by Eq. (2.12), along with finite size corrections (Xavier and Alcaraz, 2012) causing the visible even-odd oscillations, gave $c = 1.08(4)$. Error bars are of the order of the symbol size. The inset shows the extrapolation of the Binder cumulant crossings points (examples of which are seen in Fig. 2·12), which we have used to extract the critical κ for the infinite system. Here κ_{crit} is 1.519(5).

accurately computing the EE for larger system sizes, and it is not clear whether c will flow with increasing size to 1 (in general) and 3/2 (in the special case of $\lambda = 0$), or whether the value changes continuously as we vary λ. In any case, as we will see, the system should not have a CFT description and it is interesting that the "effective c" nevertheless is close to common CFT values.

Next we look at the critical exponent for the spin correlation using the technique of Binder crossings and flowing exponents at different λ. The spin dimension calculated

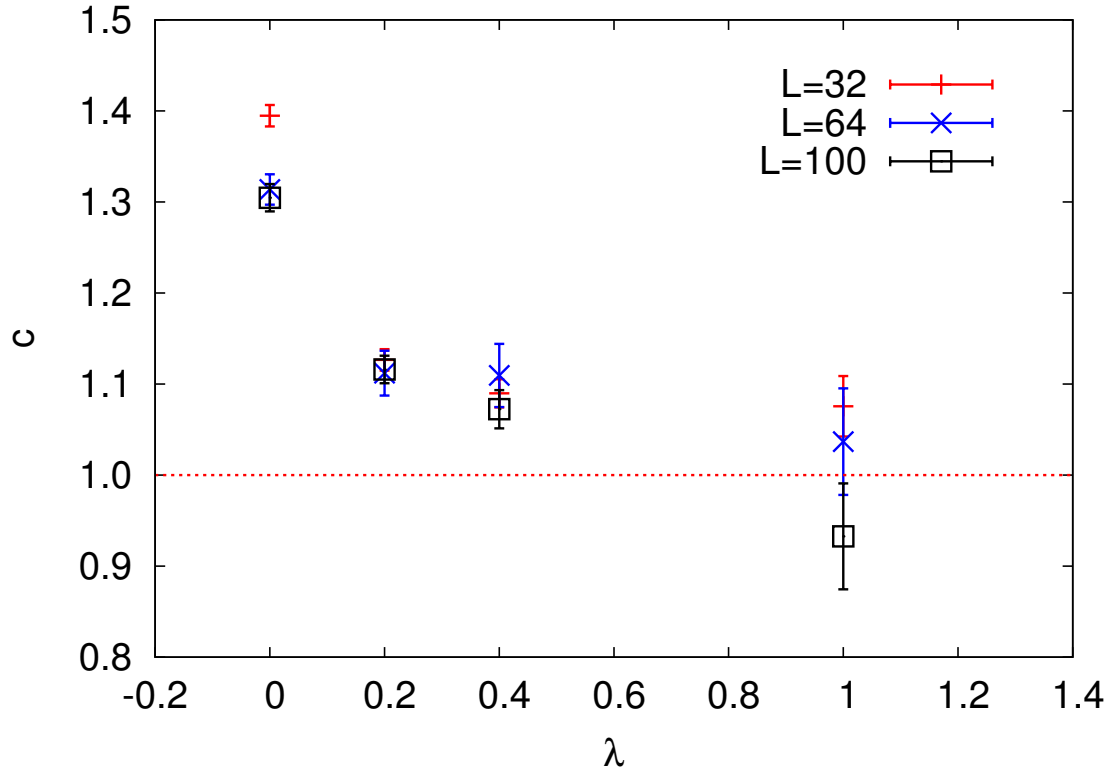

Figure 2·7: EE for the 1D critical APS versus the parameter λ, extracted as illustrated in Fig. 2·13.

from the two- and four-point functions in Fig. 2·14 disagree slightly when $\lambda \approx 1$, but considering the relatively large error bars we consider the agreement satisfactory nevertheless. The exponent values differ substantially from the expected CFT value 1/2 for the entire range of λ studied. This rules out a k=1 WZW description of the critical APS.

We can also study the scaled r-dependent correlation function as defined in Eq. (2.6), and we expect that it would not flow to a constant with respect to point separation with increasing size as there does not appear to be a CFT description for this system. In Fig. 2·9 we show results for $\lambda = 1$ using the scaling dimension $\Lambda_\sigma = 0.38$ from Fig. 2·8 and tuning slightly to 0.40 to get data collapse for a large range of $\frac{x}{L}$, and find that it does not follow the CFT functional form even for a large system of 12288 sites.

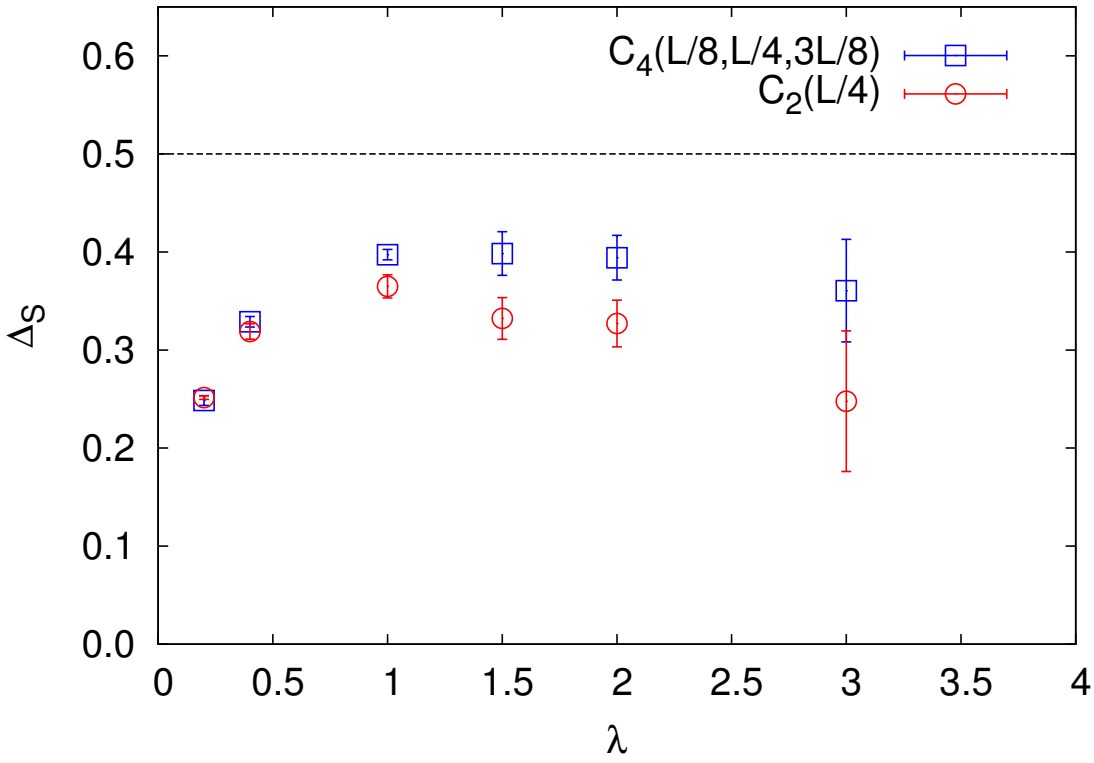

Figure 2·8: Dimension of the spin operator in the 1D critical APS graphed vs the short-bond parameter λ. The values were deduced using two- and four-point functions calculated on the critical curve.

To check the deviations more explicitly, we define the ratio of the scaled correlations at two different distances,

$$R(r_1, r_2) = \frac{C_{sc}(r_1)}{C_{sc}(r_2)}, \tag{2.13}$$

which should approach unity for all r_1, r_2 when $L \to \infty$ if the CFT description is valid. In the inset of Fig. 2·9 we plot $R(0.2, 0.5)$ as a function of $1/L$ at criticality and extrapolate it to infinite size using a second-order polynomial. We see that the result deviates substantially from unity, suggesting that this indeed is a good CFT test (here with a negative result). We were not able to look at the behavior of dimer correlators in the APS, as we have done with the J-Q chain, as the dimer order is quite weak at criticality and not substantial enough to perform a careful finite-size

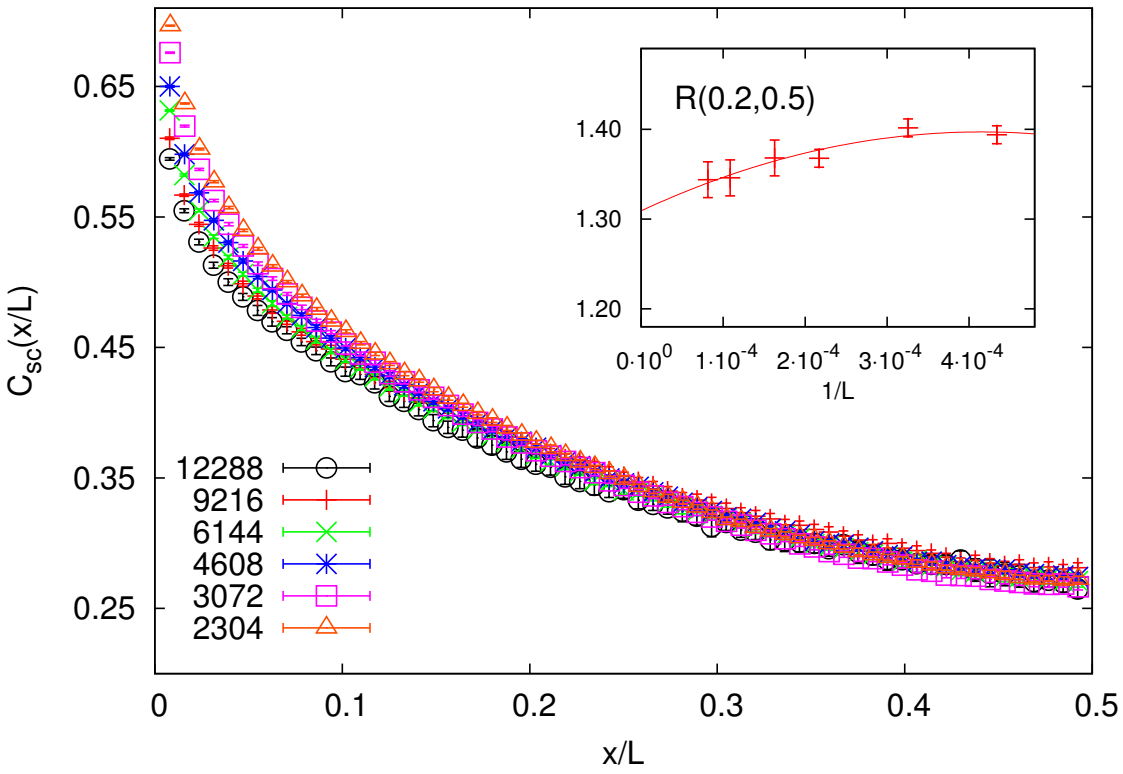

Figure 2·9: Scaled spin correlation functions, defined in Eq.(2.6), plotted against the separation as a fraction of the system size for the critical APS at $\lambda = 1$ (where $\kappa_{\text{crit}} = 1.519$). The inset shows the ratio $R(0.5, 0.2)$ Eq. (2.13), of the correlations at two distances.

scaling analysis with large system sizes.

We have found that the EE of the APS falsely points towards the existence of a conformal description at criticality. We have determined the inapplicability of a CFT description by extracting the dimension of the spin operator and by investigating the behavior of the two-point spin correlator. As the APS is capable of harboring a long-range ordered Néel state in 1D, it is apparent that the Hamiltonian must have long-range interactions on this side of the phase transition, and it is likely that the effects of these interactions carry on to the critical point as well, thus perhaps preventing a CFT description (as that requires sufficient locality of the interactions). Note that long-range interactions do not automatically preclude a CFT description and there are

indeed examples of this, e.g., SU(N) spin chains with exchange interactions decaying with distance r as $1/r^2$ (Haldane et al., 1992). As the rate of decay is decreased, one would at some point expect the CFT description to break down.

Examples of direct transitions between antiferromagnetic and VBS phases have already been seen in both frustrated and (Sandvik, 2010a) and unfrustrated (Laflorencie et al., 2005) spin chains with tunable power-law decaying long-range interactions, and it was found that the dynamic exponent $z < 1$. Thus, space and time do not scale in the same manner and we cannot have a $1+1$-dimensional CFT description of such a system (though scale invariance still holds). As the Hamiltonian of the APS is unknown, it is not possible to determine z, but given that there is a long-range ordered Néel state terminating at the critical curve it seems plausible that the Hamiltonian could have $z \neq 1$. It might indeed be worthwhile to find the parent Hamiltonian and to test this conjecture.

Our numerics have also shown that the critical APS looks like a CFT when examined only through the lenses of entanglement, following the predicted scaling with the size of the subsystem of the bipartition and even delivering values of c in the range of common CFT values (the effective c being close to 1 and 3/2). Thus, our study shows that care has to be taken when using the EE to establish the proper field-theory description, and it is important to also tests the constraints of CFTs in the details of correlation functions.

2.4 Emergent symmetry in the Heisenberg antiferromagnetic chain

The spin-1/2 Heisenberg chain, with the Hamiltonian

$$H = \sum_{i=1}^{N} \vec{\mathbb{S}}_i \cdot \vec{\mathbb{S}}_{i+1} \tag{2.14}$$

can be transformed into a system of interacting spinless fermions of two species using the transformation (Affleck, 1985; Affleck and Haldane, 1987):

$$\vec{\mathbb{S}}_n = \frac{1}{2}\psi^{\dagger}{}^i_n \vec{\boldsymbol{\sigma}}^j_i \psi_{nj}, \tag{2.15}$$

where ψ^i_n is a spin doublet and repeated indices imply summation over the range of values that the index can take (as we will use throughout this work). To take the continuum limit, we will reiterate the series of arguments presented in (Affleck, 1985; Affleck and Haldane, 1987) and use this process to define quantities that we will use later. Each fermion in the doublet can be rewritten as two new fermions,

$$\psi^j_n \simeq [i^n \psi^j_L(n \pm \frac{1}{2}) + (-i)^n \psi^j_R(n \pm \frac{1}{2})], \tag{2.16}$$

(plus and minus for even and odd n, respectively) which is an exact transformation up to an overall factor. This is motivated by the expectation that the free-fermion ground state would have all states with $|k| < \pi/2a$ occupied and then only Fourier modes with $k \simeq \pm\pi/2a$ would be important (Haldane, 1980). Thus, we understand the left (L) and right (R) fermion operators to be "locally" constant and to be slowly varying at the scale of lattice separation. These will ultimately form the operators of the continuum field theory. We can now write the spin operator on the lattice, using the current operators

$$\vec{J}_L = \psi^{\dagger}{}^i_L \vec{\boldsymbol{\sigma}}^j_i \psi_{Lj}, \tag{2.17a}$$

$$\vec{J}_R = \psi^{\dagger}{}^i_R \vec{\boldsymbol{\sigma}}^j_i \psi_{Rj}, \tag{2.17b}$$

and the fermion bilinear

$$\boldsymbol{G}^i_j = \psi^{\dagger}{}^i_L \psi_{Rj}, \tag{2.18}$$

by direct substitution in Eq. (2.15) as

$$\mathbb{S}_n^i = a(J_L^i + J_R^i) + (-1)^n a\mathrm{Tr}[(\boldsymbol{G} - \boldsymbol{G}^\dagger)\boldsymbol{\sigma}^i]. \tag{2.19}$$

Here we have used script letters for lattice operators and bold font for matrices and we will continue to maintain these conventions throughout this text. The operators $\vec{J}_L, \vec{J}_R, \boldsymbol{G}$ are defined at the same lattice position n as the spin operator but this is not explicitly indicated to keep the equations unencumbered. This form of the spin operator can be substituted into the Hamiltonian of Eq. (2.14), which upon coarse graining has the following continuum limit,

$$H = (a/2)\int dx[\vec{J}_L \cdot \vec{J}_L + \vec{J}_R \cdot \vec{J}_R + 2\vec{J}_L \cdot \vec{J}_R] + ..., \tag{2.20}$$

where a is the lattice spacing (Affleck, 1985).

Note also that at this stage we have only one SU(2) symmetry which comes along with the 3D rotation symmetry that the microscopic model has. This is manifest in each of $\vec{J}_{L/R}$ but they are not free to turn through different arbitrary angles due to the $\vec{J}_L \cdot \vec{J}_R$ term which keeps the relative angle between them fixed. Assuming that this Hamiltonian flows to the free fermion fixed point, which has the Hamiltonian

$$H_{fixed} = \int dx[\vec{J}_L \cdot \vec{J}_L + \vec{J}_R \cdot \vec{J}_R], \tag{2.21}$$

it can be shown that the term that couples left and right currents in Eq. (2.20) is irrelevant under RG flow (Affleck, 1985; Affleck and Haldane, 1987) for this particular fixed point. This is not true for all perturbations to the fixed point Hamiltonian and thus was checked explicitly (Affleck, 1985; Affleck and Haldane, 1987) for the $\vec{J}_L \cdot \vec{J}_R$ term. Thus we see that this line of reasoning leads us to believe that in the thermodynamic limit we should be left with the free fermion fixed point, which is also described by the $k = 1$ Wess-Zumino-Witten (WZW) conformal field theory (Belavin

et al., 1984).

To understand how the decoupling of the currents affects correlation functions of spin and dimer operators, we must first connect the primary operators of the CFT to these order parameters. Once we have done this, we can use the constraints that the extended symmetry places on the correlation functions of the primary operators to understand the correlations of the measurable orders.

The primary operators of the $k = 1$ WZW theory that we are going to be interested in are $[\boldsymbol{J_L}, \boldsymbol{J_R}, \boldsymbol{g}]$, which are the left and right currents with scaling dimension 1 and the primary field with scaling dimension 1/2. These are all SU(2) matrices, although the currents form matrices which belong to the Hermitian subset of SU(2), which are described by SO(3) vectors. This can be seen by observing that $\vec{J}_{L/R}$ in the fixed point Hamiltonian [Eq. (2.21)] are SO(3) vectors and thus the matrices to represent these must be written as

$$\boldsymbol{J_{L/R}} = J^a_{L/R}\boldsymbol{\sigma^a}, \tag{2.22}$$

where $J^a_{L/R}$ form the components of $\vec{J}_{L/R}$. This structure is also justified by the framework of the 2D CFT, which requires independent generators of translations for z and $\bar{z}$ (conjugate variables in the complex plane). In the Virasoro algebra of the 2D CFT (Di Francesco et al., 1997), these would usually be called $J(z)$ and $\bar{J}(\bar{z})$ and in the case of the left (right) fermion, $z = x + it$ ($\bar{z} = x - it$) would encode its space-time position.

The primary field $\boldsymbol{g}$ is made out of the continuum versions of the lattice operators which we shall denote as (S^a, D). The components S^a form the continuum spin operators and D represents the continuum dimer operator. These together form an SO(4) pseudovector which is embedded in $\boldsymbol{g}$ through

$$\boldsymbol{g} = S^a\ i\boldsymbol{\sigma^a} + D\boldsymbol{I}, \tag{2.23}$$

as any general SU(2) matrix can be expanded in this manner. The continuum versions of spins and dimers will be mapped back to the lattice variables in the next section. The primary field $\boldsymbol{g}$ is also closely related to the fermion bilinear $\boldsymbol{G}$ as $\boldsymbol{g}$ is influenced by transformations in both z and $\bar{z}$ (left and right rotations) and $\boldsymbol{G}$ is made out of left- and right-moving fermions and is also sensitive to transformations in both of them.

As mentioned earlier, the left and right currents can turn through different arbitrary angles at the fixed point and these SO(3) rotations can be written in terms of transformations on the SU(2) matrices as

$$\boldsymbol{J_L} = J_L^a \boldsymbol{\sigma^a} \rightarrow \boldsymbol{L J_L L^\dagger} = J_L^{'a} \boldsymbol{\sigma^a}, \tag{2.24a}$$

$$\boldsymbol{J_R} = J_R^a \boldsymbol{\sigma^a} \rightarrow \boldsymbol{R J_R R^\dagger} = J_R^{'a} \boldsymbol{\sigma^a}, \tag{2.24b}$$

where $\boldsymbol{L}$ and $\boldsymbol{R}$ are the SU(2) rotation matrices. It is important to note here that these rotations do not mix left and right currents and keep the 2D conformal structure intact. The field $\boldsymbol{g}$ depends on z and $\bar{z}$ by construction (Di Francesco et al., 1997) and thus is affected by both left and right rotations. These rotations are reflected in (S^a, D) through

$$\boldsymbol{g} = S^a \; i\boldsymbol{\sigma^a} + D\boldsymbol{I} \rightarrow \boldsymbol{L g R^\dagger} = S^{'a} \; i\boldsymbol{\sigma^a} + D^{'}\boldsymbol{I}, \tag{2.25}$$

which creates the new set $(S^{'a}, D^{'})$. The matrices $(\boldsymbol{g}, \boldsymbol{J_L}, \boldsymbol{J_R})$ live on the complex plane formed by space-time and so do their components. The correlation functions of these components (which are the continuum spin, dimer, and current operators) on the complex plane are of interest to us as they tell us what to expect for the correlation functions of the lattice operators, which we will investigate numerically later. We would also like to point out here that all the correlation functions that we consider in this text are connected correlation functions as they are the ones which

the CFT predicts. From this point on, we will not explicitly mention that we are only considering connected correlation functions. For the continuum operators, the connected correlation functions we consider are the same as the naive correlation functions as all the operators have a zero single body expectation (enforced by the CFT) value and this implies nothing needs to be subtracted from the naive correlation function to get the connected one.

To extract the correlation functions of (S^a, D), we examine

$$\langle \mathrm{Tr}[\boldsymbol{g}_{z_1}\boldsymbol{g}^\dagger_{z_2}]\rangle = \langle S^a S^a\rangle + \langle DD\rangle \tag{2.26}$$

and see that the right hand side is non-zero as the arbitrary transformations $\boldsymbol{L}$ and $\boldsymbol{R}$ leave the two point function of $\boldsymbol{g}$, as defined here, unchanged through Eq. (2.25) due to the cyclicity of the trace and as $\boldsymbol{R}^\dagger\boldsymbol{R} = \boldsymbol{L}^\dagger\boldsymbol{L} = \boldsymbol{I}$. Similarly, if we look at the transformation of the three-point function,

$$\begin{aligned}\langle \mathrm{Tr}[\boldsymbol{g}_{\boldsymbol{z_1}}\boldsymbol{g}^\dagger_{z_2}\boldsymbol{g}_{\boldsymbol{z_3}}]\rangle \rightarrow \\ \langle \mathrm{Tr}[\boldsymbol{L}\boldsymbol{g}_{z_1}\boldsymbol{R}^\dagger\boldsymbol{R}\boldsymbol{g}^\dagger{}_{z_2}\boldsymbol{L}^\dagger\boldsymbol{L}\boldsymbol{g}_{z_3}\boldsymbol{R}^\dagger]\rangle,\end{aligned} \tag{2.27}$$

we see that the only way to keep this invariant under arbitrary $\boldsymbol{L}$ and $\boldsymbol{R}$ would be to have this vanish. The vanishing of the three-point function then implies that all three-point functions of (S^a, D) (which could be either of $\langle S^a S^a D\rangle, \langle S^a D S^a\rangle, \langle D S^a S^a\rangle$, $\langle DDD\rangle$) would vanish. This can be seen by writing down all the possible three-point functions of $\boldsymbol{g}$ and $\boldsymbol{g}^\dagger$ and solving for the spin and dimer correlation functions.

When discussing the lattice spin and dimer correlation functions, we will also need the continuum versions of the correlation functions of the currents and operators. The expressions which are of interest to us and robust against arbitrary $\boldsymbol{L}$ and $\boldsymbol{R}$ transformations are

$$\langle \mathrm{Tr}[\boldsymbol{J_L}\boldsymbol{J_L}]\rangle \sim \langle J^a_L J^a_L\rangle, \tag{2.28}$$

$$\langle \mathrm{Tr}[\boldsymbol{J_L} \boldsymbol{g} \boldsymbol{g}^\dagger] \rangle \sim \langle J_L^a S^a D \rangle + \langle J_L^a D S^a \rangle, \tag{2.29}$$

and permutations of the second equation with $\boldsymbol{J_L}$ in different positions. These equations also apply for the right currents by just switching all $L \to R$. The non-vanishing nature of these correlation functions can be seen again using the cyclicity of the trace and transformation equations (2.24a), (2.24b) and (2.25).

We have seen above that some of the correlation functions of continuum operators vanish and for the ones that do not, we can predict their functional forms based on the CFT constraints. The primary operators of the $k = 1$ WZW model are $\boldsymbol{J_L}, \boldsymbol{J_R}$ and $\boldsymbol{g}$ with scaling dimensions $(h, \bar{h})$ given by (1,0),(0,1) and (1/4,1/4) respectively. Using these dimensions, we can infer that the correlation functions on the periodic chain must have the following forms,

$$\langle \mathrm{Tr}[\boldsymbol{g}(0)\boldsymbol{g}^\dagger(x)] \rangle \sim \frac{1}{L \sin(\pi \frac{x}{L})}, \tag{2.30a}$$

$$\langle \mathrm{Tr}[\boldsymbol{J_L}(0)\boldsymbol{J_L}(x)] \rangle \sim \frac{1}{\left[L \sin(\pi \frac{x}{L})\right]^2}, \tag{2.30b}$$

$$\langle \mathrm{Tr}[\boldsymbol{J_L}(0)\boldsymbol{g}(x)\boldsymbol{g}^\dagger(y)] \rangle \sim \frac{1}{\left[L \sin(\pi \frac{x}{L})\right]\left[L \sin(\pi \frac{y}{L})\right]}, \tag{2.30c}$$

and the same for $L \to R$. We can now use these expressions to understand the lattice correlation functions by writing the lattice operators in terms of their continuum versions. Inspired by the analysis leading up to Eq. (2.19), the spin and dimer lattice operators have been postulated (Affleck, 1985; Tsvelik, 2007) to be

$$\mathbb{S}_n^i \sim \alpha(J_L^i + J_R^i) + (-1)^n \beta S^i, \tag{2.31a}$$

$$\mathbb{D}_n = \vec{\mathbb{S}}_n \cdot \vec{\mathbb{S}}_{n+1} \sim D_0 + (-1)^n \gamma D, \tag{2.31b}$$

where α, β, γ are UV sensitive prefactors and D_0 is a constant shift of the lattice dimer operator which must be subtracted out when calculating connected correlation

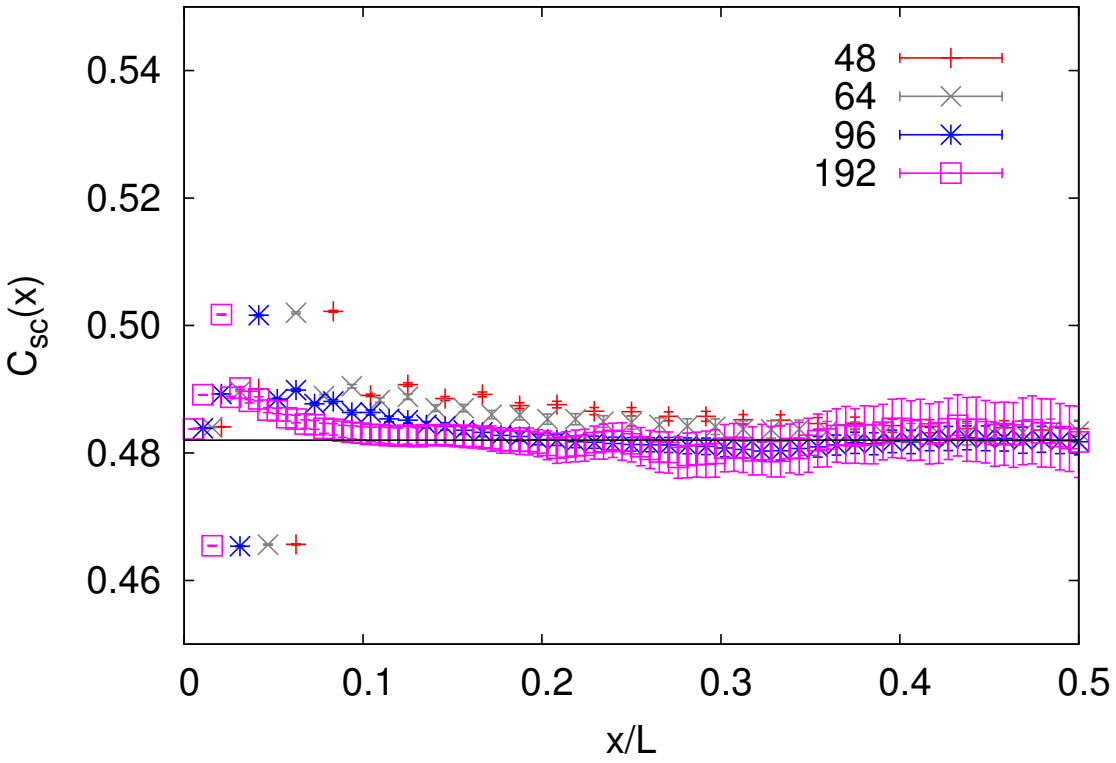

Figure 2·10: Scaled dimer two-point function for the critical JQ_2 periodic chain as defined in Eq. (2.38). The results flow to a constant with increasing size. The Horizontal axis only extends to $x/L = 0.5$ as two-point functions are symmetric about $y = L/2$.

functions.

Using this equivalence between the lattice and continuum operators, we can construct the lattice correlation functions that we are going to use;

$$\langle \mathbb{D}\mathbb{D} \rangle \sim (-1)^n \langle Tr[\boldsymbol{g}\boldsymbol{g}^\dagger] \rangle + ..., \tag{2.32a}$$

$$\langle \mathbb{D}\mathbb{D}\mathbb{D} \rangle \sim 0 + ..., \tag{2.32b}$$

$$\langle \vec{\mathbb{S}} \cdot \vec{\mathbb{S}} \rangle \sim (-1)^n \langle Tr[\boldsymbol{g}\boldsymbol{g}^\dagger] \rangle + \langle \vec{J}_L \cdot \vec{J}_L \rangle + \langle \vec{J}_R \cdot \vec{J}_R \rangle + ..., \tag{2.32c}$$

$$\langle \vec{\mathbb{S}} \cdot \vec{\mathbb{S}}\mathbb{D} \rangle \sim \langle Tr[\boldsymbol{J_L}\boldsymbol{g}\boldsymbol{g}^\dagger] \rangle + \langle Tr[\boldsymbol{g}\boldsymbol{J_L}\boldsymbol{g}^\dagger] \rangle + (L \to R) + ..., \tag{2.32d}$$

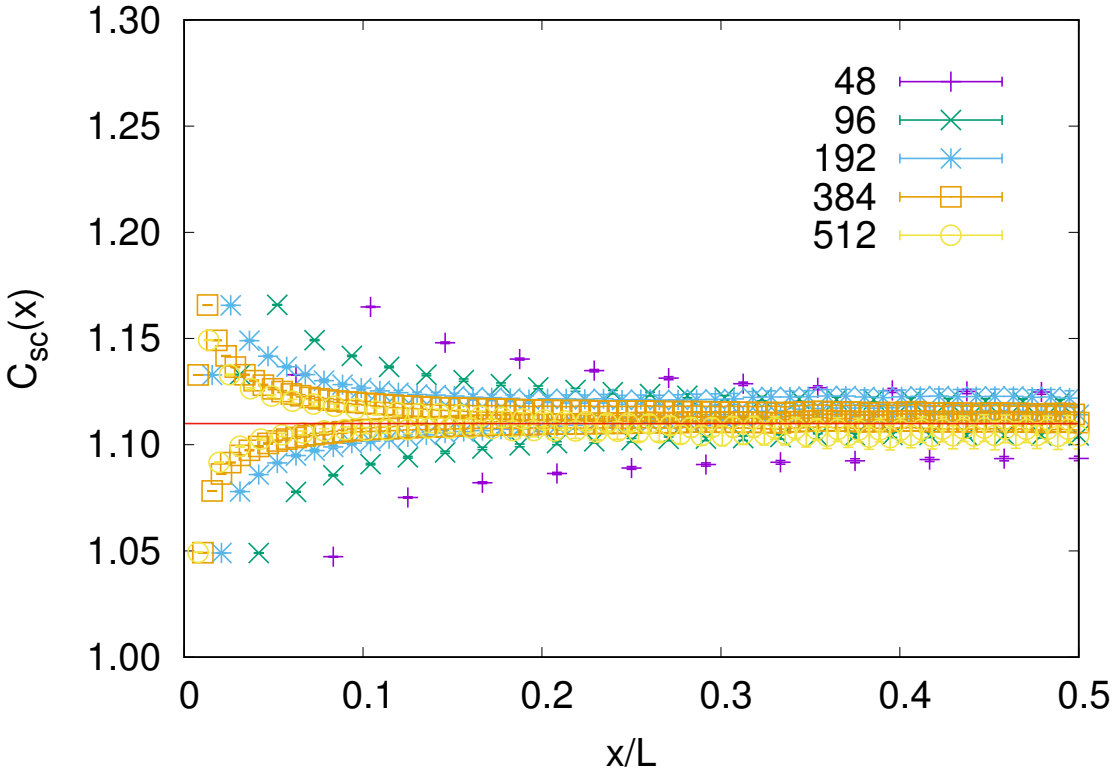

Figure 2·11: Spin two-point function for the critical JQ_2 chain scaled with the first term of Eq. (2.35) [as explicitly shown in Eq. (2.39)]. The approach to a constant for large sizes confirms the expected form.

where we have dropped the prefactors as they are UV-controlled parameters which are not important from the continuum perspective and to keep the equations from becoming unnecessarily dense. The additional terms ignored in these equations are lattice non-asymptotic corrections which occur due to finite distance and lattice size. Our simulations use lattices large enough to observe the decay toward zero of these contributions.

We can incorporate the results of Eqs. (2.30a), (2.30b) and (2.30c) to hypothesize that the full functional forms of the connected lattice correlation functions are

$$\langle \mathbb{D}_0 \mathbb{D}_x \mathbb{D}_y \rangle \sim 0 + ..., \tag{2.33}$$

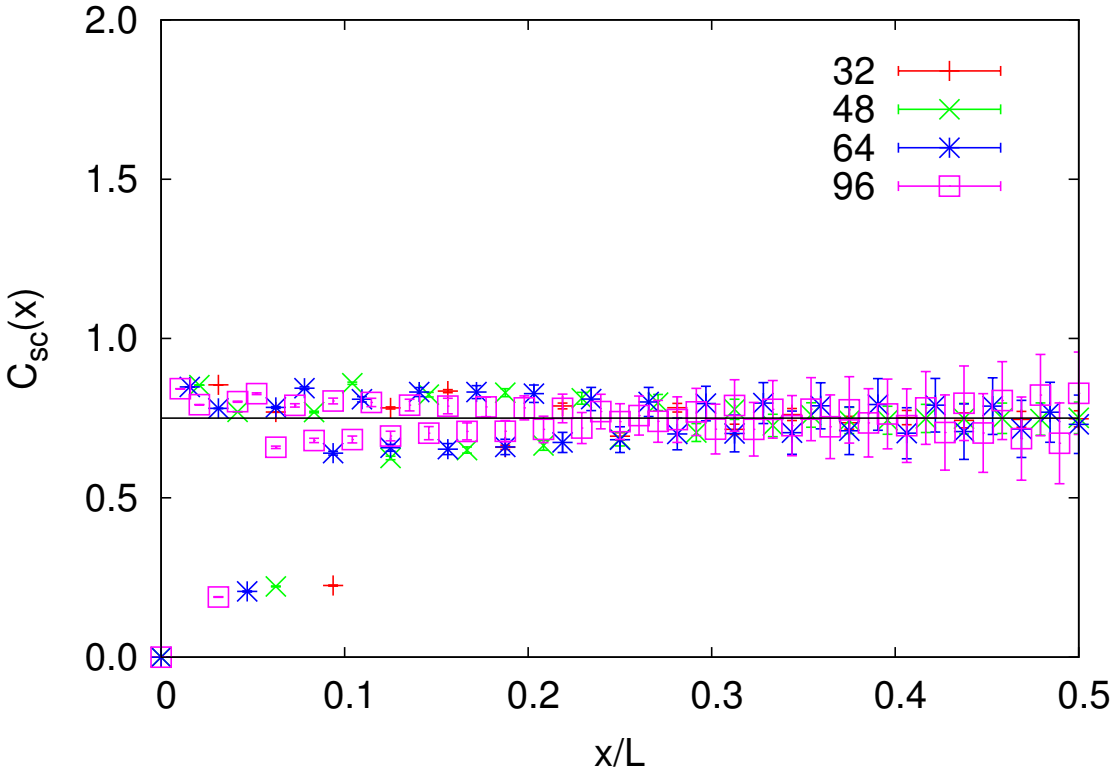

Figure 2·12: Spin two-point function for the critical JQ_2 chain with the first term of Eq. (2.35) subtracted out and scaled with the second term, as in Eq. (2.40). We see improving agreement with the expected form with increasing L.

$$\langle \mathbb{D}_0 \mathbb{D}_x \rangle \sim \frac{(-1)^x}{L \sin(\pi \frac{x}{L})} + ..., \tag{2.34}$$

$$\langle \vec{\mathbb{S}}_0 \cdot \vec{\mathbb{S}}_x \rangle \sim \frac{(-1)^x}{L \sin(\pi \frac{x}{L})} + \frac{1}{\left[L \sin(\pi \frac{x}{L})\right]^2} + ..., \tag{2.35}$$

$$\langle \mathbb{D}_0 \vec{\mathbb{S}}_x \cdot \vec{\mathbb{S}}_y \rangle \sim \frac{1}{L \sin\left[\frac{\pi}{L}(y-x)\right]} \left[\frac{(-1)^x}{L \sin(\pi \frac{y}{L})} - \frac{(-1)^y}{L \sin(\pi \frac{x}{L})} \right] + ... \tag{2.36}$$

The most striking effects of the extended symmetry are seen in Eqs. (2.33) and (2.36) where the vanishing of the three-point function of $\boldsymbol{g}$ ensures that there is no term with scaling dimension 3/2 (three times scaling dimension of $\boldsymbol{g}$) in either of these equations. In this case, if we were to use the three-point function's scaling form

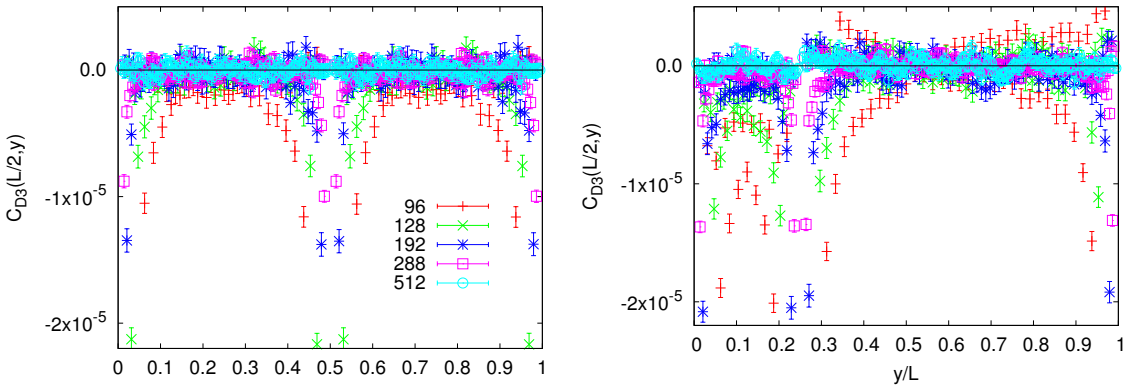

Figure 2·13: The Dimer three-point function for the critical JQ_2 chain vanishes for large enough system size, which agreement with Eq. (2.33), here shown for $x = L/4$ and $x = L/2$.

to infer the scaling dimensions of the operators (which imply the scaling dimensions should sum to 2), we would run into errors as we would be unable to make it consistent with the two point functions (which imply the scaling dimensions should sum to 3/2). To see proof of this numerically, we again calculate scaled correlation functions for these expressions, except for $\langle \mathbb{D}_0 \mathbb{D}_x \mathbb{D}_y \rangle$, which is expected to be zero. If the numerics agree, we should expect to see that the scaled functions are constants with respect to x and y, similar to the TFIM.

The continuum description of the Heisenberg model ground state has marginal operators which lead to log corrections to correlation functions. We shall use the JQ_2 chain which is the Heisenberg model with a four spin term that enforces dimer order when strong and tunes out the log corrections at the transition point (where the marginal operator vanishes) into the dimer phase;

$$H = -J\Sigma_i \mathbb{P}_{i,i+1} - Q\Sigma_i \mathbb{P}_{i,i+1}\mathbb{P}_{i+2,i+3} \tag{2.37}$$

where $\mathbb{P}_{i,j} = 1/4 - \vec{\mathbb{S}}_i \cdot \vec{\mathbb{S}}_j$. This model is an alternative to the more commonly used J_1-J_2 (first and second neighbor interacting) Heisenberg chain (Eggert, 1996), with the advantage that it is amenable to QMC studies without sign problems.

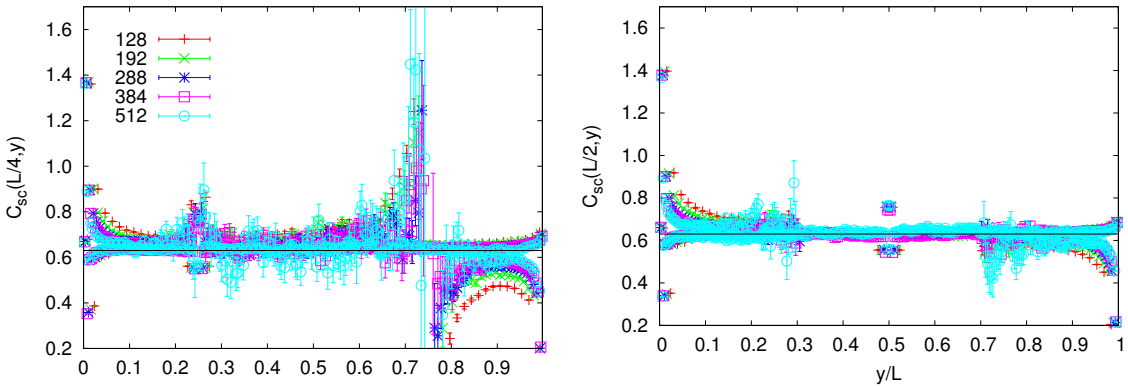

Figure 2·14: The scaled dimer-spin-spin three-point function, Eq. (2.41), for the critical JQ_2 flows to a constant, here demonstrated for $x = L/4$ and $x = L/2$. In the upper panel, the divergence at $y = 3L/4$ is due to the exact vanishing of the correlation function at this point. In the lower panel, data for even y values in the range $y/L \in (0.3, 0.7)$ have been excluded as $\langle \mathbb{D}_0 \vec{\mathbb{S}}_x \cdot \vec{\mathbb{S}}_y \rangle$ tends to a "0/0" form and, thus, the scaled correlation function is very noisy.

At a critical value of Q/J, $Q_c/J \approx 0.84831$ (Tang and Sandvik, 2011; Sanyal et al., 2011), we would expect to see the correlation functions behave according to the predicted forms. All our simulations of the ground state of the critical JQ_2 chain are done using a projector QMC method formulated in the valence-bond basis. The correlation functions are evaluated using loop estimators on the transition-graphs created by sampling the states in the valence-bond basis (Beach and Sandvik, 2006; Sandvik and Evertz, 2010). Fig. 2·10 illustrates the scaled correlator for $\langle \mathbb{D}_0 \mathbb{D}_x \rangle$, defined using Eq. (2.34) as

$$C_{sc}(x) = \langle \mathbb{D}_0 \mathbb{D}_x \rangle \times \frac{L \sin(\pi \frac{x}{L})}{(-1)^x}, \tag{2.38}$$

and we see that it approaches a constant for fairly small chain lengths. Fig. 2·11 shows the scaled version of the first term (scaling dimension of 1) of $\langle \vec{\mathbb{S}}_0 \cdot \vec{\mathbb{S}}_x \rangle$, again defined using Eq. (2.35) as

$$C_{sc}(x) = \langle \vec{\mathbb{S}}_0 \cdot \vec{\mathbb{S}}_x \rangle \times \left[\frac{L \sin(\pi \frac{x}{L})}{(-1)^x} \right], \tag{2.39}$$

which dominates the second term (scaling dimension of 2) and we see that this flows to a constant [1.11(1)] with increasing size. In Fig. 2·12, we subtract out the first term and present the scaled version of the second term in a scaled correlation function defined as

$$\begin{aligned} C_{sc}(x) = &\left[\langle \vec{\mathbb{S}}_0 \cdot \vec{\mathbb{S}}_x \rangle - 1.11 \times \frac{(-1)^x}{L \sin(\pi \frac{x}{L})} \right] \\ &\times \left[L \sin\left(\pi \frac{x}{L} \right) \right], \end{aligned} \tag{2.40}$$

for which we cannot go to large sizes due to insufficient data quality. We still can observe that it matches our expectations, flowing to a constant with increasing system size.

In Fig. 2·13, we show the agreement of the three-point dimer correlation function [denoted by $C_{D3}(x, y)$ in both figures] with Eq. (2.33) for two different values of x and the whole range of y values. Only in the case of the three-point dimer function, we present the raw correlation function without scaling as it is expected to be zero and there is no sense in which we can scale it. We show the same for Eq. (2.36) through Figs. 2·14 by again defining a scaled correlator as

$$C_{sc}(x, y) = \langle \mathbb{D}_0 \vec{\mathbb{S}}_x \cdot \vec{\mathbb{S}}_y \rangle \frac{L \sin\left[\frac{\pi}{L}(y - x) \right]}{\frac{(-1)^x}{L \sin(\pi \frac{y}{L})} - \frac{(-1)^y}{L \sin(\pi \frac{x}{L})}} \tag{2.41}$$

and observing that it approaches a constant for large sizes. With this numerical evidence, we conclude that the signatures of the extended symmetry that we expect to see are indeed present in the spin-1/2 Heisenberg chain. Finite-size (distance) corrections can be seen clearly in our numerical data and these should be described by irrelevant operators.

We have shown numerical evidence of the effects of the emergent SO(4) $\equiv$ [SU(2)$\times$ SU(2)]/Z_2 symmetry in the Heisenberg chain on the correlation functions of lattice operators. This establishes the IR emergent symmetry which was theoretically expected from a variety of arguments. The three-point function was discussed here as a useful tool to understand the structure of the underlying field theory and has been shown to yield useful information through not only its scaling dimension, but also its functional form. The clearest example of this is $\langle \mathbb{D}_0 \vec{\mathbb{S}}_x \cdot \vec{\mathbb{S}}_y \rangle$ whose observed scaling dimension is not directly related to the leading scaling dimensions of the operators it is made out of, due to cancellations of contributions from the field and current operators. Here, we have also developed tests of CFT through correlation functions and these can be used to test suspected extended symmetry in higher dimensional systems (Nahum et al., 2015; Wang et al., 2017) and more broadly to test for CFT signatures in general.

In higher dimensions, an open question is what system geometry is best suited for investigating the conformal symmetry explicitly in equal-time correlation functions. In 1D, for the ring geometry (infinite imaginary time, i.e., the ground state) the conformal distance naturally emerges, but it does not have a direct generalization to 2D or 3D. The functional form of the correlation functions when expressed using the conformal distance in 1D provides perhaps the most striking evidence of conformal invariance in finite systems, and such a concept in higher dimensions would be very useful for lattice calculations. QMC calculations of correlation functions can be readily extended to higher dimensions to check the existence of CFT descriptions if such concepts were to be developed. For 1D systems, density matrix renormalization group (DMRG) can be used to check the predictions of the CFT as well, including direct detection of the conformal tower of excitations (Chepiga and Mila, 2017). With DMRG calculations using the common open boundary conditions (as the computa-

tional cost of periodic boundaries is significantly higher), CFT results for correlation functions will only be valid away from the boundaries, and the correlation functions will then just depend on the lattice separation between sites instead of the conformal distance (achieved by the mapping of the infinite cylinder to the infinite plane). This would be relevant when simulating the critical J_1-J_2 chain which is not amenable to QMC due to the sign problem but has the same CFT description as the J-Q chain considered here, and is another model which recreates the $k = 1$ WZW model in the continuum limit.

2.5 Measuring Operator Expectation Values in QMC

Operator expectation values are calculated based on overlap diagrams of $\langle\psi_G|$ and $|\psi_G\rangle$. For both variational and projector QMC, the ground state $|\psi_g\rangle$ is generated in the singlet basis using different techniques, and once this is achieved, overlap diagrams are represented as shown in Fig. 2·15. As $|\psi_g\rangle = \sum_i c_i |V_i\rangle$, where $|V_i\rangle$ denotes a singlet cover, a particular step in the Monte Carlo chooses a singlet cover for each of the left and right projections, and the overlap is created by overlaying these configurations, resulting in a loop diagram. As the operator expectation values are usually calculated in the z-basis, which is an orthogonal basis, we need to understand the z-basis configurations which this overlap pattern hosts. A particular singlet state is a product state over singlets between exclusive pairs of sites, which are each a superposition of two anti-aligned z-states. This means that a singlet state is a superposition of 2^{N_s} z-states. When considering different left and right singlet states, the common z-states between these states lists the legitimate z-basis configurations. This listing is provided by the loop diagram, where the singlet constraints force all sites in a loop to be exactly aligned or anti-aligned depending on the sublattice assignment. The number of z-basis configurations is the 2^{N_l}, where N_l is the number of loops and is

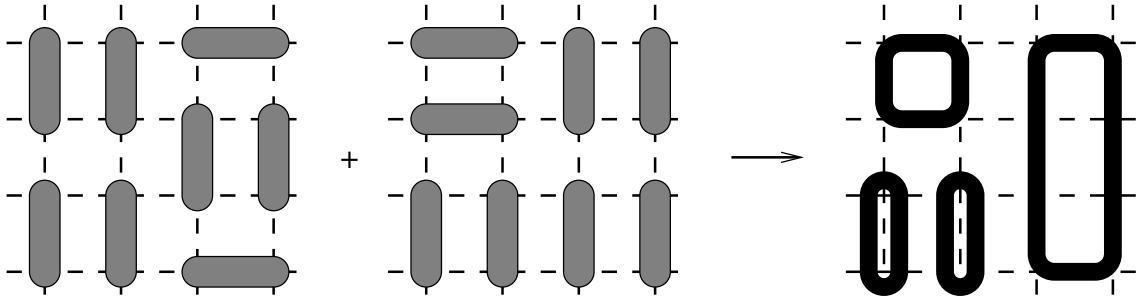

Figure 2·15: Overlap of two singlet states (left and right projection) creates a loop diagram.

necessarily $\leq N_s$. This automatically implies that, if we want to know the correlation between the spin states at two sites, we just need to keep track of how many times in the Monte Carlo simulation they reside in the same loop. If they are in the same loop, they are perfectly correlated, i.e. $\langle S_i^z S_j^z \rangle = 1/4$, else perfectly uncorrelated, i.e. $\langle S_i^z S_j^z \rangle = 0$. The total spin correlation is a sum over this for all loop diagrams generated during the Monte Carlo.

Configuration	Contribution
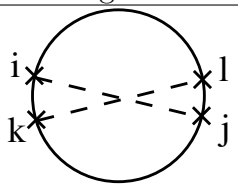	1/2
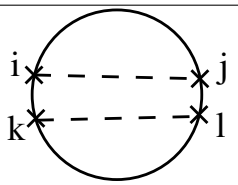	1
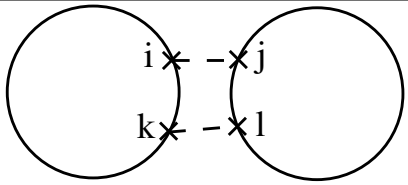	1/4

Table 2.1: Different loop configurations and their contributions

One must be more careful when considering operators that are off-diagonal in

the z-basis, e.g. an operator such as $\vec{S}_i \cdot \vec{S}_j$, which changes the loop diagram as it explicitly creates a singlet between sites i and j with a coefficient of $1/2$. The resulting loop diagram depends on the topology of the connectivity between i and j and the diagrams which contribute to the expectation value of this operator are listed in Table. 2.1 The new loop diagram may have a different number of loops, meaning that it corresponds to a different number of z-basis states and this must be factored in as well when calculating the contribution of a particular diagram. The first case in Table. 2.1 shows the new singlets generated by $\vec{S}_i \cdot \vec{S}_j$ as dotted lines, and we can see that the new connections create a figure of 8 without breaking the loop. This means that the number of loops is the same, and as the projection generates a factor of $1/2$, the contribution to the correlation is $1/2\times1$. In the second case, the dotted lines break the loop into 2, which means that the number of loops has increased by a factor of 2^1, and this factor applies to the number of z-basis configurations as well. This implies that the contribution in this case is $1/2\times2$. In the third case, i and j are initially in different loops, but the singlet projector links them into one, resulting in a factor of $1/2$ for the number of z-basis states. This leads to an overall contribution of $1/2\times1/2$. This process becomes especially tedious when considering operators which act on more than two sites. For instance, in the previous section, data is presented for the expectation value of the three point dimer operator $D_0D_xD_y$, which is a six point operator as $D_x = \vec{S}_i \cdot \vec{S}_{i+1}$. In this case, the six point operator must first be rewritten in term of the singlet projectors, and the corresponding diagrams analyzed to understand the contributing factors. For the three point dimer correlator, this can be simplified by using the rotational symmetry and writing it as $D_0D_xD_y = D_0D_x\vec{S}_y \cdot \vec{S}_{y+1} = 3D_0D_xS^z_yS^z_{y+1}$. All the diagrams which contribute to this simplified form of the six site correlation function are shown in Fig. 2·16, and the contributing factors can be worked out using the arguments

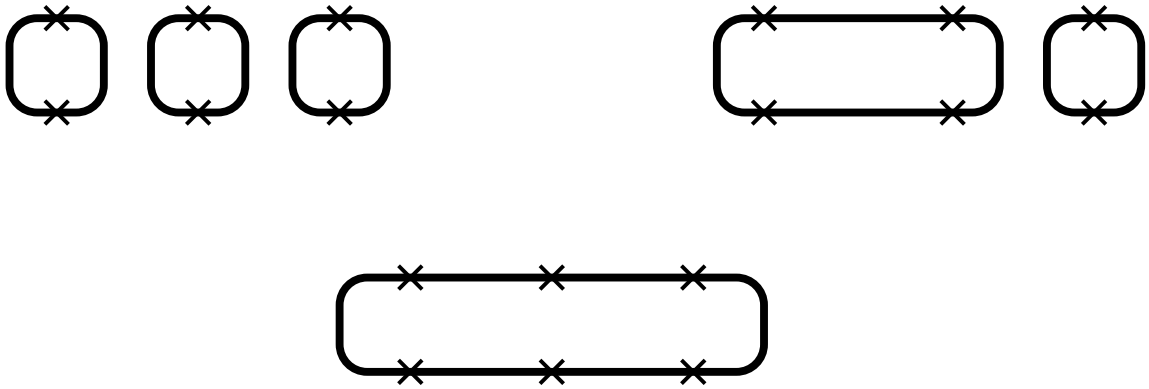

Figure 2·16: Loop diagrams for six site correlation function with sites represented by crosses, different permutations of site numbers lead to different contributions

presented for the case of two sites.

Chapter 3

Emergent Symmetry in 2D and Unconventional Scaling Behavior

3.1 Continuous symmetries and effects of anisotropy

Many condensed matter systems host degrees of freedom which have continuous symmetry. Famous examples of this are the U(1) symmetries of the BCS superconductivity order parameter and the Berezinskii-Kosterlitz-Thouless transition, and the SU(2) symmetries of Heisenberg spin systems in magnetic materials. In most realistic systems, these symmetries are not exactly realized due to imperfections such as lattice anisotropies and preferential couplings. In such cases, it is important to understand the effect of the anisotropy on the continuous symmetry. In some cases, the symmetry is preserved as the anisotropy proves to be irrelevant and leaves universal features such as the behavior at phase transitions unchanged. In this chapter, we will study the particular case of U(1) symmetry in a 2D quantum clock model, which shares features with the 3D classical clock model. The clock model is generated by adding anisotropy to Hamiltonian for a planar phase, which can take values between $[0, 2\pi\}$. A simple and common form of interaction used for such a system on a lattice is $\cos(\theta_i - \theta_j)$, where i and j are neighboring sites on the lattice. The field theory description of the phase transition in such a system can be written in terms of a phase ϕ, with a free energy term having a leading piece ϕ^2. The anisotropy can be represented by $\cos(q\phi)$, where q is an integer and is the number of favored directions.

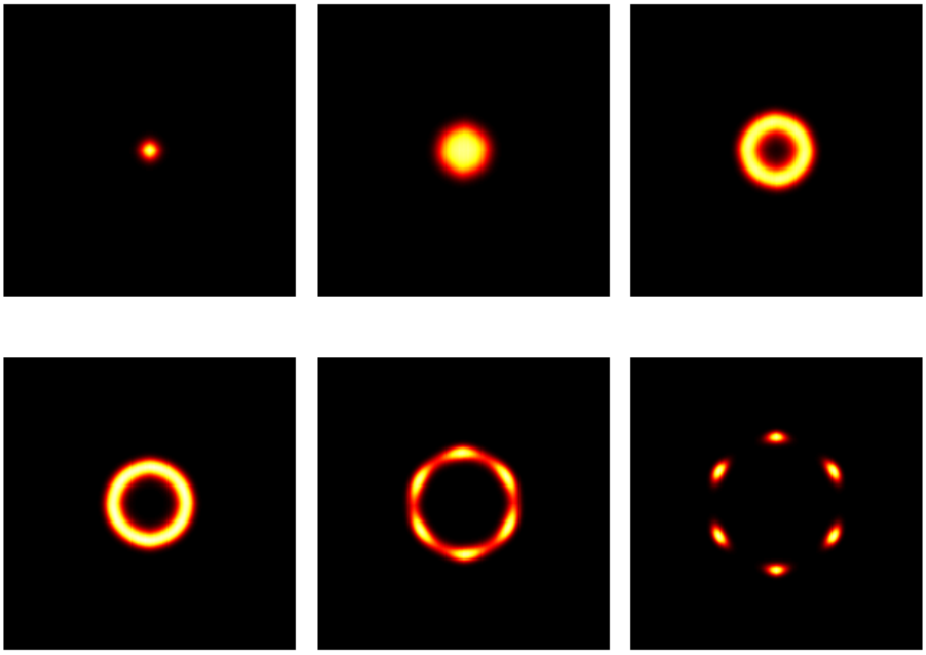

Figure 3·1: Histograms for the magnetization as a function of tuning parameter s. The critical value is $s_c = 0.2402(1)$. These simulations were carried out on a 48×48 square lattice.

Under renormalization, it has been found that for some values of q, the anisotropy flows to zero, implying that the long distance behavior is unchanged.

In the context of anisotropy, we must also discuss dangerously irrelevant operators as these play a crucial role at the phase transition. Before this, we briefly review general relevant and irrelevant operators. Renormalization group (RG) flows are controlled by relevant operators, whose coefficients must be explicitly tunes to zero to reach a critical point. For irrelevant operators, their coefficient flows to zero under the RG flow and thus they do not need to be explicitly tuned. If multiple relevant operators are present and a flow to a critical point is desired, the coefficients of all the relevant operators must be tuned as even a single untuned relevant operator leads to a flow away from the critical point. Depending on the coefficients, the flow forms a curve in coefficient space and this curve has a minimum distance to the critical

point we desire. Following this curve either leads to a runaway flow to infinities or, in rare cases, to a new fixed point. The only way to reduce the distance of this curve to the fixed point is by tuning the coefficient of the responsible relevant operator. Now we turn to the intriguing case of the dangerously irrelevant operator. This is a misnomer as the operator is actually relevant on one side of the transition. This is a consequence of the same tuning parameter controlling the coefficients of two different relevant operators. One of the operators is tuned intentionally, making the other a dangerously irrelevant operator. For the quantum clock model, the anisotropy acts as a such an operator. At the critical point, the global order parameter does not show the effect of anisotropy, and retains the U(1) symmetry. This can be seen in Fig. 3·1, where the histogram for the global magnetization vector $\mathbf{M}$ is plotted for different values of the tuning parameter s. We can see that when the magnetization begins to reach a non-zero value, in other words when the transition is complete, the circular symmetry starts to be affected by the anisotropy. The details of the model and other results are provided in the following sections.

3.2 Quantum Clock Model

Here we would like to study a q-state quantum clock model on a square lattice with periodic boundary conditions, defined using the Hamiltonian

$$H = -s \sum_{\langle i,j \rangle} \cos(\theta_i - \theta_j) - \frac{1-s}{q} \sum_i T_i^x, \tag{3.1}$$

where $\theta_i = \frac{2\pi}{q} k$ with k chosen from the set $\{0, ..., q-1\}$ and can be thought of as the angle of the 2D magnetization vector given by $\vec{M}_i = (\cos\theta_i, \sin\theta_i)$. The intersite interaction and the planar magnetization vector are chosen to be identical to the XY model, the only difference being the θ is now a discrete variable instead of being a continuous phase between 0 and 2π. T_i^x is the equivalent of a transverse

field in the quantum Ising model and can be represented as a $q \times q$ matrix with matrix elements such that $\langle\theta_i|T_i^x|\theta_i'\rangle = 1$ if $\theta_i \neq \theta_i'$ and zero otherwise. We make this particular choice for the quantum fluctuations as it allows us to efficiently simulate the system using quantum Monte Carlo. Using the quantum to classical mapping (Suzuki, 1976), this 2D quantum clock model maps to a 3D anisotropic classical model in the limit of infinite number of layers in the imaginary time dimension. To make all the interactions in the classical version of the form $\cos(\theta_i - \theta_j)$, we would have to use a transverse field term whose matrix elements are similar to those of the transfer matrix, i.e. $\langle\theta_i|T_i^x|\theta_i + 1\rangle > \langle\theta_i|T_i^x|\theta_i + 2\rangle > ....$ Even though the interactions along all directions would be similar using this sort of transverse field, the system may show different thermodynamic behavior than the 3D isotropic classical version due to the requirement of infinite number of slices in imaginary time. This would not be expected for our system as the order parameter is made out of the clock degrees of freedom and does not couple to the lattice directly. An easy choice of a transverse field operator which approximates the feature mentioned above would be $\langle\theta_i|T_i^x|\theta_i'\rangle \neq 0$ only if $|\theta_i - \theta_j| = 1$. Although this choice is more clock like than our definition of the transverse field operator which connects all states, we continue to use our definition as it recreates the physics of the 3D classical clock model even though the transverse field generates interactions in the extended imaginary time which are significantly different from the 3D clock model. For $s = 1$, the ground state is completely ordered with a Z_q symmetry and for $s = 0$ it is a paramagnetic state with each "spin" in a uniform superposition and no correlations between spins. The transverse field term has a $\frac{1}{q}$ suppression due to the O(q) number of non-zero matrix elements. All the off-diagonal terms drive the system out of a ferromagnetic state and it was found that without this suppressing factor, the critical point for large q approached $s = 1$ as very strong ferromagnetic interactions would be required to stabilize the ordered phase.

We can develop an approximate understanding of the $q = 3$ case using the quantum to classical mapping. This mapping extends the effect of a quantum fluctuation to a classical bond between copies of the system in imaginary time. For $q = 3$, we observe that T_i^x has the same matrix elements as the Potts interaction $\delta_{\theta_i,\theta_i'}$ and so does $\cos(\theta_i - \theta_j)$, which implies that it maps exactly to an anisotropic Potts model in 3D. This system would behave similar to the isotropic Potts model if the anisotropy is irrelevant at the critical point. We find evidence for a first order transition in agreement with the 3D isotropic Potts model (Janke and Villanova, 1997) using the Binder Cumulant for the $q = 3$ quantum clock model (Fig. 3·2). We define the Binder Cumulant using the total magnetization ($\vec{M} = \sum_i \vec{M}_i, M = |\vec{M}|$) as

$$U_m = \left(2 - \frac{\langle M^4 \rangle}{\langle M^2 \rangle^2}\right) \tag{3.2}$$

and use it to identify the critical point (s_c). For a first order transition, it is known (Binder, 1987) that the Binder Cumulant shows a negative peak which diverges as L^d, where L is the system size and d the dimension of the lattice. Fig. 3·2 illustrates U_m versus s for a few system sizes. The inset shows the scaling of the negative peak and we find good agreement with L^2. For $q > 3$, the mapping to the anisotropic Potts model only holds in imaginary time and we cannot gain intuition from the 3D classical Potts model. For $q = 5, 6$, we see that the system shows a continuous phase transition (Figs. 3·4, 3·5), reflected in the monotonic behavior of U_m, whereas for $q = 4$, we see that U_m begins to develop a negative peak only for large system sizes (Fig. 3·3). This implies the presence of a weak first order transition emerging for systems larger than 16×16 approximately.

The 2D quantum clock model for $q > 3$ can map to an anisotropic classical clock model in 3D in the strong anisotropy limit using a more complicated form of the transverse field as discussed above. Using this form for the quantum fluctuations

we can approximate the 3D classical clock and may expect to find that the quantum phase transition and the classical one driven by temperature have the same universality class. In the following section, we find that even the simpler form of the quantum term used in this work generates a quantum phase transition similar to the classical clock model which has an emergent U(1) symmetry for $q \geq 5$ (Lou et al., 2007). This suggests that the exact kinetic form of the transverse field term does not play a major role and perhaps the anisotropies generated are not relevant and leave the thermodynamic behavior unchanged. All of our data is generated using Stochastic Series Expansion Quantum Monte Carlo (SSEQMC), which uses Monte Carlo sampling to estimate the path integral at a particular temperature (Sandvik, 1999). Local and cluster updates were used on the spacetime configurations to maximize ergodicity and get accurate estimates. We choose a temperature which is low enough for the system to be in its ground state. All of the results presented in the next section are for $q = 5, 6$, although we believe that the arguments presented hold for general $q > 4$.

The quantum clock model shows an emergent U(1), or circular symmetry of the magnetization vector, at the quantum phase transition. The critical point separates the paramagnetic phase from the ferromagnetic phase, where all the spins point along a particular direction chosen out of q choices. This implies that the magnetization has a q-fold, or Z_q, symmetry and unit magnitude. Slightly above the critical point, the magnetization develops finite magnitude but retains a circular symmetry in its direction. This phenomenon has already been explored in the classical clock model in 3D (Lou et al., 2007) by investigating histograms of the magnetization vector. We quantitatively analyze the emergent symmetry using the Binder Cumulant of the magnetization defined previously and a U(1) order parameter defined as

$$\phi_q = \langle \cos(q\theta) \rangle \,, \tag{3.3}$$

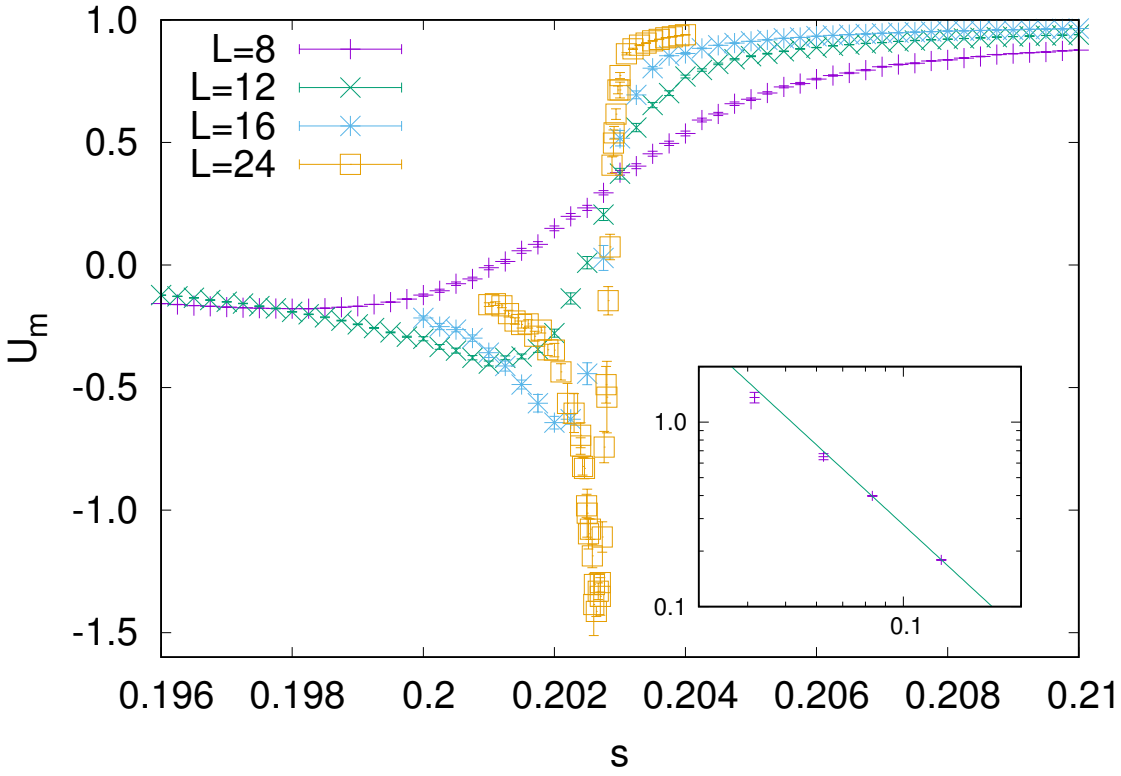

Figure 3·2: Binder Cumulant U_m for $q = 3$. The negative peak shows a potential first order transition. The inset shows the scaling of the negative peak value with $1/L$ fit to the form $f(L) = a/L^b$ with $b = 1.95(4)$.

where θ is the orientation of the thermodynamic magnetization $\vec{M}$. In the ferromagnetic phase θ can only take the values of $\frac{2\pi i}{q}$ with i being an integer in the set $\{0, ..., q-1\}$ and under this distribution of θ, ϕ_q evaluates to unity. If $\vec{M}$ is circularly symmetric, θ is chosen from a uniform distribution and ϕ_q vanishes. Note that this quantity is not sensitive to the magnitude of the magnetization, only its orientation. The magnitude can be probed using U_m which vanishes in the paramagnetic phase and is unity when the magnetization develops a finite value with small fluctuations around this value. Using ϕ_q and U_m, we can investigate four different regions which we find in our phase diagram. Two of these regions correspond to the paramagnetic phase ($U_m = 0$, $\phi_q = 0$) and the ferromagnetic phase ($U_m = 1$, $\phi_q = 1$) and are

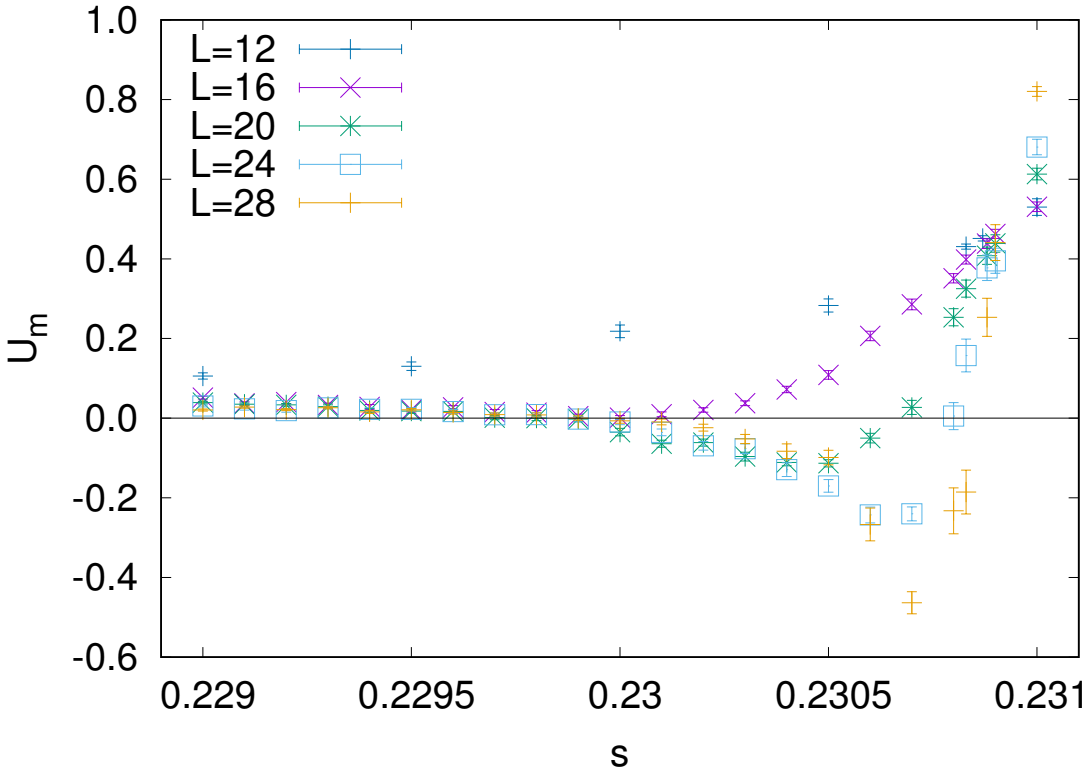

Figure 3·3: Binder Cumulant U_m for $q = 4$ shows a weak first order transition. The negative peak appears at sizes larger than 16x16.

stable fixed points when viewed from a renormalization group (RG) perspective. The other two regions are found in a vanishingly small vicinity of the critical point and correspond to the unstable critical point $U_m = c$, $\phi_q = 0$ where the magnetization develops power law correlations and the unstable U(1) symmetric point $U_m = 1$, $\phi_q = 0$. The constant c is characterized by the nature of critical fluctuations and is a universal number which we will discuss in detail later in this section. The U(1) symmetric point has a finite magnetization magnitude as $U_m = 1$. We identify these points on a RG flow diagram (Fig. 3·6) of ϕ_q versus U_m generated using SSEQMC for $q = 6$. Each trajectory in this diagram is at a particular value of s and the system size increases along the trajectory with the smallest system size being 3×3. The critical point is found to be at $s_c = 0.2402(1)$ using finite size scaling and we see that all

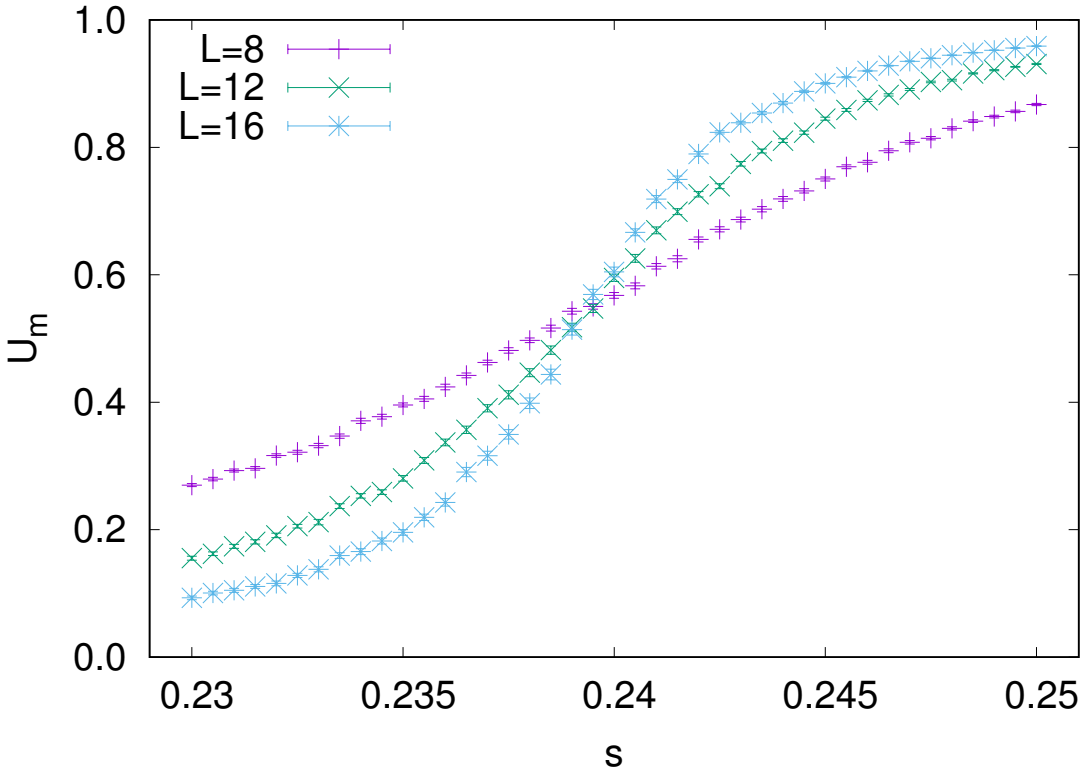

Figure 3·4: Binder Cumulant U_m for $q = 5$. The monotonic behavior of U_m is evidence of a continuous transition.

trajectories with $s < s_c$ flow to the paramagnetic fixed point and those with $s > s_c$ flow to the ferromagnetic one. Note that the trajectories for s slightly greater than s_c flow towards the critical point first and then to the U(1) symmetric point and finally to the ferromagnetic fixed point for large enough system sizes. For smaller $\epsilon = s - s_c$, we need to go to larger sizes to see the deviation from U(1) symmetry. This can be interpreted as another length scale becoming important in this system, which is the length scale at which the U(1) symmetry breaks. This length scale also diverges as we approach the critical point as seen in the RG flow diagram. This phenomenon is explained by a dangerously irrelevant operator (José et al., 1977; Oshikawa, 2000) which breaks the U(1) symmetry, i.e, it is irrelevant at the critical point but leads to a flow away from the U(1) symmetric line $\phi_q = 0$ for any $\phi_q > 0$. If we consider the

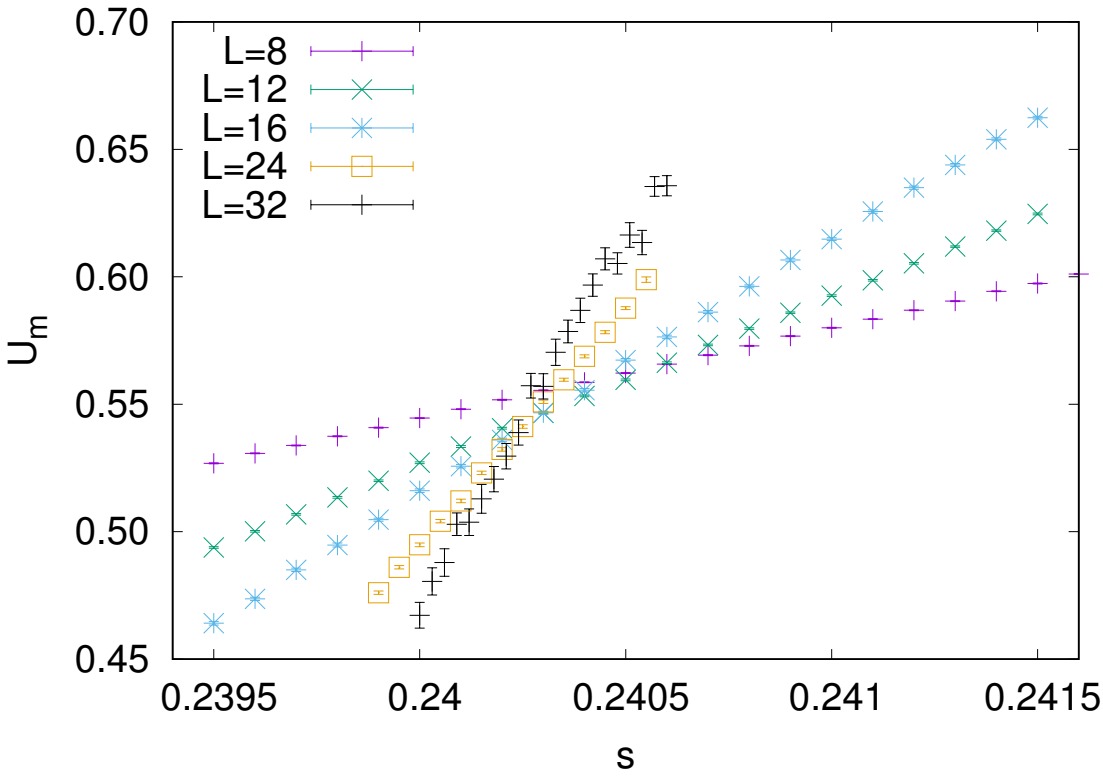

Figure 3·5: Binder Cumulant U_m for $q = 6$. The monotonic behavior of U_m is evidence of a continuous transition similar to the $q = 5$ case and the crossing points for different sizes can be seen here.

2D XY model, where the θ_i themselves are U(1) symmetric, we have $\phi_q = 0$ for the entire phase diagram due to the microscopic symmetry and the dangerously irrelevant operator does not play a role. Using this flow diagram we can understand the critical behavior around both unstable points. This has been done for the 3D XY model (Shao et al., 2019) where different scaling exponents were found in the vicinity of the unstable points corresponding to the XY and Z_q transitions along with the length scale at which the crossover between these two behaviors was observed.

The RG flow diagram shows us that the critical point hosts a U(1) symmetric state and the transition can be seen as that of a paramagnet to an ordered state with U(1) symmetry. A similar transition is shown by the 3D XY model, where the microscopic

phases are U(1) symmetric and the Hamiltonian is the same as a 3D classical clock model. This leads us to expect that the universality class of the 2D quantum clock model would be the same as the 3D XY model due to the nature of the critical point. We can verify this by checking for consistency between the critical exponents of both models. These exponents are calculated using the method of flowing Binder Cumulant crossing points (Luck, 1985) to study the scaling behavior. The critical exponent $1/\nu$ for the 3D XY transition is 1.489(1) and we use this value along with the leading finite size correction exponent $\omega = 0.8$ (Campostrini et al., 2001) to fit the flowing exponent for $q = 5, 6$ to the form $1.489 + aL^{-0.8}$ and find acceptable fits (Fig. 3·7). We can repeat the same process for the spin correlation exponent η and we find that we are unable to fit our data to the expected value of 0.0380(4) (Campostrini et al., 2001) and instead find $\eta = 0.07(1)$ for both $q = 5$ and 6 (Fig. 3·8) using a general fitting function of the form $\eta(L) = \eta(\infty) + aL^{-b}$. This may be caused by non-monotonic behavior at large sizes which we are unable to access with our simulations or because we are extracting $1 + \eta$ from the scaling of $\langle M^2 \rangle$ where η is small compared to unity. The critical fluctuations can be characterized by the ratio $\frac{\langle M^4 \rangle}{\langle M^2 \rangle^2}$, which is used in the Binder Cumulant, and is a universal number for the 3D XY universality class, up to a factor dependent on the spatial anisotropy. We find this ratio to be 0.532(1) for $q = 6$ and 0.524(3) for q=5, which is particular to the boundary conditions used in our simulation but carries universal information about the critical fluctuations. We also find that the U(1) symmetry breaking observable ϕ_q has a scaling dimension of $\Delta_\phi = 1.4(4)$ for $q = 5$ and $\Delta_\phi = 2.3(3)$ for $q = 6$ (Fig. 3·9), showing that it is irrelevant at the critical point and consistent with the scaling dimensions observed in the 3D classical clock (Lou et al., 2007). We extract this exponent by studying the behavior of the thermodynamic quantity ϕ_q at the Binder Cumulant crossing point as a function of size. Using data from pairs of sizes $(L, 2L)$, we estimate a running

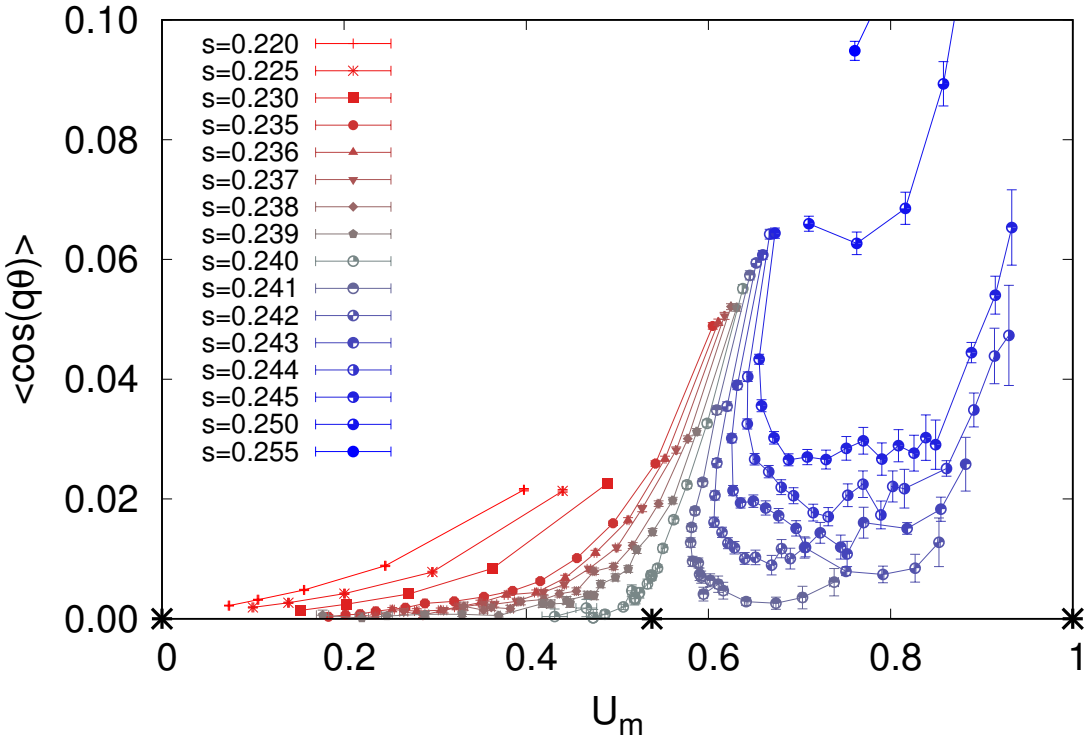

Figure 3·6: Flow diagram for $q = 6$ (ϕ_q vs U_m) showing flows approaching the XY fixed point followed by the Z_q fixed point. The stable point (0,0) is marked here along with the unstable points (0.532,0) and (1,0).

exponent $\Delta_\phi(L)$ and extrapolate it to $\Delta_\phi(\infty)$ which gives us the thermodynamic value.

Emergent symmetry has been known to coexist with two length scales in an order to order transition in quantum magnets at a deconfined quantum critical point (Shao et al., 2016). Our system possesses an emergent symmetry in a simpler set up and some semblance of two length scales, although we do not see anomalous scaling at the critical point as seen at the deconfined point. One of the most direct probes of the two length scales is the domain wall energy. It was predicted (Senthil et al., 2004) and found numerically (Shao et al., 2016) that the domain wall energy for a 2D system

with two length scales ξ and ξ' follows

$$\Delta E \sim (\xi\xi') \tag{3.4}$$

for the deconfined quantum critical (DQC) point. As discussed in Ref. (Shao et al., 2016), the second length scale can correspond to either a dangerously irrelevant operator (Léonard and Delamotte, 2015) in general or the size of a deconfined spinon in the particular case of deconfined quantum criticality. It has been found that the classical 3D clock model shows a length scale associated with the dangerously irrelevant operator (Shao et al., 2016) which does not lead to strong corrections of the critical exponents as seen at the DQC point. We use the domain wall energy to investigate which category the quantum clock model falls into. Following the treatment in Ref. (Shao et al., 2016), we can assume in general that $\xi \sim \delta L^{1/\nu}$ and $\xi' \sim \delta L^{1/\nu'}$. It was found that at the DQC point the length scale ξ', which is associated with the deconfined spinon, saturates to system size for a finite system while the conventional diverging correlation length saturates at $\xi \propto L^{\nu/\nu'}$ with $\nu/\nu' < 1$ for the DQC point. This leads to ΔE scaling as $L^{1+\nu/\nu'}$, compared to the conventional scaling seen for the 3D clock model of L^2 (Shao et al., 2016).

The domain wall energy is calculated by applying open boundary conditions on the 2D lattice which are inconsistent with the ordered state and measuring the excess energy over the ground state with consistent boundary conditions. This quantity is determined using QMC simulations carried out at the critical point, where the correlation lengths begin to diverge and we can extract the scaling exponent from the finite size scaling. For the quantum clock model, we fixed all $\theta_i = 0$ on the left boundary and all $\theta_i = \pi$ on the right boundary while maintaining periodic boundary conditions for the top and bottom boundaries. These conditions allow for a maximum twist for $q = 6$ and would accommodate three domain walls. As we are only interested

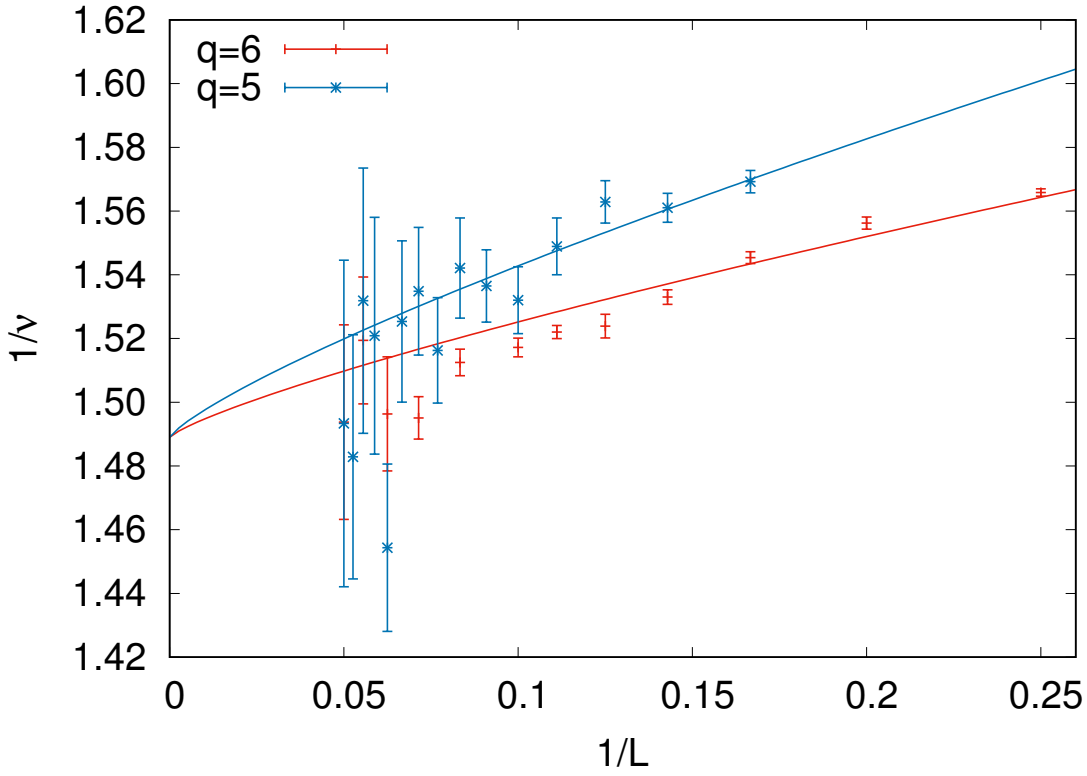

Figure 3·7: ν calculated using the Binder Cumulant crossing method as a function of $1/L$. Fit to $f(x) = aL^{-\omega} + 1/\nu(\infty)$ with values for ω and $1/\nu(\infty)$ taken to be the 3D XY values.

in looking at the domain wall energy scaling, the number of domain walls we engineer in our system is irrelevant and the largest number of domain walls allows us to get the largest energy with relatively small error bars. The excess energy is found to scale with $\Delta_{dw} = 2.27(6)$ for $q = 5$ and $\Delta_{dw} = 2.17(5)$ for $q = 6$ (Fig. 3·10) whereas the conventional finite-size scaling at a continuous phase transition would suggest that both ξ and ξ' must be replaced with L, leading to an exponent of 2. This discrepancy may once again be caused by non-monotonic behavior or because we have used $\omega = 0.8$ following the 3D classical clock model (Shao et al., 2016) instead of the correct irrelevant exponent.

We see no definitive signatures of anomalous scaling here and conclude that we

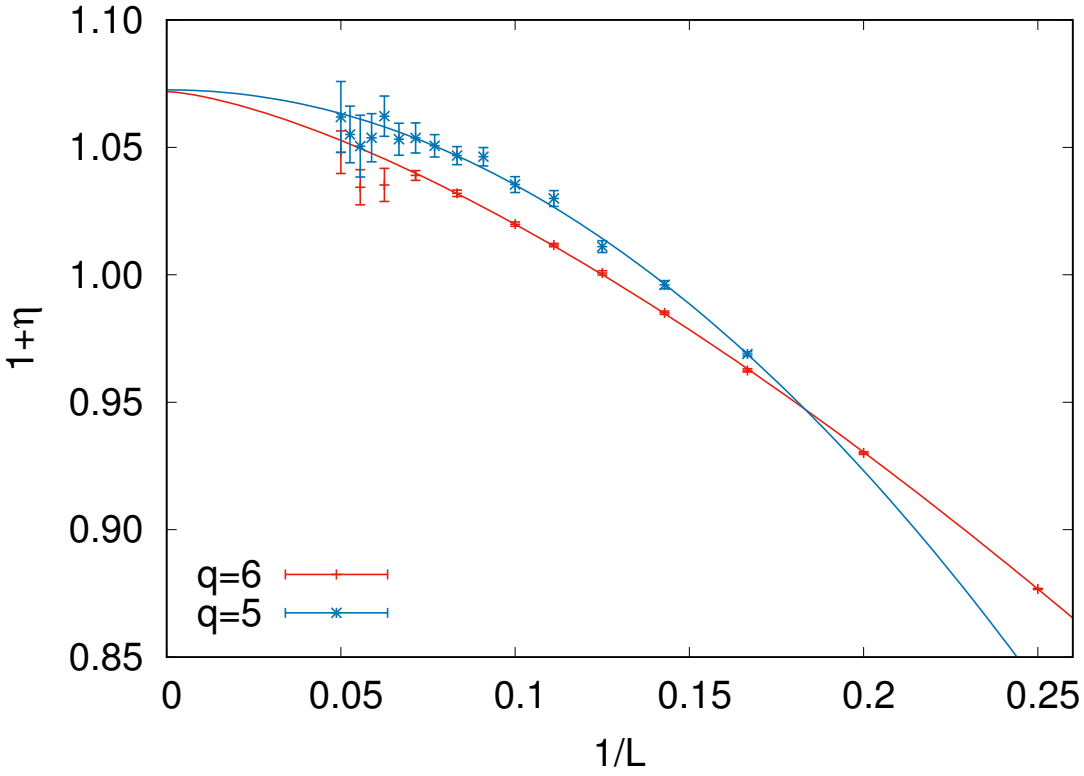

Figure 3·8: $1 + \eta$ calculated using the Binder Cumulant crossing method as a function of $1/L$. Fit to $f(x) = a/L^b + c$ leads to $\eta(\infty) = 0.07(1)$ for $q = 5$ and 6.

need deconfined quantum criticality or an order to order transition to see this effect.

3.3 Robustness and variants

As discussed in the previous section, there are multiple ways of encoding the anisotropy. The model described above is a hard constraint, where a phase on a lattice site can only take q discrete values. We will call this limit the hard clock. This can be contrasted with a "soft" clock model, where the phases are still permitted to take continuous values, along with a potential of the form $\cos q\theta$. This potential forces a preference towards q distinct states. Both these formulations have been checked for the 3D classical clock model and found to be consistent with the predictions from

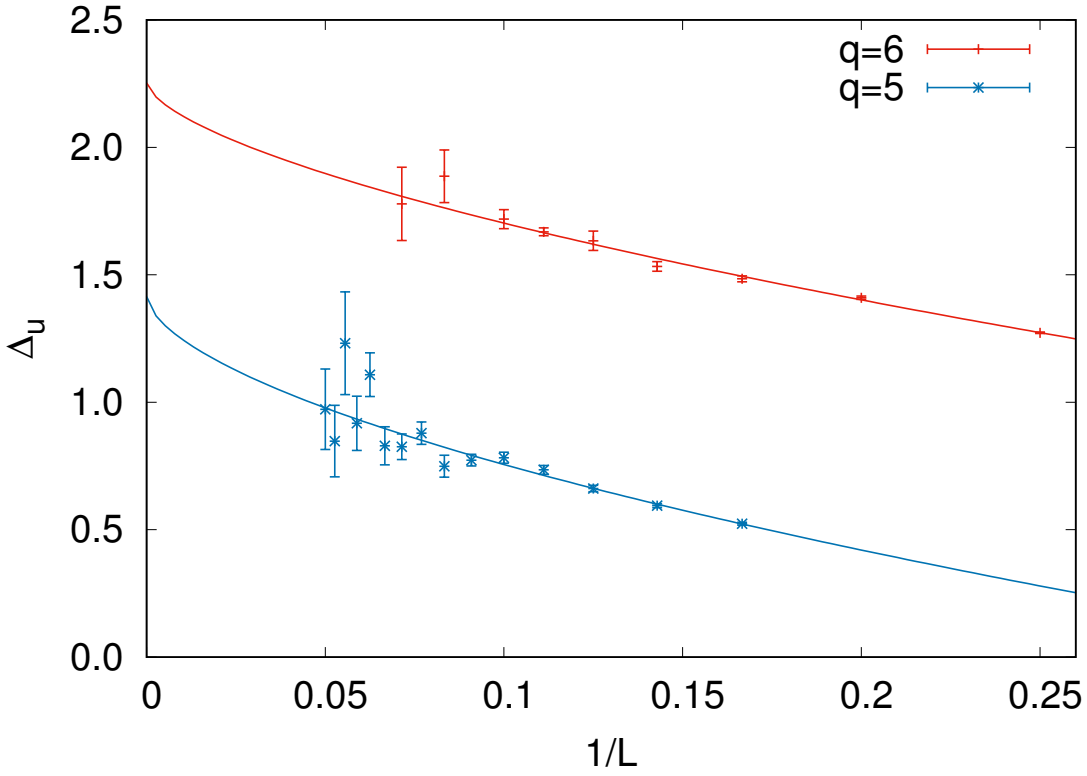

Figure 3·9: Δ_ϕ calculated using the Binder Cumulant crossing method as a function of $1/L$. Fit to $f(x) = a/L^b + c$ leads to $\Delta_\phi(\infty) = 2.3(3)$ for $q = 6$ and $\Delta_\phi(\infty) = 1.4(4)$ for $q = 5$.

RG. This method is used to investigate the lowest q at which emergent symmetry can be theoretically expected, which is $q = 4$. In the formulation of the hard clock, the $q = 4$ case maps on to disconnected copies of the Ising model, leading to a typical continuous phase transition. This can be seen in the following manner. The clock angle θ can be relabeled in terms of the spin-1/2 variables σ and τ with 0 denoting spin down and 1 denoting spin up as follows:

θ	$\sigma\tau$
0	00
$\pi/2$	01
π	11
$3\pi/2$	10

Using this representation, one can see that the $p = 0$ transverse field operator can

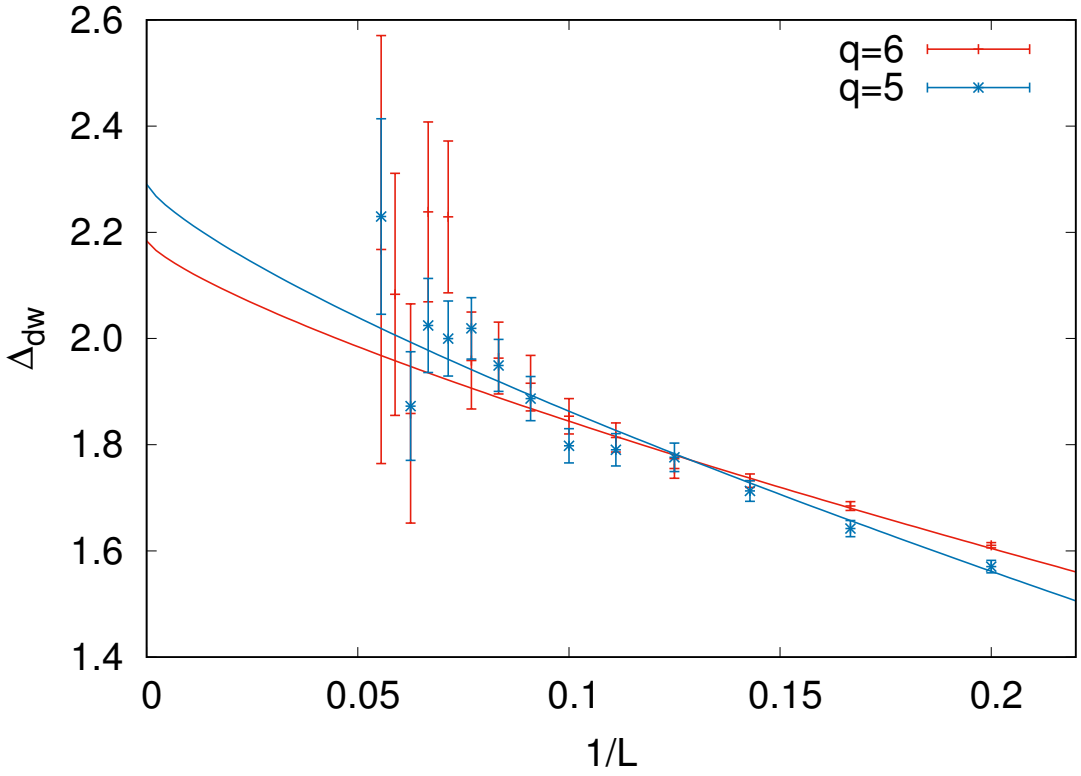

Figure 3·10: Δ_{dw} calculated using the ratio of domain wall energies for pairs of sizes $(L, 2L)$ for varying L. We see that the $\Delta_{dw}(\infty) = 2.17(6)$ for $q = 6$ and $\Delta_{dw}(\infty) = 2.27(5)$ for $q = 5$.

be written as $\sigma_x \otimes I_\tau + \tau_x \otimes I_\sigma$ where $I_{\sigma/\tau}$ is the identity operator for a particular species. Note also that in this language, the matrix elements which connect θ and θ' which are separated by π corresponds to an operator of the form $\sigma_x \otimes \tau_x$. Using these arguments, we can rewrite the $q = 4$ quantum clock Hamiltonian in terms of the Ising variables as

$$H = -\frac{s}{2}\sum_{\langle i,j\rangle}(\sigma_i^z\sigma_j^z + \tau_i^z\tau_j^z) - \frac{1-s}{4}\sum_i(\sigma_i^x + \tau_i^x + \sigma_i^x\tau_i^x). \tag{3.5}$$

From the Hamiltonian above we see the correspondence to two TFI models σ and τ which are completely disconnected and should reproduce the 2D TFIM continuous transition. As the hard clock fails to describe the U(1) transition, we encode a

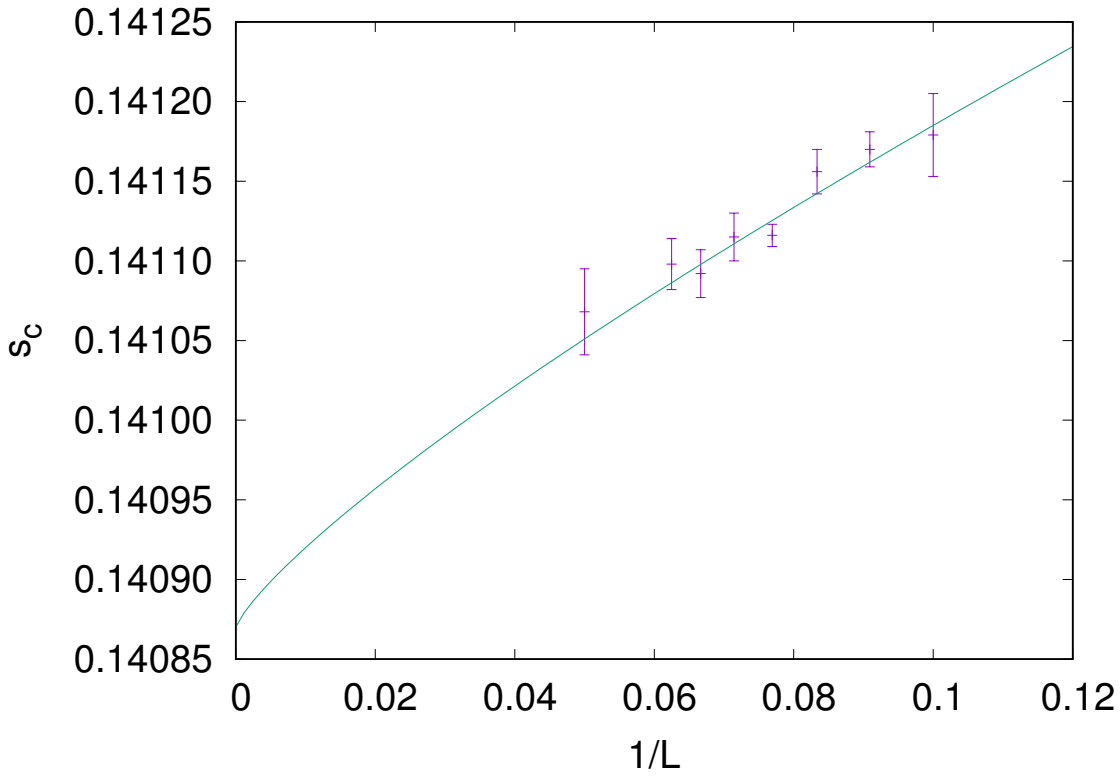

Figure 3·11: s_c calculated using the Binder Cumulant crossing method as a function of $1/L$. Fit to $f(x) = aL^{-\omega} + s_c(\infty)$ leads to $s_c(\infty) = 0.14087(4)$ using $\omega = 0.8$ for the 3D Ising model.

quantum soft clock by using an 8-state quantum hard clock model and elevating 4 states by adding a potential term, leading to the Hamiltonian,

$$H = -s\sum_{\langle i,j\rangle}\cos\left(\frac{2\pi}{q}(\theta_i - \theta_j)\right) - sV\sum_i(\theta_i \mod 2) - \frac{1-s}{q}\sum_i T_i^x. \tag{3.6}$$

For this Hamiltonian, $q = 8$ shows a weak dependence for the scaling dimension of the dangerously irrelevant operator at the critical point, implying that it is either weakly relevant or irrelevant. This is consistent with field theory predictions and numerical investigations, which show that $\Delta_u \approx 0.11$. In this way we see that the soft clock recreates the anisotropy with $q = 4$.

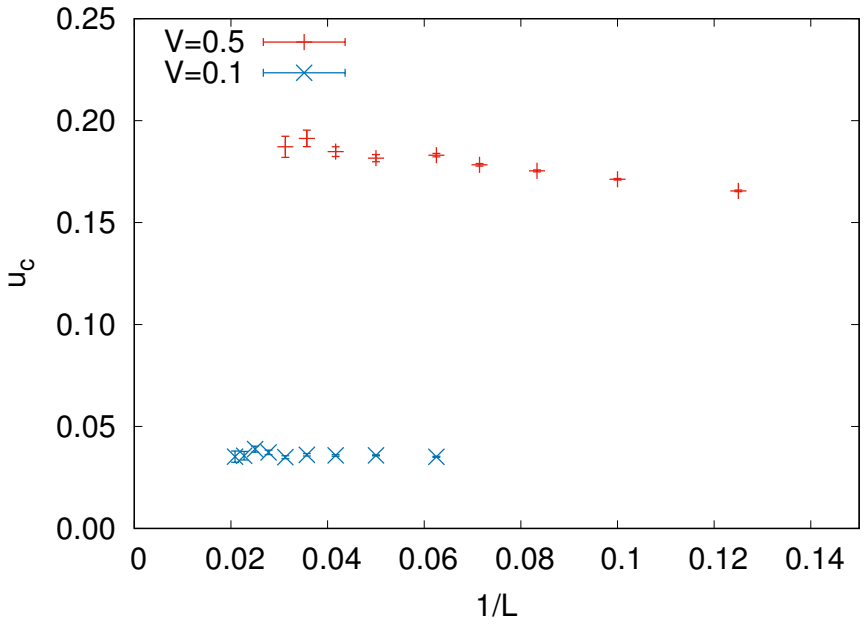

Figure 3·12: Orientational order parameter u as a function of inverse size at the critical point for soft clock model with 8 background states.

3.4 Details of the Monte Carlo method

The design of the quantum Monte Carlo algorithm for this model follows in a manner similar to the transverse field Ising model(TFIM). We use SSEQMC and sample the operator string using two stage updates, the first to switch diagonal operators and the second to move in the space of off-diagonal operators. Following the technique in the TFIM, we add in an identity operator to the Hamiltonian which facilitates exchanges between diagonal and off-diagonal operators. In the case of the TFIM, we had only one diagonal operator, which was the ferromagnetic coupling. By using $-(\sigma_i^z\sigma_j^z + 1)$, we ensured that the antiferromagnetic configuration has a zero matrix element and does not need to be considered. The same must be done to ensure that all ferromagnetic matrix elements have the same sign to avoid the sign problem. For a q-state clock model, it means that $-\cos(\theta_i - \theta_j)$ must be modified so that all the values it can evaluate to have the same sign. This is done by using $-(\cos(\theta_i - \theta_j) + 1)$,

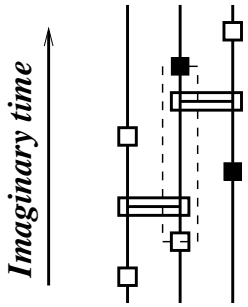

Figure 3·13: Updates which are local in space switch the states along a particular imaginary time string. Filled squares denote the transverse field operator and and the unfilled squares denote the identity operator. Rectangles are ferromagnetic operators.

and now for the q values that $|\theta_i - \theta_j|$ can take, the ferromagnetic term is non-positive.

The TFIM algorithm builds clusters which terminate at the off-diagonal or identity operators and we do the same for the clock model. These clusters can be updated by choosing a global q to shift the states of all the sites in that cluster. Unlike the TFIM, where the cluster spins can be only one of two values, here we have q possibilities, with complicated patterns which can be formed even within clusters. These patterns cannot be modified easily by the global cluster updates, especially for the large clusters which develop at the onset of order. This leads to reduced ergodicity and we use local updates to partially remedy this problem. These local updates work by picking a segment in imaginary time, between two operators which can switch between diagonal and off-digonal matrix elements. These are the identity and the transverse field operators. We first build a string between two consecutive operators of this form, including ferromagnetic operators which may radiate out of the string. Once this is done, a color q is chosen to switch the state in the string with a probability which is consistent with the matrix elements of all operators affected. This creates local differences between spatial regions which may be part of the same cluster. Note that this technique also fails in the ferromagnetic phase as the strings

become very long and the probability to choose a different color for the string becomes small.

Chapter 4

Relationship to Coupled Ising models and Restricted Dynamics

4.1 Fluctuation Coupled Ising Models and Fragmentation

We will introduce the shattering of the Hilbert space and its consequences in the context of a coupled Ising model made out of two Ising species, σ and τ, with the following Hamiltonian:

$$H = -\frac{s}{2}\sum_{\langle i,j\rangle}\left(\sigma_i^z\sigma_j^z + \tau_i^z\tau_j^z\right) - (1-s)\sum_i \sigma_i^x\tau_i^x. \tag{4.1}$$

Here, $\langle i,j\rangle$ refers to nearest neighbors and s is the tuning parameter used to drive the ground state from a paramagnet ($s=0$) to a ferromagnet ($s=1$). This model can also be written using just a single species (σ) which lives on a larger lattice which is two copies of the original lattices connected in a bilayer fashion.

4.1.1 Arbitrary Lattice

We begin by considering a system which lives on an arbitrary lattice in arbitrary dimension and examine the spin degrees of freedom. In the rest of this paper, we shall use 0 to denote the state $\sigma^z(\tau^z) = -1$ and 1 to denote $\sigma^z(\tau^z) = +1$.

Let us label the four possible states in the z-basis on a single site as $\{00, 01, 10, 11\}$ where the first number denotes the state of the σ spin (0 or 1) and the second denotes the τ spin. As the only quantum fluctuation allowed by our Hamiltonian is $\sigma_i^x\tau_i^x$,

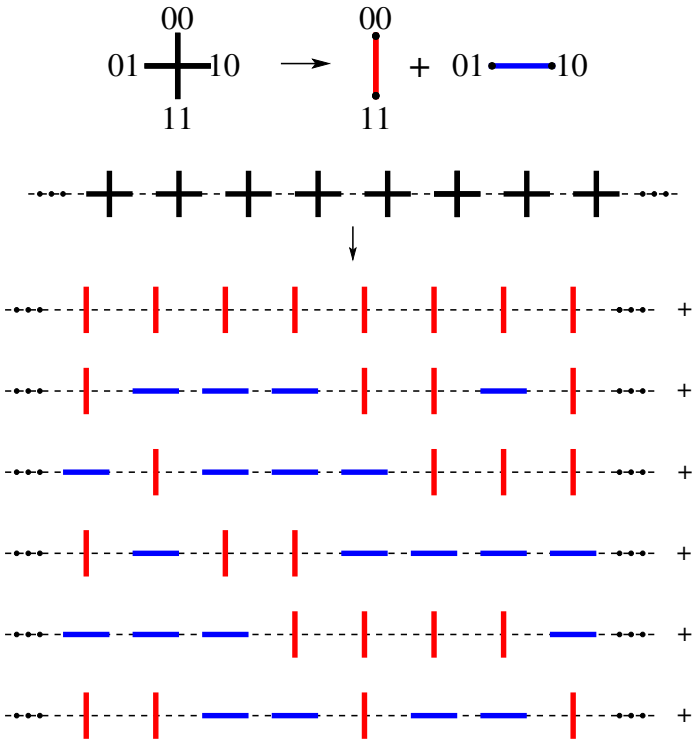

Figure 4·1: The four states at a particular site break into two non-communicating axes as shown above, leading to the Hilbert space breaking into many distinct axis arrangements.

which acts by flipping the state of both σ and τ simultaneously, the four states described above break into two sets $(00, 11)$ and $(01, 10)$ such that states within a set can transform into one another through $\sigma_i^x \tau_i^x$ but states from different sets cannot be connected by any operator in the Hamiltonian. An equivalent way of seeing this is by noticing that $\sigma_i^z \tau_i^z$ commutes with the Hamiltonian for all i, implying that we have a local conserved quantity. This quantity will be used to label the shattered blocks of Hilbert space. We will represent the local splitting pictorially using vertical and horizontal axes (as shown in Fig 4·1) where the vertical axis corresponds to the set $(00, 11)$ and the horizontal axis to $(01, 10)$. As this decomposition can be done for every site on the lattice and assuming that the lattice has N sites, the Hamiltonian then breaks into 2^N blocks, each of which is a $2^N \times 2^N$ matrix. In the language of

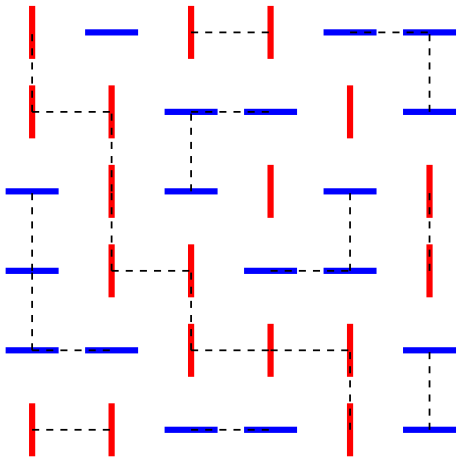

Figure 4·2: An axis arrangement for the square lattice with interacting sites connected by dotted lines.

eigenvalues of $\sigma_i^z \tau_i^z$, each block can be represented as a set of 1's and -1's which denote the value of this operator for each site and there are 2^N sequences of these for N sites. Each block in the Hamiltonian now represents a particular axis arrangement (shown for 1D and 2D lattices in Figs 4·1, 4·2).

We shall describe this phenomenon as the fragmentation or shattering of Hilbert space. Both of these terms have been used in recent work in the context of the eigenstate thermalization hypothesis (ETH) (Sala et al., 2019; Khemani and Nandkishore, 2019) and a similar phenomenon has been studied in disordered Floquet circuits composed of Clifford gates (Chandran and Laumann, 2015). This phenomenon has also been seen numerically for quantum dimer models with restricted dynamics but a similar geometric way to understand the same has not been identified in that context (Sikora et al., 2011).

The classical term in our Hamiltonian allows us to treat adjacent sites with states on different axes as effectively non-interacting. For example, consider the state 00 on site i and the state 11 on site j, where i and j are nearest neighbors. The energy cost of such an arrangement due to the classical term $-(\sigma_i^z \sigma_j^z + \tau_i^z \tau_j^z)$ is -2 (in units

of the ferromagnetic coupling). The same argument can be made for set of states $(01, 10)$. If site j hosts one of the states from the horizontal axis, i.e. 01 or 10, the energy associated with the arrangement of states on i and j will always be 0, as one of the bonds (either $\sigma\sigma$ or $\tau\tau$) is always broken while the other is always satisfied. This implies that, from energy considerations, states 01 and 10 are equivalent if site i hosts 00. This argument can be repeated for all combinations of states as long as the states on sites i and j belong to different axes. From this analysis it follows that, if nearest neighbor sites i and j host the same axes, then they have an Ising bond of strength s between them, else, they are non-interacting. If we now consider a typical axis arrangement (corresponding to a block) as shown in Fig. 4·2 for a 2D lattice, we see that the system has essentially broken into several smaller Ising models which co-exist on the lattice. For simple regular lattices, such as a 1D chain, square or cubic lattice with periodic conditions, the axis arrangements can be related to the partitions of natural numbers (Andrews, 1994; Sándor, 2004). This connection will be later illustrated using a periodic chain.

One of the key features of the fragmentation of real space into components is that the correlation length in a particular block in bounded by the spatial extent of the largest clusters in the corresponding axis arrangement. This feature depends crucially on the restricted dynamics from the $\sigma_i^x \tau_i^x$ and the classical term allowing a degeneracy in states. If the classical term were to be augmented by adding an interaction of the form $-\sigma_i^z \tau_j^z$, the non-interacting nature would be lost as the state 00 on site i would now prefer 10 on site j over 01. Due to this term, each spin species has a global pattern specific to which sector the state belongs to and fluctuations would occur around this pattern in the large s limit. The maximal correlation length in every sector grows to system size in this limit although the details of this growth depend on the structure of the particular sector. This illustrates that although the quantum term determines the

sector structure, interacting units within a sector may be controlled by the choice of classical terms. Careful choice of tuning parameters can also create a scenario where there are two length scales, one associated with the growth of correlation within a component and the other with the growth across components. If we were to require that the symmetry in $\sigma \to \tau$ be maintained, an additional term would be have to be added to ensure that the state 00 does not favor one of 01 or 10, and the physics would again be the same as the Hamiltonian in Eq. (4.1).

As an axis arrangement can be thought of as a configuration where each site is assigned either a vertical or a horizontal axis with probability half it can also be written in terms of a percolation problem where a particular site is occupied if the axis assigned to it is vertical or left empty if the axis is horizontal. If the percolation threshold for the particular lattice is below 1/2, most axis arrangements will form a giant component and this may have consequences on the correlation length as far above the percolation threshold, almost all axis arrangements will now have diverging length scales, leading to a continuous transition. The universality class for the transition may relate to those of diluted Ising models which are above the percolation threshold, which have been studied in the context of thermal and quantum phase transitions (Heuer, 1993; Senthil and Sachdev, 1996; Sandvik, 2006). We are unable to study this in the context of the periodic chain as the percolation threshold in 1D is unity, which means none of the axis arrangements will percolate except the two axis arrangements which correspond to all sites having the same choice of axis. This feature also extends to the dynamics of our system. As the dynamics generated by $\sigma_i^x \tau_i^x$ cannot take a state out of its corresponding axis arrangement, the system remains broken into a sum of smaller pieces. In 2D and higher, these broken pieces would in general form non-integrable pieces which thermalize within their boundaries but not with the entire system. This implies that the system would

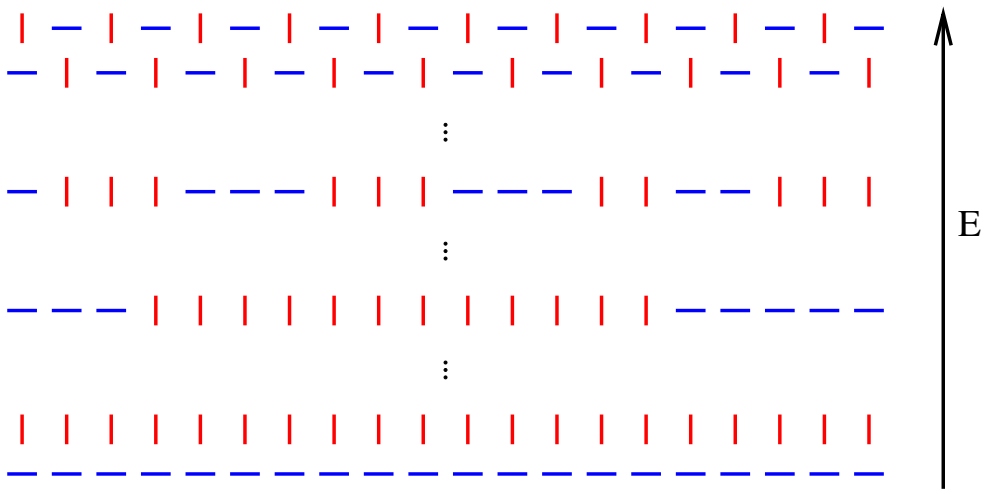

Figure 4·3: Axis arrangements sorted by energy with reference blocks making up the lowest energy region and energy increasing bottom to top.

not reach a thermal distribution and not show characteristics such as volume law entanglement entropy which would be expected of thermalizing systems.

4.1.2 Periodic Chain

Now we specialize to the periodic chain and consider the eigenstates and eigenenergies for various s. In the ferromagnetic limit ($s = 1$), the lowest energy belongs to two blocks, one with all axes vertical and the other with all axes horizontal. We shall call these two blocks as the reference blocks for this model, as they are the easiest to analyze and map exactly to the simple transverse field Ising chain. These blocks have N activated bonds, whereas all other blocks have at least one pair of nearest neighbor sites with differing axes, leading to loss of the energy which could potentially be gained from that Ising bond. The first excited level in the ferromagnetic limit is made out of all blocks with axis arrangements which break up into two pieces, one with all axes vertical and the other with all axes horizontal, as these arrangements have $N - 2$ activated bonds. In the limit of $s = 0$, all the Ising bonds are switched off and all 2^N blocks are degenerate. The axis arrangement of any block can be seen

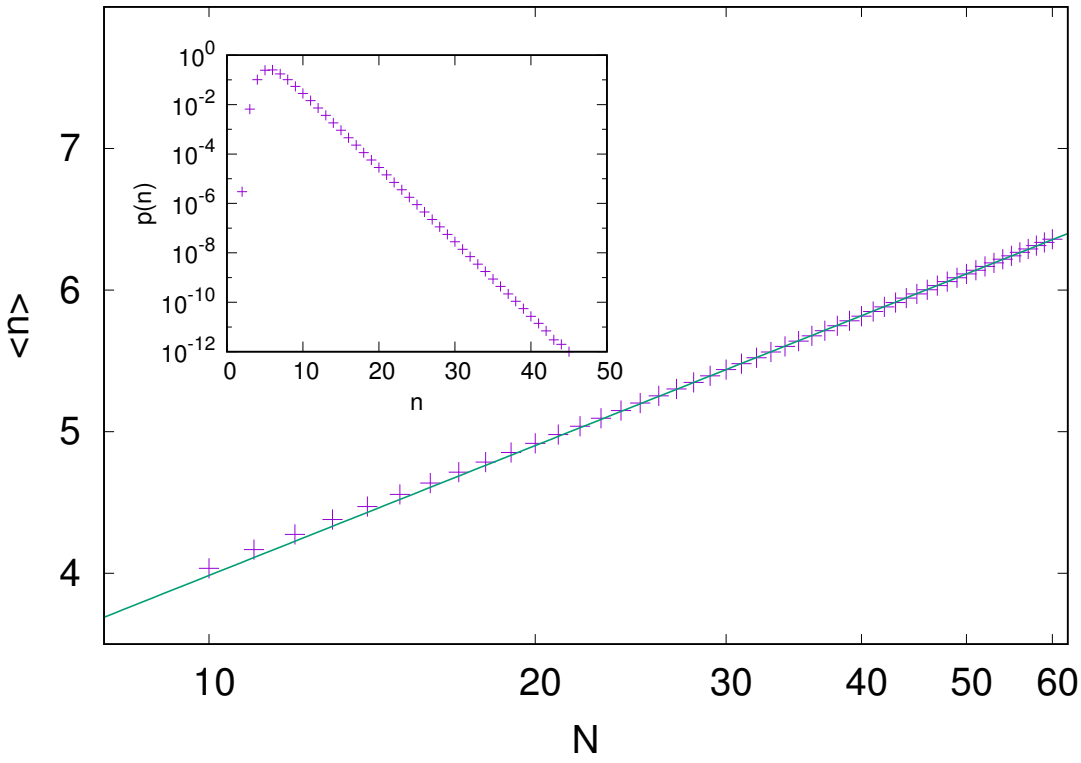

Figure 4·4: Average size of the largest piece in a block plotted as a function of the system size N and fit to the form $\langle n \rangle \approx a + b \log(N)$ with $b = 1.33(1)$. Inset: The probability distribution of the size of the largest piece, which shows an exponential tail.

as a sum of independent Ising chains of various lengths as sites with differing axes are non-interacting (Fig 4·3). As the energy density of a longer Ising chain is always larger in magnitude than a shorter chain for all s other than $s = 0$ and $s = 1$, the reference blocks, which comprise of a single periodic chain of length N, always form the lowest energy manifold.

As each block can be made up of many smaller chains, the energy spectrum for this Hamiltonian hosts a large amount of degeneracy. This can be understood by recognizing that many blocks share the same number and sizes of chains, and each block carries a different ordering of the chains. As the energy of a block is simply the sum of the energies of individual chains, the arrangement of chains that makes up a

particular block does not play a role in calculating the energy; only the number and sizes of chains control the energy. Following this line of thought, we can now map our energy spectrum to the sorted partitions of the natural number N, where each partition is defined as a set of smaller pieces whose lengths sum to N. For example the sorted partitions for $N = 4$ are:

$$4 = 3 + 1 = 2 + 2 = 2 + 1 + 1 = 1 + 1 + 1 + 1 \tag{4.2}$$

It was shown (Hardy, 1999) that the number of partitions $p(N)$ of a natural number N asymptotically behaves as $\log p(N) \approx C\sqrt{N}$ with $C = \pi\sqrt{2/3}$. Due to periodic boundary conditions, the only allowed partitions for the axis arrangements are those which have an even number of pieces. It follows that the number of energy levels in addition to the reference level are the number of even partitions of the number N. We observe that this number quickly approaches half the asymptotic value for $N \geq 10$. If we now consider a particular block and study the growth of its correlation length as we change s from the paramagnetic regime to the ferromagnetic regime, we would find that the correlation length grows until it reaches an upper bound which must be smaller than the largest piece in the partition corresponding to that block. If the largest piece is much smaller than system size the ground state of this block can never develop long range order. The statistics of different blocks along with their energies now controls how much they contribute to the ground state of the total system in the presence of a temperature or quantum fluctuation which allows them to mix.

An added level of complexity is brought in by observing that each partition of the number N corresponds to a different number of axis arrangements, i.e, blocks. We find numerically that the average size, $\langle n \rangle$, of the largest piece in the axis arrangement corresponding to a random block follows the relation $\langle n \rangle = a + b\log(n)$ (Fig 4·4). We also study the probability distribution of the size of the largest piece in a random

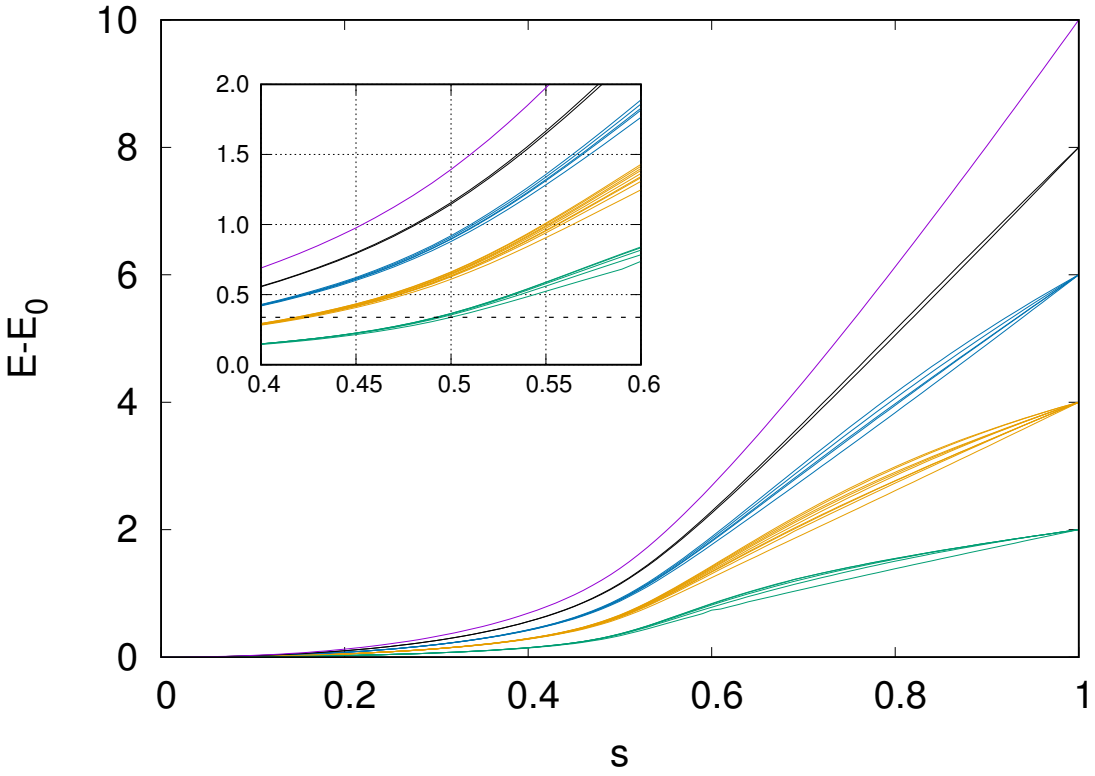

Figure 4·5: Energy levels for the Hamiltonian defined in Eq. (4.1), as a function of tuning parameter s, seen to converge in $s = 0$ limit and approach the spectrum of the classical Ising chain in $s = 1$ limit. Inset: The level diagram around $s = 0.5$ shows a minimum gap of ≈ 0.34.

block chosen with uniform probability and find exponential tails for $p(n)$ for $n > \langle n \rangle$ (shown in inset of Fig 4·4 for a 60 site chain). This suggests that, if the system is allowed to choose a block at random, the largest piece in the chosen block will be much smaller than system size with a probability $\to 1$, thus leading to a severe limitation on the growth of correlation length.

The probability distribution with which the system samples different blocks depends on the terms connecting different blocks and the relative ground state energies of different blocks. As discussed above the ground state of the entire system is always made out of the two blocks which have all axes vertical or all axes horizontal. The opposite limit is again made up of just two blocks, which are the blocks where all

axes are anti-aligned with their neighbors (Fig 4·3). Each of these breaks into N disconnected spins, as no nearest neighbor spins have a ferromagnetic bond between them. This implies that every spin is polarized in the x-direction due to the $\sigma^x\tau^x$ term with an energy of $-s$, making the total energy of the state $-Ns$. We can assume that the ground state energy for the reference blocks can be written as $-N\epsilon(N,s)$ where $\epsilon(N,s)$ is the energy density for a periodic chain of length N at tuning parameter value s. These two extremes set the range of energies which can be occupied by all other blocks. Another general trend to be expected from the lowering of energy due to larger system size would be to have partitions with the largest pieces occupy lower energy levels (Fig. 4·3). As we have seen from the distribution of partitions, these levels would contain a relatively small number of blocks due to the large pieces they must contain. Also, all the energies must converge in the $s = 0$ limit, as the ferromagnetic term switches off, leaving all blocks equivalent in energy.

The above gives us a fair idea of the energy level diagram and we present a detailed study of the $N = 10$ case in Fig. 4·5, obtained using Lanczos diagonalization, which captures the essential features. An important region of the energy level diagram is $s \approx 0.5$ as the simple Ising chain undergoes a continuous quantum phase transition at this point. In an Ising chain, the correlation length grows continuously with increasing s for $s < 0.5$ and at the transition the correlation length reaches the system size. If the gap to a large number of blocks vanishes at this point, the correlation length would acquire large contributions from the other blocks in the presence of arbitrarily small coupling across blocks, which would lead to a capping on the correlation length. As the gap must once again open in the ferromagnetic regime, the system will drop back into the fully polarized state with large correlation length. This mechanism can create a jump in the correlation length, which is a hallmark of a first order phase transition. This is a heuristic argument which does not take into account the nature

of the coupling to other blocks. Using our Lanczos diagonalization analysis, we find that this gap converges to a finite value with increasing size. This is expected for higher dimensions as well, as the lowest block above the ground state block must necessarily have at least one missing ferromagnetic bond which contributes a finite amount to the energy.

4.1.3 Fluctuations between blocks and block mixing

One of the easier ways to allow the system to access all possible blocks would be to couple it to a thermal bath which provides an inverse temperature β. Assuming that the ground state energies of all the blocks is $O(N)$ (which we see is an upper bound from the energy level diagram), the contribution of the blocks with relatively small pieces or "restricted" blocks (Z_r) in the partition function is $Z_r = e^{-\beta E} D_r$, where D_r is the degeneracy of the blocks. As we have seen that this degeneracy$\rightarrow 2^N$ and $E \propto N$, a finite β is not sufficient to suppress these levels, and there can exist a range of temperatures where these levels can mediate a transition with limited correlation length, i.e, a first order transition. Finite temperature would allow thermal fluctuations which can jump across blocks and in this way wash out the block structure as well. This cannot be studied in our analysis of the 1D chain as it is known that any non-zero temperature leads to disorder in the Ising chain and the phase transition is thus completely washed out. For higher dimensional systems this mechanism can lead to interesting crossover physics between the continuous quantum phase transition and the thermal phase transition of the classical system expected at any finite temperature. A coupling across blocks can also be achieved by a weak global transverse field and a perturbation theory approach may be used to study this. More powerful numerical results, which layout the entire phase diagram in the presence of a transverse field, are presented in the following section.

4.2 Perturbations and Ashkin-Teller Criticality

We now connect the different blocks using a weak perturbation which allows axis flipping. In spin language this corresponds to a global transverse field, leading to a Hamiltonian of the form

$$\begin{aligned} H =& \frac{-s}{2} \sum_{\langle i,j \rangle} \left(\sigma_i^z \sigma_j^z + \tau_i^z \tau_j^z \right) \\ & - (1-s) \sum_i \left[p \sigma_i^x \tau_i^x + (1-p)(\sigma_i^x + \tau_i^x) \right]. \end{aligned} \tag{4.3}$$

The $\sigma^x(\tau^x)$ operator switches $00 \to 10$ $(00 \to 01)$, effectively changing the axis at that particular site. In the weak perturbative limit of $(1-p) \ll 1$, this can be seen as connecting blocks which only differ in a few axis arrangements, i.e those which have similarly sized pieces in a similar arrangement. For smaller p, blocks which have pieces of substantially different sizes would begin to couple as well, which would imply that the bound on the correlation length would weaken as the system can now build in longer correlations through a combination of blocks for the same value of s. In the opposite limit of $p \to 0$, blocks are strongly coupled, and the system can also be seen as two copies of transverse field Ising models. This suggests that the system would undergo a continuous transition, which would be in the Ising universality class of the appropriate dimension.

For $p = 1$, the ground state sector is exactly a transverse field Ising model on the appropriate lattice. In this limit, for all $s \in [0,1]$, $M_{\sigma\tau} = \frac{1}{N} \sum_i \sigma_i^z \tau_i^z = \pm 1$ as the axes are perfectly ordered implying all $\sigma_i^z \tau_i^z$ are either +1 or -1 for the horizontal or vertical axes. For $s \to 1$, σ^z and τ^z are each disordered and with reducing s, they undergo an Ising transition where they develop long range order. For $p < 1$, at $s = 0$ the paramagnet phase has no long range order in axis arrangements or either of the spin species as the perturbation allows complete access to Hilbert

space. The conditions describe three phases, 1) complete paramagnetic phase with $\langle M^2_{\sigma\tau}\rangle = \langle M^2_{\sigma}\rangle = \langle M^2_{\tau}\rangle = 0$, 2) axis ordering with $\langle M^2_{\sigma\tau}\rangle \neq 0, \langle M^2_{\sigma}\rangle = \langle M^2_{\tau}\rangle = 0$, and 3) ferromagnet with $\langle M^2_{\sigma\tau}\rangle \neq 0, \langle M^2_{\sigma}\rangle = \langle M^2_{\tau}\rangle \neq 0$. These three phases are also described by the Ashkin-Teller (AT) model (Delfino and Grinza, 2004), where phase 2 is called the polarization ordered phase. The Hamiltonian for the AT model is

$$H = -J\sum_{\langle i,j\rangle}\sigma^z_i\sigma^z_j - J\sum_{\langle i,j\rangle}\tau^z_i\tau^z_j - K\sum_{\langle i,j\rangle}\sigma^z_i\tau^z_i\sigma^z_j\tau^z_j, \tag{4.4}$$

and the phase diagram as a function of $\frac{J}{T}$ and $\frac{K}{T}$ contains the above mentioned phases. The arguments presented until this point in this section are valid for general lattices in all dimensions.

In 2D, the AT model is fairly well studied from a theoretical viewpoint (Delfino and Grinza, 2004). It was found that for $K > J$ and $J > 0$, the system passes through two phase transitions; from the paramagnet to polarized state and from the polarized state to the ferromagnet. Both these transitions are Ising-like as a Z_2 symmetry is broken each time. At $K = J$, the polarized state vanishes, and we have a direct transition from the paramagnet to the ferromagnet. The universality class at this point is that of the $q = 4$ Potts model in 2D. For $0 < K < J$, the system interpolates smoothly between two disconnected Ising models ($K = 0$) and the $q = 4$ Potts model. Along this interpolation, some of the critical exponents, such as the scaling dimensions of the polarization operator and the energy density, vary smoothly (Cardy, 1987). This is expected as the energy density coupling between the two species caused by the four spin term is marginal in 2D and allows a smooth flow under a conformal field theory description (Gorbenko et al., 2018).

We check for a similar behavior in the coupled quantum Ising model on a periodic chain, which is expected to map to the AT model through the d-dimensional quantum to d+1-dimensional classical mapping as σ^x corresponds to an energy term of the form

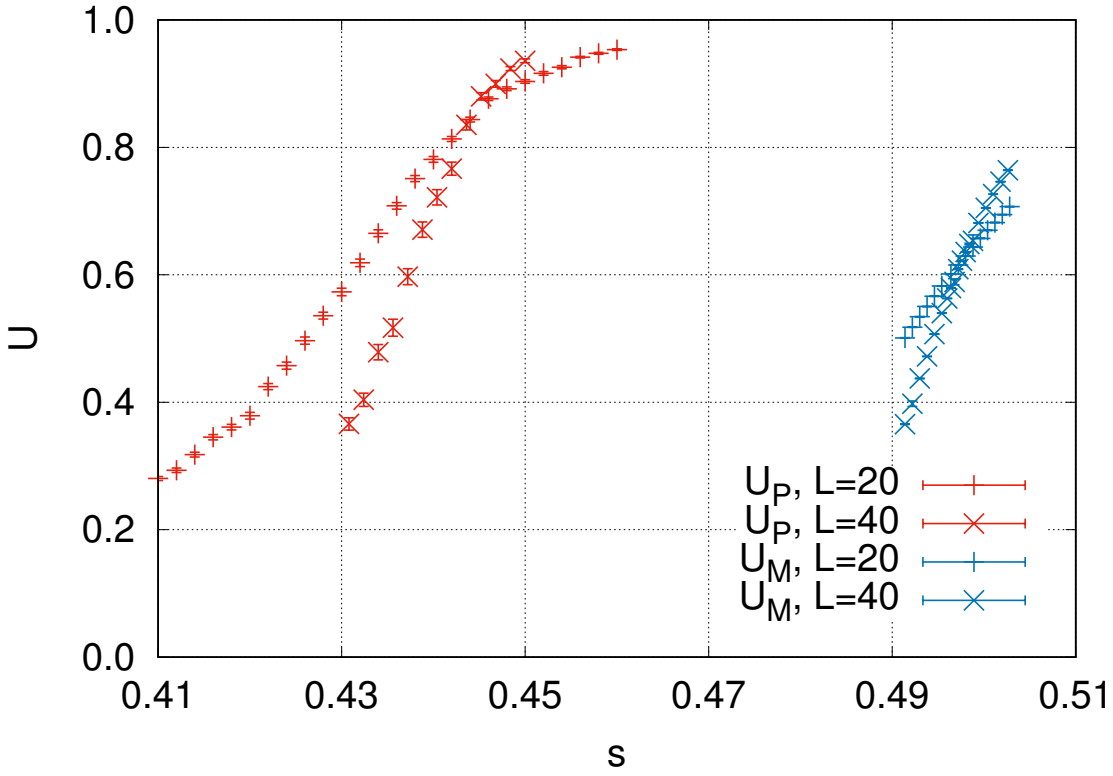

Figure 4·6: Binder cumulant as a function of s with crossing points showing approximate locations of the two transitions at $p = 0.95$. P stands for the polarization and M for the magnetization. Crossing points of U for large sizes approximate critical points for these transitions.

$\sigma_i^z \sigma_{i+1}^z$ in the imaginary time direction when written in the path integral language. We use stochastic series (SSE) expansion quantum Monte Carlo (QMC) (Sandvik, 1999) as it is a powerful and unbiased method of extracting thermodynamic expectation values for such systems.

The $p = 0$ limit corresponds to the $K = 0$ limit of the AT model and describes decoupled Ising models. The $p = 1$ limit has no paramagnetic phase and at some intermediate p_P, we would expect $q = 4$ Potts criticality. For $p < p_P$, the system would trace out the line of continuously varying exponents and for $1 > p > p_P$, it would host all three phases along with two Ising transitions; one between the paramagnetic

and polarized phases and the other between the polarized and ferromagnetic phases. To investigate these phase transitions, we define a Binder cumulant (Binder, 1981) with coefficients corresponding to Z_2 symmetry breaking, as

$$U_M = \frac{3}{2}\left(1 - \frac{1}{3}\frac{\langle M^4 \rangle}{\langle M^2 \rangle^2}\right), \tag{4.5}$$

where M can denote either $M_{\sigma\tau}, M_\sigma$ or M_τ. In the regime where we have two Ising phase transitions, the Binder cumulant is by this definition zero in the paramagnetic phase and unity in the ordered phase, for whichever order parameter is considered. There is a sharp transition in U_M at the phase transition for large sizes and we need to study only one of M_σ or M_τ as they are identical. By tracking $U_{M_{\sigma\tau}}$ and U_{M_σ}, we notice two transitions for $p = 0.95$ (Fig. 4·6) at distinct values of s. This is expected for values of p close to 1 until a point at which the $q = 4$ Potts point is realized. The scaling dimension of the spin operator is fixed at $\Delta_\sigma = 1/8$ (which is the 2D Ising value) along the critical line joining the $p = 0$ and $p = p_P$, whereas the polarization operator has $\Delta_{\sigma\tau} = \Delta_\sigma + \Delta_\tau$ at the decoupled point and $\Delta_{\sigma\tau} = \Delta_\sigma = \Delta_\tau$ at the Potts point. The critical exponent ν varies from 1 (Ising value) to 3/2 (Potts value) along this line. From our simulations and finite size scaling analysis following the method presented in Ref. (Luck, 1985), we observe that, at $p = 0.75$, $\nu = 1.41(5)$ and $\Delta_{\sigma\tau} = 0.13(1)$, indicating that this point is quite close to the Potts point (as can be seen in our approximate phase diagram, Fig. 4·7). The value of ν may be somewhat affected by logarithmic corrections expected in the exponents at the Potts point. The same extrapolation at $p = 0.50$ gives us $\nu = 1.21(1)$ and $\Delta_{\sigma\tau} = 0.17(1)$, which are values between the two extremes. This analysis shows us in a conclusive manner that the system flows to the AT universality class in the thermodynamic limit.

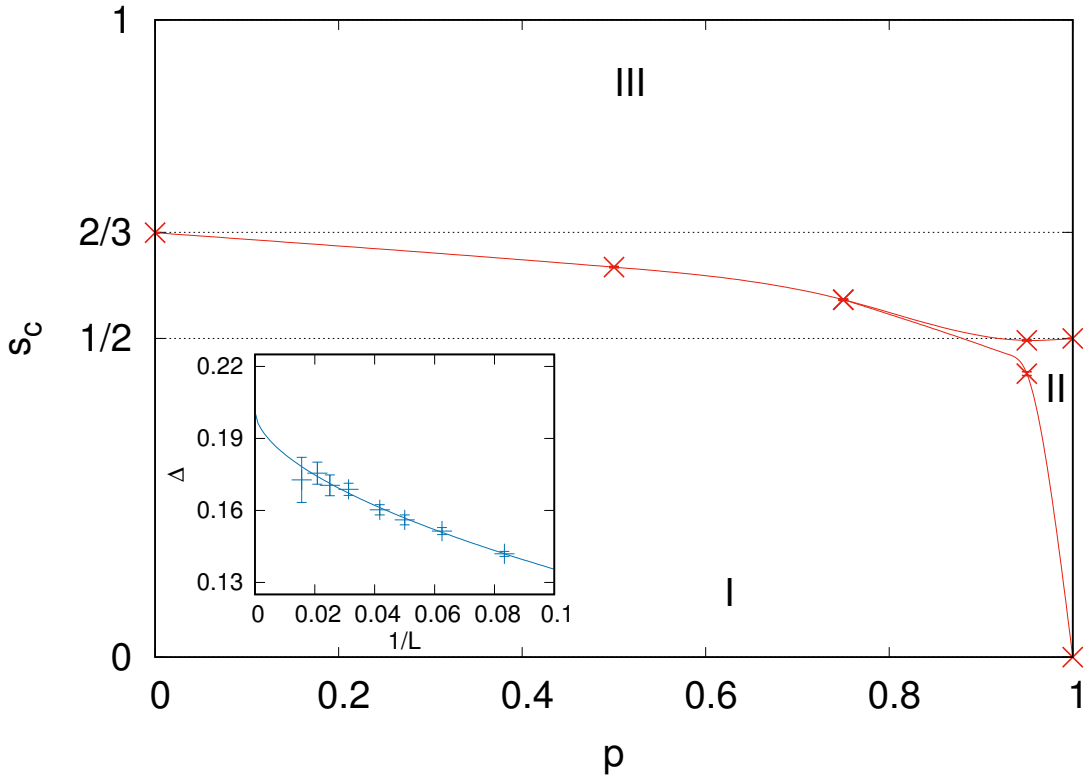

Figure 4·7: Phase diagram of the model described by Eq. (4.3) with phases I. paramagnet, II. polarization ordered and III. ferromagnet with the AT line of continuously varying exponents from $p = 0$ to $p \approx 0.75$. Inset: Polarization exponent $\Delta_{\sigma\tau}(1/L)$ for $p = 0.5$ extrapolated to $\Delta_{\sigma\tau}(0) = 0.20(1)$.

4.3 Relation to Pseudo-first Order Behavior

The Binder cumulant is used in general to identify the nature of a phase transition and the critical exponent ν for the correlation length (extracted from the slope). Non-monotonic behavior in the Binder cumulant involving a minima is usually taken as a signature of a first-order transition, although this can only be confirmed by checking that the value of this negative peak diverges as L^d (Binder, 1987). A dip in the Binder cumulant has been misinterpreted to signal a first order transition for the frustrated J_1-J_2 Ising model on the square lattice where nearest neighbors

interact with a ferromagnetic bond of strength J_1 and next nearest neighbors with an antiferromagnetic bond of strength J_2 (Jin et al., 2012). In this model there exists a phase transition between a Z_4 symmetric striped phase and a paramagnetic phase with increasing temperature. The dip was taken to represent a first order transition until a detailed numerical study by Jin *et al.* (Jin et al., 2012) showed that the cumulant dip mapped onto the $q = 4$ Potts model, which also shows non-monotonicity with a negative dip which does not diverge. The reason for this behavior was traced to the shape of the distribution at the critical point for these models (Sandvik, 2010b) and it was noticed that phase coexistence was not seen, which would be a characteristic of a first order transition.

Here we present the same kind of analysis for our model and argue that the negative peak arises from an inappropriate definition of the Binder cumulant when investigating multiple phase transitions. The Binder cumulant may evaluate to different values in different phases and if the phases are not well understood, this behavior can be interpreted as arising from a first order transition. Even at special points such as the Potts point ($K = 1$ point in the AT model), which is known to harbor a continuous phase transition between trivial paramagnetic and ferromagnetic phases, remnants of the polarization ordered phase cause non-monotonic behavior in the Binder cumulant. We will explicitly observe this kind of remnant here.

If we consider the $p = 0.95$ phase transitions presented in the previous sections, we see that in the paramagnetic phase, the Binder cumulant can be defined as

$$U_M = 2 - \frac{\langle M^4 \rangle}{\langle M^2 \rangle^2}, \tag{4.6}$$

instead of the definition used in Eq. (4.5), because the magnetization can now be defined as a vector $\boldsymbol{M}=M_x\hat{x} + M_y\hat{y}$, where $M_x(M_y)$ is the magnetization along the vertical (horizontal) axis. This definition leads to $U_M = 0$ for the paramagnetic phase

and $U_M = 1$ for the ferromagnetic phase and is used for decoupled Ising systems as well as systems with XY symmetry. Importantly, however, this definition of U_M evaluates to -1 in the polarization ordered phase as a global axis is chosen and only constrained Ising like fluctuations are allowed along this axis forcing $\langle M^4\rangle/\langle M^2\rangle^2$=3, which can be calculated assuming Gaussian probability distributions arising from the central limit theorem. If we use Eq. (4.6) for the entire range of s at $p = 0.95$, in the thermodynamic limit, we would expect a region where $U_M = 0$, a region with $U_M = -1$ and a region with $U_M = 1$. A schematic of this is shown in the inset of Fig. 4·8. For small sizes U_M changes gradually and these values are not reached exactly.

From Fig. 4·6 and further extrapolations, we note that the paramagnetic to polarization ordered transition occurs at $s = 0.44(1)$ and the polarization ordered to ferromagnetic one occurs at $s = 0.497(1)$. Following the behavior of U_M as defined above, we find a non-monotonicity in the polarized phase where the dip extrapolates to -1 (Fig. 4·8). We also study the histograms of the order parameter $\boldsymbol{M}$ and clearly see the aligning of the polarization in Fig. 4·9.

These histograms are similar to those seen at the Potts point in the J_1-J_2 model. We have checked this in the more natural formulation of the $q = 4$ Potts model on a 2D square lattice, with a Hamiltonian given by

$$H = -\sum_{\langle i,j\rangle} \delta_{q_i,q_j} = -\sum_{\langle i,j\rangle} \cos(\theta_i - \theta_j), \tag{4.7}$$

where $q_i \in \{0, 1, 2, 3\}$ are the possible states and which can be represented as unit vectors forming a regular tetrahedron, implying the equivalence of the two terms in Eq. (4.7) up to a global shift in the baseline for energy. As mentioned above, if the fluctuations in the thermodynamic magnetization are Ising like then $r = \langle M^4\rangle/\langle M^2\rangle^2 = 3$ and if they are completely paramagnetic $r = 5/3$, which can be seen by evaluating

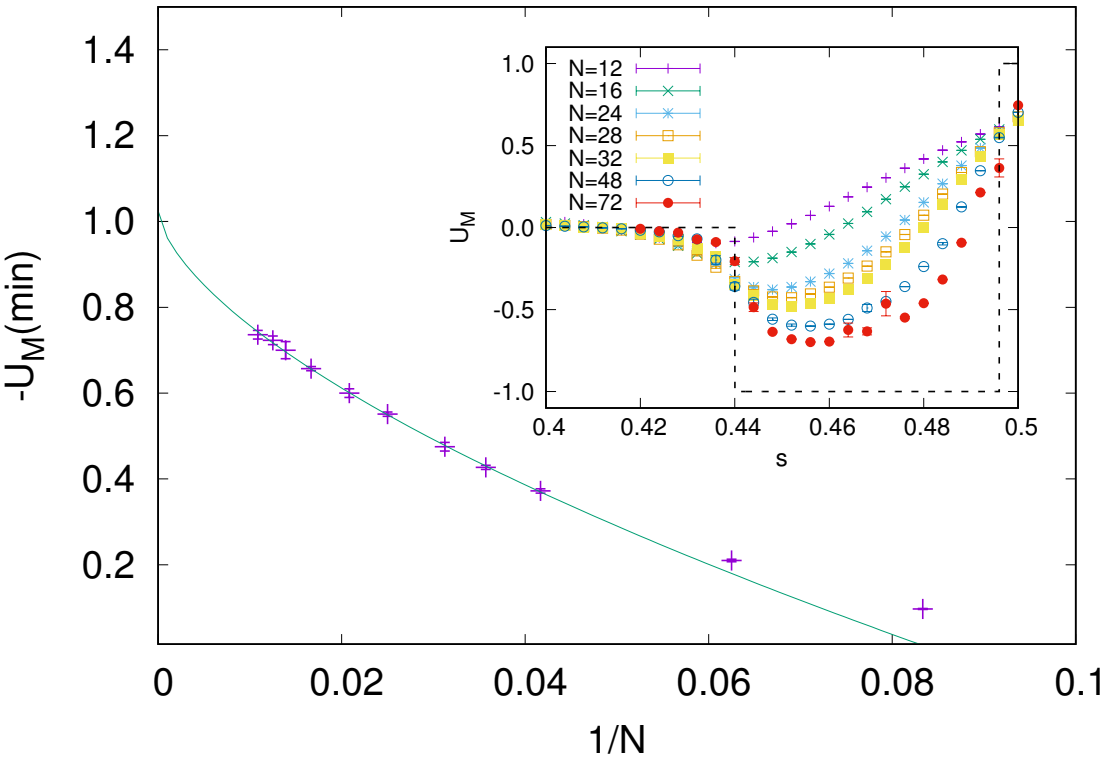

Figure 4·8: The minimum value of U_m at $p = 0.95$ as a function of N fit to the form $a+bL^{-c}$ converges to 1.02(3). Inset: U_M as a function of tuning parameter s for various system sizes. The thermodynamic from of U_M is shown by the dashed line.

Gaussian integrals over the unit vectors chosen from a tetrahedron and which lie in 3D space. In the ordered phase the fluctuations are small compared to the mean and $r = 1$. In the case of a typical continuous transition, r would vary monotonically from 1 to 5/3 from the ordered to paramagnetic phases. This is not the case for the Potts model, as seen from our simulations in Fig. 4·10, and we find a peak which grows for larger sizes. The peak appears to diverge logarithmically in the range which we have studied, but we would expect this value to converge eventually (perhaps at $r = 3$, as shown in the inset of Fig. 4·10) as we are studying a continuous phase transition. This implies remnant effects of a polarization phase which cannot be explicitly realized in this formulation of the Potts model. These effects persist up to the largest lattice

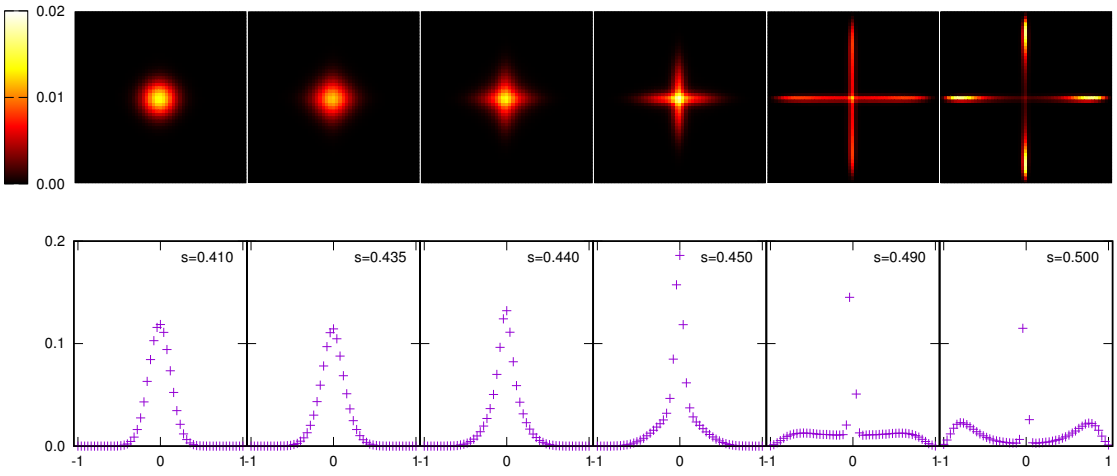

Figure 4·9: Order parameter histogram as a function of the tuning parameter s. Top: The 2D histogram of M_x and M_y. Bottom: Marginal probability distribution of M_x at corresponding values of s.

sizes (3072×3072) we were able to study and may be suppressed at even larger scales, in which case the origin of the new length scale would be of interest.

4.4 Using symmetries to design ergodic updates

In the case of coupled Ising models studied here, a set of symmetries are used while designing updates for the Monte Carlo simulation. These are the Z_2 symmetries associated with each spin species ($\sigma^z \to -\sigma^z$, $\tau^z \to -\tau^z$) and the combined flip $\sigma^z\tau^z \to -\sigma^z\tau^z$. To make use of these in the spacetime configurations which the QMC simulation samples, we introduce identity operators which do not change the physics of the system. These can be represented as I_{σ^x},I_{τ^x} and $I_{\sigma^x\tau^x}$, where the subscript denotes the off-diagonal operator it is exchanged with during simulation. These operators are added into the Hamiltonian with the same weight as their counterparts, this is done to ensure that an update can be done which switches the operator without changing the probability of the configuration. Due to his freedom of switching the off-diagonal operators, the spacetime string breaks up into clusters which can be

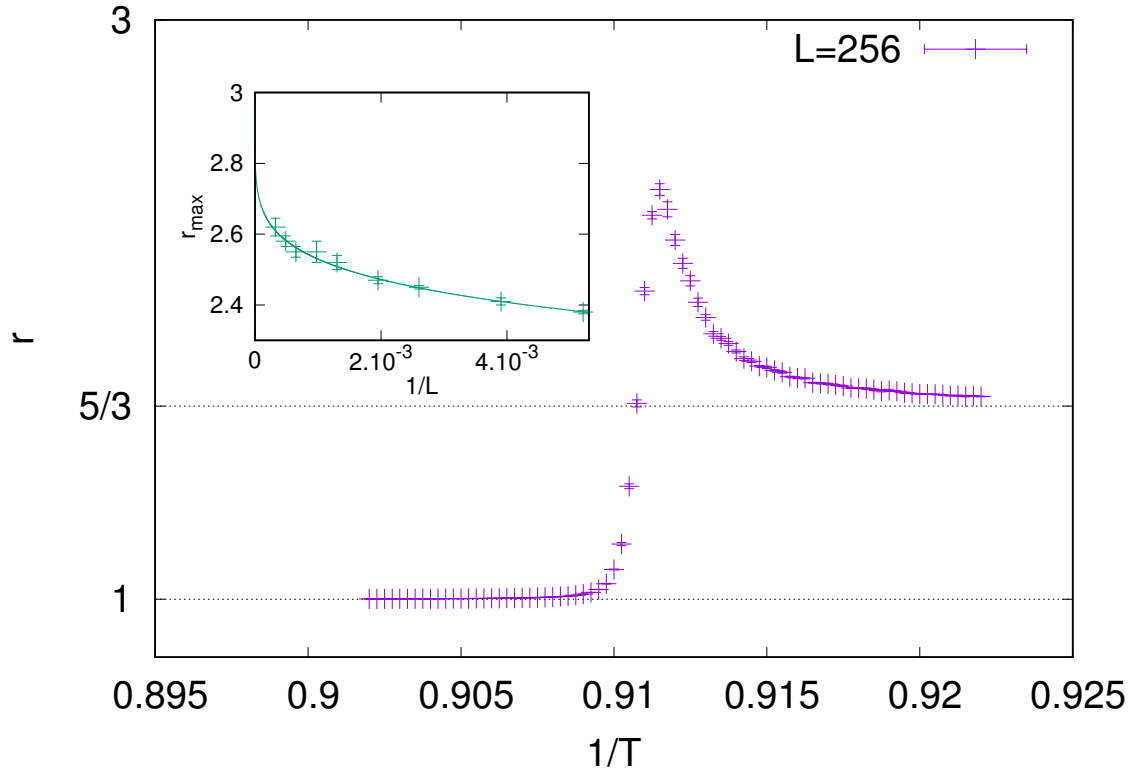

Figure 4·10: Binder ratio for the 2D $q = 4$ Potts model shows a peak at the transition, as shown here for a 256×256 system. Inset: Value of the peak as a function of inverse size fit to a function of the from $f(x) = 3 - ax^b$.

flipped under the symmetries mentioned above. This update also flips the spins in the spacetime region spanned by each cluster.

We can break the update into steps that interact with different types of clusters. We use an update which builds clusters only using the σ degrees of freedom, and flip them with a probability half, leaving the τ spin states intact. An identical update is also performed using only the τ spins, as the system is symmetric in the two species. In addition to these two independent cluster updates, we have a combined one which builds clusters by using ferromagnetic bonds of both species, but the identity and off-diagonal terms corresponding to $\sigma\tau$ only. This cluster allows a combined flip for both species and incorporates the exact Ising symmetry of merging both species into

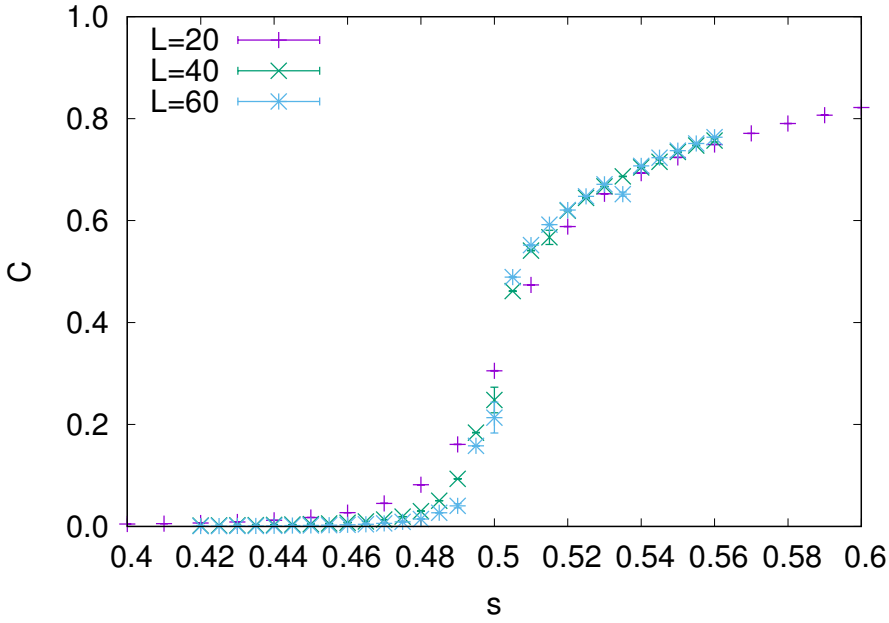

Figure 4·11: Cluster size as a function of s shows the development of large clusters in the ordered phase.

a single spin which is achieved in the $p = 1$ limit. For each of the updates described above, the space time string is broken into distinct clusters, such that the clusters span the entire configuration. As we have considered p close to unity in this chapter, the number of σ^x or τ^x operators is expected to be small compared to the number of $\sigma^x\tau^x$. This implies that the cluster breaking operators for the σ or τ updates is small, leading to larger clusters than the ones generated by the $\sigma\tau$ update. In addition to this, cluster sizes are also controlled by the strength of the ferromagnetic order (s).

For large s, the number of cluster breaks are suppressed due to the large number of ferromagnetic operators and the interconnected clusters which these create. Cluster size can be directly calculated by tracking the number of vertices (or equivalently operators) in a particular cluster. In the extreme paramagnetic limit, this reduces to just two vertices per cluster, due to the complete absence of ferromagnetic operators. In this limit a cluster just consists of two cluster breaking operators, which terminate

both ends. Fig. 4·11 shows the cluster size C as a function of s for sizes L=20,40 and 60, and we can see a sharp increase in size independent of system size, close to the critical value of s. The cluster size is normalized by the maximum size of space time and we see that at the phase transition, the clusters reach a size which is macroscopic similar to the magnetization.

Chapter 5

Obstacles to Adiabatic Quantum Computing

5.1 Quantum adiabatic annealing algorithm: outline and general considerations

The quantum adiabatic annealing (QAA) algorithm was introduced as a method to solve computational problems in Refs. (Farhi et al., 2000; Farhi et al., 2001). It exploits long-range quantum coherence in a time dependent quantum system whose defining Hamiltonian interpolates adiabatically between two limits. The goal is to use QAA to reach the ground state of a complicated classical Hamiltonian H, which encodes the solution of the computational problem at hand, by adiabatically deforming the quantum ground state of a "simpler" initial Hamiltonian, which is easy to prepare.

Concretely, a computational problem on N Boolean variables is mapped to a Hamiltonian H that describes interactions between N classical Ising spin degrees of freedom $\sigma_i^z = |\uparrow\rangle, |\downarrow\rangle$ for $i = 1, \ldots, N$. The spin-up state $\sigma_i^z = |\uparrow\rangle$ can be chosen to represent bit state $x_i = 1$ and the spin-down state $\sigma_i^z = |\downarrow\rangle$ the bit state $x_i = 0$. The mapping is such that the bit assignment that corresponds to the ground-state spin configuration of H encodes the solution of the computational problem. (Here we will mainly concern ourselves with a class of problems that have a single solution, such that the ground state of H is non-degenerate.)

In the QAA algorithm, the classical spins (bits) are represented by quantum spin-1/2 degrees of freedom. The QAA protocol is typically carried out at zero temperature and proceeds by preparing the system in a uniform superposition of all σ_i^z eigenstates by applying a strong transverse field (σ_i^z is a Pauli matrix that defines a local quantization axis for the i-th spin). Annealing is implemented by adiabatically "turning off" the transverse field while "turning on" the Hamiltonian H. This process defines a time-dependent Hamiltonian

$$H_a = (1-s)H - sV\,, \tag{5.1}$$

where $V = \sum_{i=1}^{N} \sigma_i^x$ is the transverse field term and $s = f(t)$ is a time-dependent parameter. The protocol usually starts with $f(0) = 1$ to ensure that the system is in the transverse-field ground state, where each spin is polarized along the x-axis, and ends with $f(T_f) = 0$, which recovers the target Hamiltonian at time T_f. The quantum adiabatic theorem (Wannier, 1965; Kato, 1950) guarantees that the system remains in its instantaneous ground state if $f(t)$ varies "slowly enough" with time. To be more specific, it says that the total duration T_f of the protocol should satisfy

$$T_f \gg \hbar \frac{\max_s |V_{10}(s)|}{(\Delta E_{\min})^2}\,, \tag{5.2}$$

where $V_{m0} = \langle 0|\partial H_a/\partial s|m\rangle$ in the eigenbasis spanned by $|m\rangle$, $m = 1, \ldots, 2^N - 1$, and $\Delta E_{\min}$ is the minimum gap between the ground state and the first excited state encountered during the entire protocol.

Generally, V_{m0} is proportional to system size for a local Hamiltonian and the scaling of T_f is controlled by the scaling of the minimum gap. This implies that if the system passes through a phase transition where the gap vanishes, the time to solution using a quantum annealing protocol can be polynomial or exponential in system size depending on the behavior of the minimum gap with system size. Continuous phase

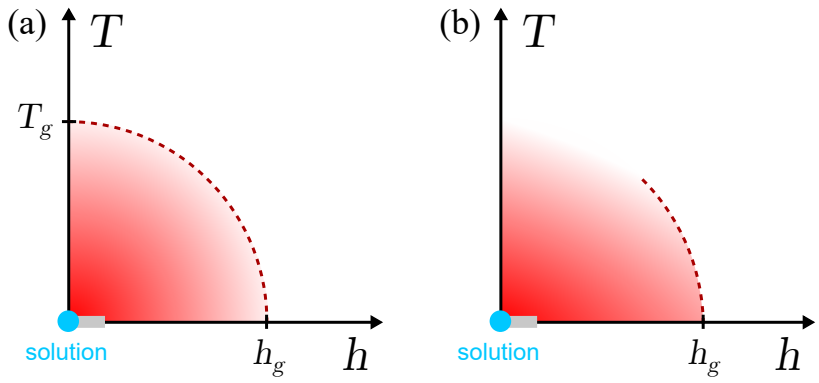

Figure 5·1: Cartoon phase diagrams in the temperature-transverse field parameter space for two scenarios that may occur in the application of the SA and QAA algorithms to the solution of computational problems. In the scenario of panel (a), SA meets a transition to a glassy phase at $T = T_g$, whereas QAA encounters a first-order quantum phase transition at $h = h_g$. Dashed line indicates a putative phase boundary that terminates at the two critical points on the axes. Panel (b) depicts the case where there is no bulk classical thermodynamic phase transition to a glass phase, but the obstruction of a first-order quantum phase transition nevertheless remains.

transitions have a scale-invariant critical point, which implies that the gap must have a polynomial dependence on system size (Sondhi et al., 1997). First-order transitions, on the other hand, manifest themselves in finite-size systems via gaps that vanish exponentially with system size, although there are pathological cases where the gap closing is only polynomial (Laumann et al., 2012). It is therefore highly probable that the QAA algorithm fails to find the solution when the annealing protocol described by H_a leads through a first-order transition in the thermodynamic limit.

In what follows, we will rewrite H_a as

$$H_a = JH - hV\,, \tag{5.3}$$

allowing J and h to take arbitrary positive values, to conform with common notation in the literature.

Since H is classical, one may also consider using simulated annealing (SA) to reach

its ground state. In this protocol, $h = 0$ and one slowly varies the temperature T from $T = \infty$ to $T = 0$. Local thermal dynamics, implemented via, e.g., the Metropolis algorithm, progressively lead toward lower-energy configurations. SA, and in fact any local classical algorithm, fails whenever a first-order transition into a glass phase is encountered upon reducing the temperature. This is true regardless of the hardness of the computational problem encoded by H (Ricci-Tersenghi et al., 2001; Ricci-Tersenghi, 2010).

When SA and QAA are taken on equal footing as methods for the solution of a given problem, they give rise to a phase diagram as a function of T and h, whose origin represents the solution of the problem. Fig. 5·1 shows two distinct scenarios for this phase diagram. In the first scenario, the solution is separated from both the classical high-T paramagnet and the strong-field quantum paramagnet, i.e., the initial states of the SA and QAA protocols, respectively, by first-order transitions. This is a commonly encountered scenario for computational problems, such as satisfiability or coloring, and is illustrated in Fig. 5·1(a). For example, the 3-regular 3-XORSAT problem, as it was formulated and studied in Ref. (Farhi et al., 2012) and also briefly introduced below, belongs to this category.

In this work, we will use a lattice reformulation of computational problems that lacks the classical transition to a glassy phase. This formulation introduces an alternative scenario to the aforementioned one and raises the question of whether the quantum phase transition is absent as well in this case, i.e., whether the two transitions are somehow linked. Below we will provide evidence for a negative answer to this question: our results suggest that the quantum phase transition remains present and first-order, and hence most probably accompanied by exponentially vanishing gaps in progressively larger finite-size systems, even in the absence of a thermodynamic classical transition to a glassy phase.

5.2 k-regular k-XORSAT and lattice embedding

5.2.1 The XORSAT problem

In this section, we describe the mapping of the the k-regular k-XORSAT problem (Johnson and Garey, 1979) to a spin Hamiltonian. We choose XORSAT because it is a prototypical problem in both physics and theoretical computer science. Even though XORSAT can be solved in polynomial time with Gaussian elimination, it nevertheless has evaded efficient solution with any local algorithm, including variants of the Davis-Putnam algorithm (Haanpää et al., 2006), message-passing methods (Jia et al., 2005), stochastic search (Guidetti and Young, 2011), simulated annealing (Ricci-Tersenghi et al., 2001), and quantum adiabatic annealing (Farhi et al., 2012).

Here we focus on the k-regular variant of k-XORSAT. This constraint satisfaction problem is defined on N Boolean variables subject to N clauses, where each clause takes in k bits and each bit participates in k clauses. The solution to the problem is a bit assignment that satisfies all clauses. An XORSAT clause evaluates to 0 (false) or 1 (true) if the sum of the bits in the clause modulo 2 is 0 or 1, respectively. In spin language, this can be interpreted as requiring the product of the spins in a particular clause to be positive or negative and associating an energy cost to the unfavorable outcome. For example, the spin Hamiltonian can be written as

$$H = -\sum_{j=1}^{N} \prod_{i \in c_j} \sigma_i^z \,, \tag{5.4}$$

where c_j is the set of the k indices of the spins that participate in the j-th clause, for k odd. Since clauses are not constrained to connect nearby spins only, this spin Hamiltonian is best represented as a bipartite k-regular graph, where one independent set of vertices represents the spins and the other the clauses. A random instance of

this problem is thus a randomly generated bipartite k-regular graph. A solution of an instance (if it exists) is given by a corresponding ground state of H.

Numerical examination of the QAA algorithm for Hamiltonian (5.4) restricted to $k = 3$ and to instances with unique ground states showed that the minimum gap closes exponentially with system size, indicating a first-order transition at a particular value of the transverse field in the thermodynamic limit (Farhi et al., 2012). This finding implies that QAA takes an exponentially long time to find the solution in this formulation of 3-regular 3-XORSAT. On the other hand, application of the SA algorithm to the XORSAT problem reveals a random first-order transition into a glassy phase at some characteristic temperature — see, e.g., Ref. (Ricci-Tersenghi et al., 2001). These results suggest that the solutions of XORSAT instances reside deep inside a glass phase and are inaccessible to both classical local search algorithms and QAA, despite the fact that XORSAT is computationally tractable (i.e., in complexity class P).

5.2.2 Lattice embedding

In an attempt to avoid the aforementioned obstructions to the solution of XORSAT, here we introduce a lattice embedding of the problem that circumvents the classical thermodynamic transition. The idea is based on previous works by some of us (Chamon et al., 2017; Zhang et al., 2018). Note that this lattice embedding does not enable an efficient solution of the problem via SA, despite the absence of the glass transition, as the dynamics instead becomes glassy upon approaching $T = 0$. The rationale for this reformulation is rather to see whether the avoidance of the thermodynamic glass transition and hence the absence of a finite-T classical glass phase has any effect on the quantum axis.

The lattice embedding is achieved by drawing each variable and each clause as a bit line or "bus" and laying all lines on a 2D plane, with vertical lines corresponding to

clauses and horizontal ones to variables, as shown in Fig. 5·2. Each variable (clause) corresponds to a horizontal (vertical) Ising spin chain and the intersection between variable chains and clause chains is mediated by CNOT or SWAP gates. If the y-th variable participates in the x-th clause, then a CNOT gate is placed at the intersection of the x-th vertical line with the y-th horizontal line, else a SWAP gate is placed to ensure that the bit and clause do not couple.

Each gate has two inputs (i_1 and i_2) and two outputs (o_1 and o_2). The gate constraints can be written in spin language as

$$H^0_{x,y} = -\sigma^z_{x,y;i_1}\sigma^z_{x,y;o_1} - \sigma^z_{x,y;i_2}\sigma^z_{x,y;o_2} \tag{5.5a}$$

for a SWAP gate and

$$H^1_{x,y} = -\sigma^z_{x,y;i_1}\sigma^z_{x,y;o_1} + \sigma^z_{x,y;i_1}\sigma^z_{x,y;i_2}\sigma^z_{x,y;o_2} \tag{5.5b}$$

for a CNOT, where the subscripts x and y specify the position of each gate. To accommodate the y-th variable to appear negated in the x-th clause, we can simply change the sign of the second term in (5.5b). Here we will deal only with monotone instances where no variables appear negated, and hence no such change will be necessary.

Inter-site ferromagnetic bonds of strength J are placed between the outputs of a gate and the inputs of nearest-neighboring gates. This construction ensures that when all ferromagnetic bonds are satisfied by a spin configuration, the corresponding bit assignment satisfies all clauses and is the solution to the problem. The overall

spin Hamiltonian is

$$H = -\sum_{\langle x,y;x',y'\rangle}\sum_{v=1,2}\sigma^z_{x,y;o_v}\sigma^z_{x',y';i_v} + g\sum_{x,y}H^{A_{x,y}}_{x,y} \tag{5.5c}$$

$$-\sum_x(\sigma^z_{x,0;o_2}\sigma^z_{x,\partial_{y=0}} + \sigma^z_{x,N;i_2}\sigma^z_{x,\partial_{y=N}}) \tag{5.5d}$$

$$+ g\sum_x(\sigma^z_{x,\partial_{y=0}} \pm \sigma^z_{x,\partial_{y=N}})\,. \tag{5.5e}$$

The sums are over $x, y = 1, \ldots, N$, so that a problem instance with N variables maps to a lattice with N^2 sites with a gate at each site, $\langle \ldots \rangle$ denotes neighboring positions on the lattice, v is the orientation of the bond labeled as 1 (2) for horizontal (vertical), and g is a constant that offsets the energy cost of the gate and boundary terms with respect to the bond terms.

The first line of Eq. (5.5c) defines the interactions in the bulk. A is the biadjacency matrix of the bipartite k-regular graph that defines the problem instance, as described above. When $A_{x,y} = 1$, a CNOT gate is placed at position (x, y), otherwise a SWAP is placed there instead, as sketched in Fig. 5·2. Note that in our convention indexing proceeds from left to right and top to bottom. We consider the limit $g \to \infty$, so that outputs are essentially "dummy" spins, whose state is completely controlled by the gate inputs. When the ground state of H is reached, the solution appears on the left and right boundaries of the lattice, which are left free. The requirement that clauses sum modulo 2 to 0 or 1 is enforced by the term on the last line, which acts only on the top and bottom rows of boundary spins and whose relative sign between top and bottom depends on whether k is odd or even. For example, for $k = 2$ we choose + (all-zeros state in bottom row) to ensure that all clauses sum modulo 2 to 0, whereas for $k = 3$ we choose − (all-ones state in bottom row), which requires all clauses to sum modulo 2 to 1. When $g \to \infty$ this interaction becomes a hard constraint. This clause constraint is then propagated to the bulk by the terms in

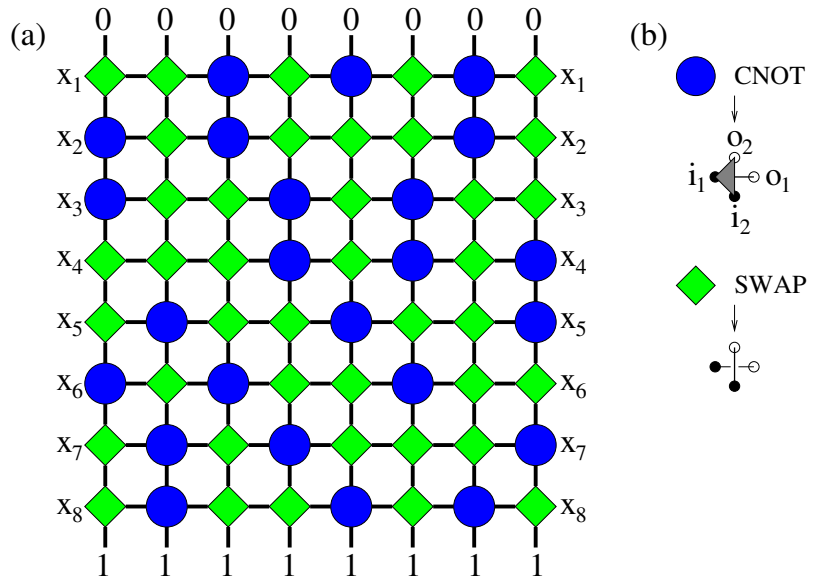

Figure 5·2: (a) Lattice representation of 3-regular 3-XORSAT instance with 8 variables and 8 clauses as a 8×8 lattice of CNOT and SWAP gates. There are 4 bits coupled by a gate at each position of the lattice, as shown in (b). The variable bits x_i record the solution of the problem upon termination of a protocol that reaches the ground state. Upper and lower boundary states are forced by a strong field that favors the uniform bit states shown. (b) Sketch of couplings between bits in each of the gates. Lines denote ferromagnetic bonds in the spin representation and grey triangle represents the 3-spin term in Eq. (5.5b). The formula for the 3-XORSAT instance shown here is $(x_2 \oplus x_3 \oplus x_6) \wedge (x_5 \oplus x_7 \oplus x_8) \wedge (x_1 \oplus x_2 \oplus x_6) \wedge (x_3 \oplus x_4 \oplus x_7) \wedge (x_1 \oplus x_5 \oplus x_8) \wedge (x_3 \oplus x_4 \oplus x_6) \wedge (x_1 \oplus x_2 \oplus x_8) \wedge (x_4 \oplus x_5 \oplus x_7)$.

Eqs. (5.5d) and (5.5e), which define the interaction between spins at the top ($\partial_{y=0}$) and bottom ($\partial_{y=N}$) boundaries and bulk gate spins.

Here we restrict our analysis to instances of k-regular k-XORSAT which have all the minimum nonzero number of solutions. For $k = 3$, generic problems with a unique solution exist. For all such problems, a spin reversal transformation exists which maps the solution to the all spins down state (Farhi et al., 2012) and we shall assume that our system has already undergone this transformation. We will focus on these problems below, as they are a finite fraction of all 3-XORSAT instances and are

thus good representatives of the full ensemble (Jörg et al., 2010). For $k = 2$, there are always two solutions, one of which corresponds to the all-down state.

We generate 3-regular 3-XORSAT instances with unique solutions by first generating a random bipartite 3-regular graph and retaining only those instances which have an odd determinant, as this condition enforces a unique solution (Yang, 2013). We also ensure that the generated graph is connected. We then use the biadjacency matrix of this graph to define the lattice embedding. For the k-regular variants of XORSAT, the finite lattices are by definition square. Varying the clause-to-variable ratio amounts simply to changing the lattice aspect ratio.

5.3 Analytic results: limiting cases and weak-field perturbation theory

5.3.1 Dilute constraint limit and 2-XORSAT

In the lattice setup, if we only have SWAP gates at all the intersections between clauses and bits, then we recreate disconnected transverse field Ising chains. This can be seen by considering the action of the SWAP gate as given in Eq. (5.5a), where we see that spins are only coupled along either the horizontal or vertical directions. Considering also the transverse-field term, and remembering that input and output spins of gates are locked when $g \to \infty$, the Hamiltonian for a decoupled chain reduces to

$$H_a = -J \sum_{i=1}^{N} \sigma_i^z \sigma_{i+1}^z - h \sum_{i=1}^{N} \sigma_i^x \,, \tag{5.6}$$

where i now denotes the coordinate along the chain. This is simply the transverse-field Ising (TFI) chain, which is known to have a continuous phase transition at $h = J$ and a critical behavior which is well understood (Pfeuty, 1970). This would then imply that in the limit of zero CNOT gates on the lattice, we would have a second-order transition characterized by the TFI chain universality class.

The lattices that arise in our embedding of k-regular k-XORSAT have k CNOTs in each vertical and horizontal line. This leads to a CNOT density $\frac{k}{N}$. For $N \gg k$, the system reduces to independent TFI chains coupled at a vanishing number of points. Two possibilities arise for a potential phase transition that the system may undergo as a function of h. The first is that the phase transition remains continuous as for decoupled TFI chains when the density of "impurities" is vanishing. The second possibility is that this vanishing number of impurities drastically changes the nature of the phase transition from continuous to first-order. In the first case, we would be left with a lattice which is able to solve the computational problem in polynomial time. In the second case, the lattice would require exponential time and would be an example of a system where adding a vanishing number of impurities changes the order of the transition. An example of this behavior occurs in the polymerization of rubber (Flory and Rehner Jr, 1943), where the process of vulcanization leads to a vanishing number of cross-links between polymers, which in turn changes the state of rubber from liquid to solid.

Let us examine the $k = 2$ case. Each instance contains a periodic Ising chain, as it corresponds to a series of ferromagnetic bonds between spins, where each spin participates in only two bonds, as illustrated in Fig. 5·3(a). This lattice can be reconfigured as an Ising chain with offshoots, as shown in Fig. 5·3(b), using the following "unraveling" procedure. First, pick an arbitrary CNOT and an arbitrary direction (vertical or horizontal), then draw a link between the starting CNOT and its neighbor in that direction. As there is only one neighbor in either direction, there is no ambiguity in this step. Now rename the neighbor as the starting site and follow the same procedure using the direction perpendicular to the current direction. This process creates a unique loop with spin chains branching out at the locations with CNOTs. This equivalence is valid as SWAP gates only braid chains over each other

without interactions. Taking the limit of large size, we would expect the average separations between CNOTs to be of order N and the fluctuations about this should be statistically small.

Examining the energetics of domain walls in this system illustrates why SA is expected to be efficient in reaching the solution in this case. Let us consider a configuration of this system with a number of domain walls which would correspond to a typical state encountered at finite temperature, as seen in Fig. 5·3(b). If we translate a domain wall through a CNOT, it generates two domain walls on the other side, one of which can be healed by translating it out to the boundary, while the other can travel around the ring until it meets another domain wall, with which it can mutually annihilate. In this way, domain walls can be healed all the way to a state without domain walls, i.e. the ground state, in a smooth sequence of steps that monotonically reduce energy other than the one additional bond that must be broken when passing through a CNOT. In Sec. 5.4, we will show that 2-XORSAT is also efficiently solved with QAA.

We now apply the same argumentation to the lattice representation of the $k = 3$ case. We decompose the lattice into a loop using the unraveling procedure. Fig. 5·4 shows a realization of 3-regular 3-XORSAT with the same backbone structure as Fig. 5·3. The additional CNOT gates now provide frustrating interactions which force the backbone chain to have all spins pointing down and spin inversion symmetry for that section of the lattice is lost. We can look at this in detail using the particular cross-connecting CNOT shown in Fig. 5·4 (highlighted in red) for the classical ground state where all bonds must be satisfied. If we assume that the spins lying in the blue chain are +1, then spin A3 would be forced to -1, implying B1 has to be -1. From this it follows that B2 must be +1, as B3 is +1 due to a direct connection to the boundary. This would then force B4 and as a result C2 to be +1. And as C3 is +1

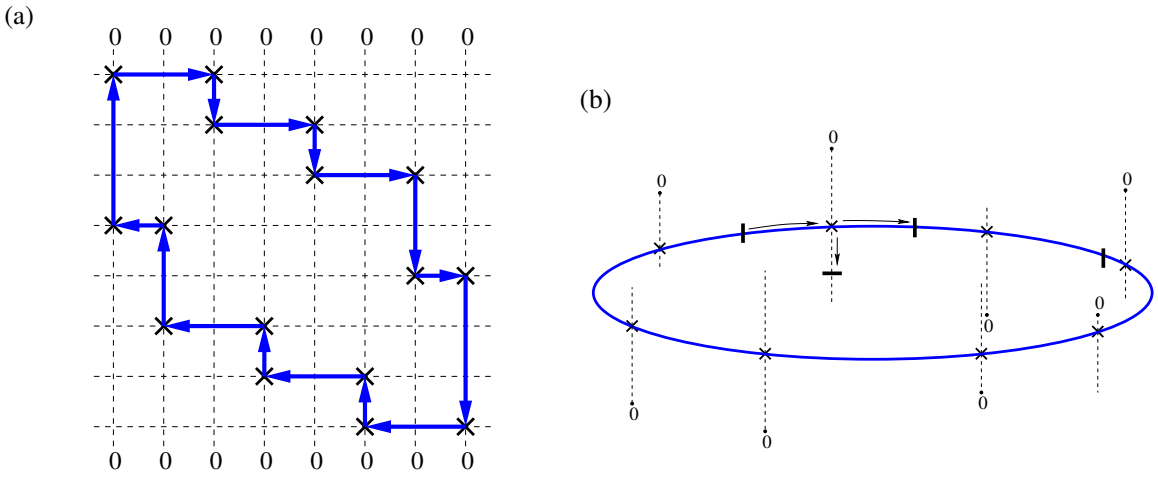

Figure 5·3: (a) "Backbone" loop for a $k = 2$ instance of k-regular k-XORSAT in the lattice representation. SWAP gates are omitted and CNOT gates are denoted by $\times$ symbols. Arrows indicate the "unraveling" procedure described in the text. (b) The corresponding unraveled loop picture with spin chains radiating out of CNOT gates. Domain walls are sketched as | symbols and their movement, indicated by the arrows, heals broken bonds and reduces energy.

due to the boundary, C1 must both be -1 creating a contradiction as C1 belongs in the blue chain and must be +1. In terms of the ring structure in Fig. 5·4(b), this would mean cross-connections between various offshoots, which would destroy the one-dimensional nature of the chain.

The convoluted loop structure of $k = 3$ instances implies that domain wall movement now becomes highly non-trivial: we cannot simply heal domain walls by moving them to the boundary, but must instead translate them to the next CNOT, where they can perhaps annihilate by merging with another domain wall. However, moving a domain wall around the ring now produces a large number of domain walls, as each CNOT results in branching. Each of the resulting defects can be healed only after traversing half the ring on average. This illustrates why SA will fail to solve this problem efficiently, even though our lattice formulation can be shown to feature no

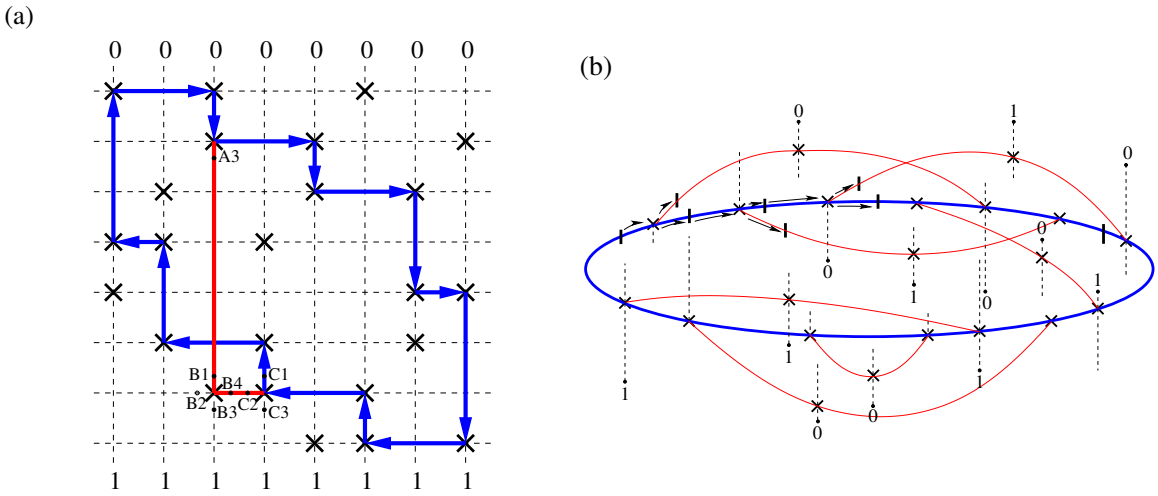

Figure 5·4: (a) Lattice representation of 3-regular 3-XORSAT instance with the same backbone as the one shown in Fig. 5·3(a). The backbone cannot independently fluctuate between positive and negative values, due to constraining couplings to spins outside the backbone (example shown in red), and hence the backbone cannot be isolated as in the $k = 2$ case. (b) Loop equivalent for the $k = 3$ realization, with arrows showing domain wall movement that in this case involves branching of domain walls at CNOT gates.

thermodynamic glass transition (Chamon et al., 2017; Zhang et al., 2018) and is also found to be similar to the vertex models proposed in Ref. (Chamon et al., 2017) (see also Appendix 5.5).

5.3.2 Weak-field perturbation theory: absence of gap collapse

Altshuler *et al.* (Altshuler et al., 2010) pinpointed a potential setback inherent in the QAA protocol. Perturbative analysis showed that generic classical Hamiltonians set up to solve computational problems may give rise to an avoided level crossing when an arbitrarily small transverse field is added. This implies an exponential reduction in annealing velocity, in order to maintain fidelity with the target ground state. In order to fully address the potential issue of avoided level crossings and to show that it is not present in our lattice formulation, we will now present a full perturbative

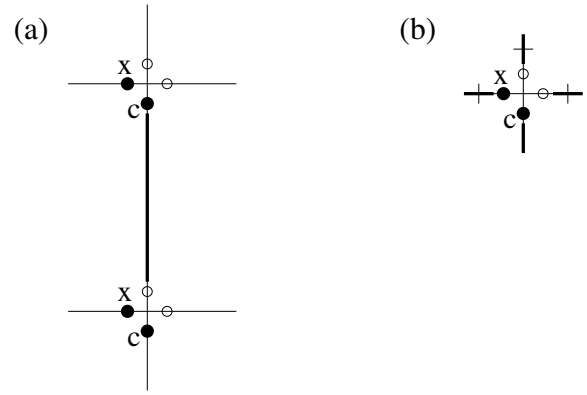

Figure 5·5: (a) Sketch of y-bond connecting the spins of two gates. The state of this bond only affects the four perturbation correction terms corresponding to the spins shown as filled circles. (b) Flipping the control spin (X) of a CNOT gate switches the state of the bonds marked with a cut. Along the vertical line, either the upper or lower bond can be broken (upper bond shown here).

treatment of the general k-regular k-XORSAT problem. A similar analysis appears in Ref. (Knysh and Smelyanskiy, 2010).

Consider the spectrum of a classical spin model that represents a computational problem. We again restrict ourselves to instances with a unique solution. The ground state of the model is therefore unique. The first excited state is degenerate and is made out of all those configurations that differ from the ground state in the status of a single bond. At $h = 0$, the corresponding energy levels have a difference of J from the ground-state level. Altshuler *et al.* show that perturbative corrections to the gap between the ground state and the first excited state for small h should depend on system size in the general case, an argument resulting from the disorder present in most spin representations of computational problems. This leads to a second-order correction proportional to Nh^2, where N is the system size. They conclude that for arbitrarily small h there exists N such that the correction surpasses J, leading to an avoided level crossing.

Contrary to the above argument, we will show that there are no vanishing gaps in

the weak-field limit for k-regular k-XORSAT. First, let us define a bond to have two states, the set state where it is satisfied and the broken state, and the two inputs of a gate to be degrees of freedom (as mentioned in the previous section, the outputs of the gates are completely determined by the inputs, so they are not degrees of freedom, and thus will be ignored). Each gate has four bonds radiating out. Flipping either of the two input spins of a SWAP gate flips the states of two bonds, irrespective of what their states are and irrespective of what the state of the spin was. For the CNOT gate, flipping the carry input (C) switches the state of two bonds, but flipping the control input (X) switches the state of three bonds, again irrespective of the initial bit states (Fig. 5·5). Flipping a boundary spin switches the state of only one bond. The important thing to note here is that the cost induced due to a flip does not depend on the states of spins. Therefore, perturbation theory on the ground state creates N corrections, but none of these depend on the ground-state configuration.

First, consider that all excited-state levels are non-degenerate. This situation is artificial and we treat it only because it simplifies the discussion of the physically relevant case of highly degenerate excitation manifolds discussed below. The excitation energy E_i^{flip} of the state created due to a single spin flip at site i is one of $J, 2J, 3J$, depending on whether it belongs to the boundary, a SWAP gate or a CNOT gate respectively. The second-order perturbation correction to the ground-state energy is

$$\Delta E^{(0)} = \sum_{i=1}^{N} \frac{h^2}{E_i^{\text{flip}}} \propto \frac{Nh^2}{J}\,, \tag{5.7}$$

so far in accordance with the Altshuler *et al.* argument. Any term in this sum is determined only by the state of the four bonds radiating out of a particular point on the lattice and the gate corresponding to that point. Each lattice point carries two spins, implying that the status of a particular bond, which can only control two lattice points, is relevant only to at most four terms in this sum. As the only difference

between the ground state and one of the first excited states is the status of one bond, only four or lesser number of terms in the perturbation corrections for both states can differ. It follows that the change in the gap due to these corrections is

$$|\Delta E^{(0)} - \Delta E^{(1)}| \propto h^2/J\,, \tag{5.8}$$

which is *independent* of system size, similar to the clean TFI model (Suzuki et al., 2012).

We now take into account the mixing of the degenerate first-excited states amongst themselves due to the transverse field. This typically results in the degenerate levels spreading over a band of width $\propto h$ and is, once again, independent of system size. After first-order degenerate perturbation theory, the states that result from the mixing of the first-excited configurations at zero field are

$$|\tilde{E}^{(l)}\rangle = \sum_i \alpha_i^{(l)}\, |E_i^{(1)}\rangle\ , \tag{5.9}$$

where $|E_i^{(1)}\rangle$ is a first-excited configuration with energy $E^{(1)}$. The states $|\tilde{E}^{(l)}\rangle$ are then used to perform higher-order perturbation theory. Second-order corrections look like

$$\Delta\tilde{E}^{(l)} = h^2 \sum_{i,j} \sum_m \frac{\alpha_i^{(l)}\alpha_j^{(l)}}{|E^{(1)} - E_m|}\, \langle E_i^{(1)}|V|m\rangle\, \langle m|V|E_j^{(1)}\rangle\ , \tag{5.10}$$

where m runs over states that are necessarily not $|E_i^{(1)}\rangle$. Of the "diagonal" terms $|\,\langle E_i^{(1)}|V|m\rangle\,|^2$, at most four are nonzero, by the same reasoning we employed above. For the terms with $i \neq j$, if $|E_i^{(1)}\rangle$ has a frustrated bond in the bulk, there is no way to connect it to $|E_j^{(1)}\rangle$ via V using states $|m\rangle$ within the first level. On the other hand, when $|E_i^{(1)}\rangle$ contains a frustrated boundary bond, we can connect to all other such singly excited states. However, these second-order processes are equally possible for all states, regardless of gate configuration, and hence this correction amounts to

a uniform shift of all levels. The above means that the relative shift of a first-excited state level with respect to the ground-state level is going to be bounded in the same way as it was for just one spin configuration in the first level. The same argumentation extends to higher corrections straightforwardly. We therefore conclude that there is no perturbative gap collapse in the weak-field limit for the models we study here.

We remark that the arguments presented above also extend to the random graph spin model for 3-regular 3-XORSAT studied in Ref. (Farhi et al., 2012), and evidence for this can be seen in the duality of $h \leftrightarrow J$ that that model possesses. This duality implies that the spectrum is identical for $h \leftrightarrow J$, and as the strong transverse field limit has a well defined gap, the ferromagnetic limit does too.

5.4 Numerical results

In this Section, we apply the QAA protocol to the lattice models for k-regular k-XORSAT we introduced above. We simulate QAA via projector Quantum Monte Carlo (QMC) simulations to investigate the transitions encountered upon varying the transverse field. Our calculations are set up following the style of simulations for TFI models (Sandvik, 2003; Liu et al., 2013) due to the similarity in the Hamiltonians and they are able to access ground state expectation values for various observables. It is known that for glassy systems or at first-order transitions, this style of QMC suffers from long equilibration times and non-ergodic behavior (Brady and van Dam, 2016). Cluster updates using larger objects made out of multiple spins, which have been found to be useful for particular frustrated Ising antiferromagnets (Biswas and Damle, 2018), were found to be rejection-prone for our 3-XORSAT model due to the three-body terms that make up CNOTs. This limits the sizes of the lattices we can simulate and also how deep our simulations can reach into the ferromagnetic phase. We use a variety of local and replica exchange updates (Hukushima and Nemoto,

1996; Takahashi and Hukushima, 2019) to speed up the algorithm. Details of the implementation of the replica exchange method can be found in Ref. (Takahashi and Hukushima, 2019), where it has been applied to a similar model. We will study our models in the context of continuous and first-order phase transitions, which show a diverging and a finite correlation length, respectively. The energy gap is expected to close for both types of transitions, but the scaling of the minimum gap with system size differs, closing as $\sim N^{-\gamma}$ for the former and $\sim e^{-N^{\gamma}}$ for the latter ($\gamma > 0$).

The lattice models of k-regular k-XORSAT with a transverse field, defined by Eqs. (5.3) and (5.5), show two phases: a disordered phase in the limit of strong transverse field and an ordered phase in the ferromagnetic (or classical) limit. To simplify our analysis, we set $h = 1$ and vary J through the transition between the two phases. To find the critical value of the ferromagnetic coupling J_c and the nature of the phase transition, we use the Binder cumulant (Binder, 1981)

$$U_m = \frac{3}{2}\left(1 - \frac{1}{3}\frac{\langle M_z^4 \rangle}{\langle M_z^2 \rangle^2}\right), \tag{5.11}$$

where M_z is the magnetization of the system in the z direction. In the strong transverse field limit, the system is magnetized along the x axis, which implies that $M_z = 0$, whereas in the ferromagnetic limit all spins are aligned, leading to a saturation of magnetization. U_m is defined such that it evaluates to zero in the disordered phase and unity in the ordered one. At the phase transition, U_m goes from 0 to 1 within a window of J that gets narrower as system size increases. For a continuous transition, the behavior is monotonically increasing in most cases, although exceptions are known (Jin et al., 2012), and for a first-order transition U_m has a negative peak at the critical point which diverges with system size as L^d, where d is the dimensionality of the system (Binder, 1987).

The Binder cumulant is chosen here to be sensitive to Z_2 symmetry breaking,

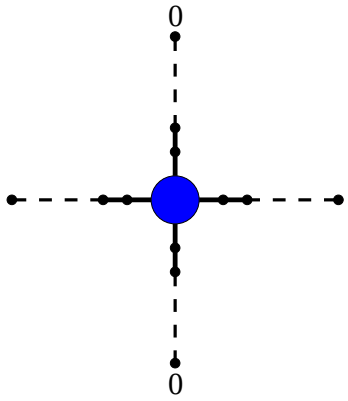

Figure 5·6: Illustration of two TFI chains coupled at their center by a CNOT gate. The boundary spins of the vertical chain are fixed.

which would be the symmetry usually studied in Ising systems. For the $k = 3$ case, the boundary conditions enforce a single solution, meaning that the system is not doubly degenerate and in this case, U_m shows a non-zero value on the disordered side before the transition (seen in Fig. 5·9), as the histogram favors net negative magnetization. This anomaly is also seen in the transverse field Ising chain with fixed boundary conditions similar to the ones studied.

We begin our study of the effectiveness of QAA on 2-regular 2-XORSAT by first applying the algorithm to the building block of this system: a single CNOT gate coupling long spin chains, as shown in Fig. 5·6. The CNOT coupling is expected to result in no drastic change to the continuous phase transition of the two chains, as it is a single defect in a large system. Numerical evidence for this is shown in Fig. 5·7. Even for large systems of two chains intersecting, the magnetization histogram shows no coexistence of phases, indicative of a second-order transition. For first-order transitions, on the other hand, the same histogram would show a bimodal distribution, indicative of phase coexistence (Binder, 1987). We expect the same conclusion to extend to the case of a large number of these "cross"-linked chains connected horizontally when the separation between CNOT gates is large, which is the case for $k = 2$, as shown in Fig. 5·3. It is seen that CNOTs interact only along a linear chain and correlation

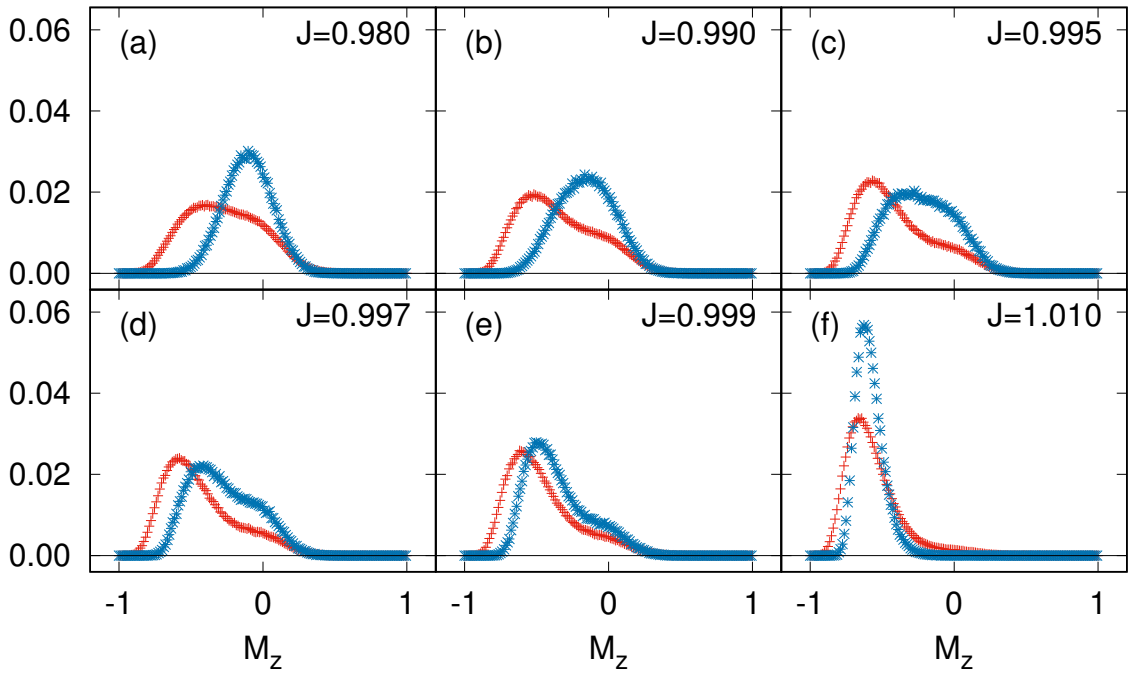

Figure 5·7: Magnetization histograms for the transverse field system shown in Fig. 5·6 with 81 spins per chain (crosses) and 321 spins per chain (stars), as obtained from QMC calculations at $h = 1$. As J increases (a-f), the average magnetization switches values without developing a strong double peak structure even for large size.

length growth is controlled by the physics of the TFI chains connecting them. We therefore expect a continuous phase transition at $h \sim J$.

We analyze 2-XORSAT instances by studying the behavior of U_m and the evolution of the magnetization histograms – see Fig. 5·8. 20 realizations are used for each size and the critical value of J is found to be close to unity, which matches the decoupled TFI chain value. For $k = 2$, the two ground states correspond to the configuration with all spins pointing down and the configuration with all bit line spins pointing up and a complicated ordering of the clause spins which is consistent with the solution and realization dependent. Due to the non-trivial structure of the ground states, U_m

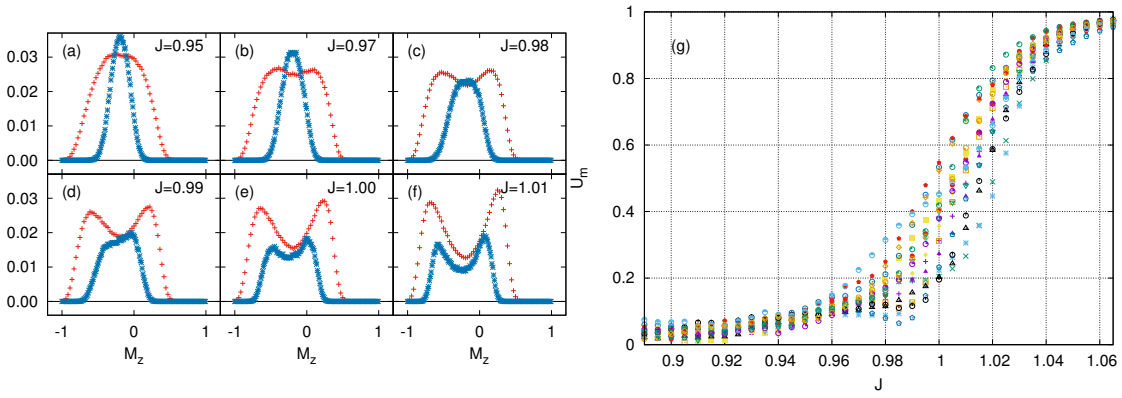

Figure 5·8: (a-f) Magnetization histograms for a single realization of the 2-XORSAT lattice with size 6×6 (crosses) and another with size 16×16 (stars) for increasing J. The slight asymmetry in the two peaks of the histograms may be caused by non-ergodicity issues in the QMC simulation. (g) Binder cumulant for 20 realizations of size 16×16. In all panels $h = 1$.

has to be defined using only the variable spins, as they form a spin-symmetric subset. This implies that the order parameter we use for U_m is the average z-magnetization squared of only the row spins i_1 and o_1 at each (x, y) position, which make up half of the total spins. For all the realizations of all lattice sizes, we found that U_m never becomes negative and the magnetization histograms show no sign of phase coexistence, indicating a continuous transition, as seen in Fig. 5·8.

The QAA protocol for 3-regular 3-XORSAT proceeds in the same vein as for $k = 2$. Using QMC simulations, we study the Binder cumulant using the full magnetization (as $k = 3$ has only one ground state) as a function of ferromagnetic coupling J for lattice sizes ranging from 6×6 to 16×16. For each lattice size, we study 20 realizations of the 3-regular 3-XORSAT on the lattice with unique solutions. We find that for most of the realizations and for all sizes the Binder cumulant shows a negative peak. This can be seen in Fig. 5·9(g) for all realizations of a 16×16 lattice. Due to lack of ergodicity typically seen at first order phase transitions, we had to reject a large number of QMC simulations, retaining only those where both phases

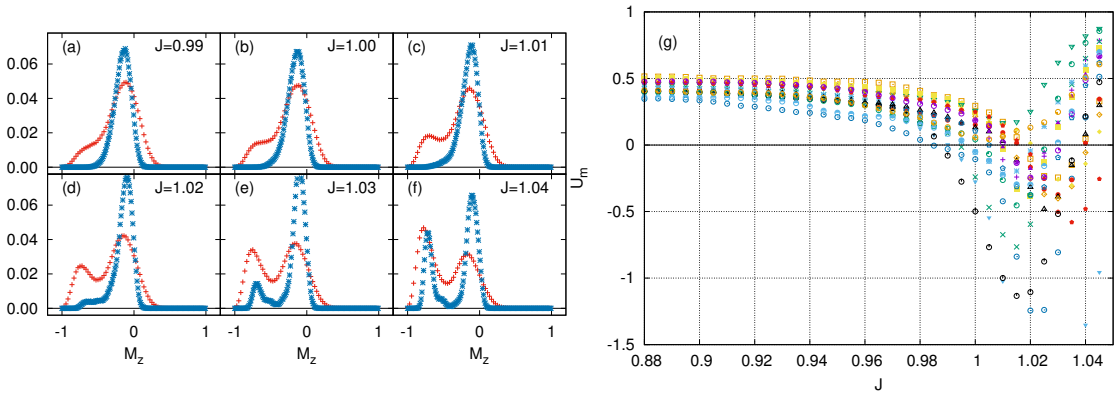

Figure 5·9: (a-f) Magnetization histograms for a single realization of the 3-regular 3-XORSAT lattice with size 6×6 (crosses) and another with size 16×16 (stars) for increasing J. (g) Binder cumulant for 20 realizations of size 16×16. In all panels $h = 1$.

are represented as some simulations are not able to break out of the paramagnetic phase. This in itself only indicates that we may have a first-order transition but does not say so definitively. Showing that the negative peak in the Binder cumulant scales as number of sites is taken to be definite proof that the system is undergoing a first-order transition but we are unable to perform this analysis due to insufficient data quality and range of sizes. We omit error bars in Figs. 5·8(g) and 5·9(g) for clarity and as the error bars are small compared to the spread of the Binder cumulant values for different realizations.

Fig. 5·9 shows the evolution of the histogram as a function of J for the 3-regular 3-XORSAT including the value of J at which U_m is found to be minimum. The histogram indicates that there is a coexistence of phases which sharpens with increasing size and the phase transition can potentially develop into a first-order transition in the thermodynamic limit. Our system sizes and data quality limit our analysis, but for the system sizes we can access the first order nature appears to persist to the largest system size (Fig. 5·9). It is important to stress here that although the density of gates is vanishing in the thermodynamic limit, they are placed in a correlated

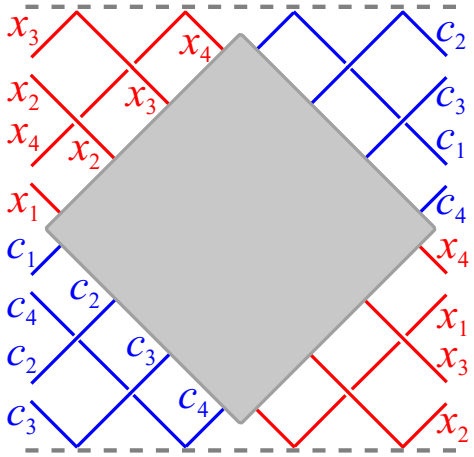

Figure 5·10: Illustration of the mapping of the lattice formulation of k-XORSAT onto the general vertex model framework for computational problems introduced in (Chamon et al., 2017), here shown for a 4×4 lattice. The grey shaded area is the placeholder in which a lattice like the one shown in Fig. 5·2(a) plugs into after a $\pi/4$ rotation. In this embedding, clause bits (blue) are fixed and variable bits (red) are left free at both left and right boundaries, whereas all bit lines are "reflected" at the top and bottom boundaries (dashed lines).

manner, and can hence define the criticality of this model.

5.5 Mapping to the vertex model

Here we comment on the limitation of using thermal annealing to reach the ground state of 3-regular 3-XORSAT in spite of the absence of a bulk thermodynamic phase transition (Chamon et al., 2017). The simplest way to understand the slow thermal relaxation into the ground state of the XORSAT model is to use the recipe of Ref. (Chamon et al., 2017) to embed XORSAT into the alternative spin model shown in Fig. 5·10. In this model, only half the boundary spins are fixed in each boundary, corresponding to the clause spins being fixed by a strong field in Eq. (5.5e), with the free bits (spins) on the rest of the boundaries. Reaching the ground state of this model through thermal annealing requires that information propagates between the boundaries until all free spins on both boundaries are fixed. This "mixed

boundary condition" case in which only partial initial information is available on the input/output boundaries was already studied in Ref. (Chamon et al., 2017). There it was found that thermal annealing is ineffective in reconciling the non-local information between the two boundaries, explaining the slow relaxation of the lattice embedding of 3-regular 3-XORSAT.

Chapter 6

Conclusions

In this thesis, we have presented a method of QMC simulations for spin systems and discussed implementations in specific models. Using these simulations we have investigated the features of quantum phase transitions.

We began with an investigation of 1+1D quantum phase transitions in the context of quantum field theory and emergent symmetry. We reformulated the results of conformal field theory (CFT) in terms of operators on the lattice which are accessible through our simulations. Using this, we showed how one may investigate the presence of a CFT and emergent symmetry through QMC simulations.

We follow this with an extension to emergent symmetry in 2+1D, where we show valuable numerical evidence for a quantum clock model. Here we have presented a clock model on a square lattice which shows a thermodynamic phase transition with a U(1) emergent symmetry in the presence of simple quantum fluctuations. The U(1) symmetry breaking to Z_q order is controlled by a dangerously irrelevant operator which leads to a second diverging length scale at the critical point. However, merely the presence of two length scales does not recreate anomalous scaling exponents at the critical point as seen at the deconfined critical point. Further investigation around the U(1) symmetric unstable fixed point is required to extract the scaling behavior in the intermediate region of the RG diagram. To create a stronger similarity with deconfined criticality, we can add terms in the Hamiltonian which force an order to order transition. In future work, we plan to investigate a Heisenberg type kinetic

term of the form $T_i^+ T_j^-$, where i and j are nearest neighbors and $T_i^\pm |\theta_i\rangle = |\theta_i \pm 1\rangle$, which may force an order similar to the Valence Bond Solid seen in the so-called JQ model at the deconfined quantum critical point. The $q = 4$ case is found to show an interesting tunability from a first order to a continuous transition. This model can be considered more carefully from the perspective of two coupled Ising models with different strengths of coupling and will be discussed in future work. The quantum clock model and the phenomena observed at its critical point may find applications in quantum phase transitions seen in Josephson Junction arrays as these arrays are described by the XY model and strong quantum effects are not well understood around the superconductor to insulator transition.

Investigations of the quantum clock model led to a natural extension of coupled transverse field Ising models, where we found the intriguing dynamical features arising from fragmented Hilbert spaces. The coupled Ising model discussed here is a tractable system which can source interesting dynamical behavior with excitations showing a restricted extent in space. Due to the intricate structure of non-interacting blocks which this system breaks into, curious features may be manifest in the crossover between quantum and thermal phase transitions, and we intend to study this in future work. Upon the addition of perturbations it is expected that the system regains ergodicity in a manner which depends on the particular perturbation used. There has been a recent numerical study (Zhao et al., 2019) which suggests that long time scales persist even in the case of a 1D version of our model in the limit of weak global transverse fields creating a coupling across blocks. In the presence of the same term, we have verified here that the system encodes a quantum realization of the AT model in a Hamiltonian made out of only two body terms explicitly for 1D and expect the same in higher dimensions. We have also identified a reason for pseudo-first order behavior which is seen in the $q = 4$ Potts model in 2D which corresponds

to a tricritical point with $q \leq 4$ corresponding to continuous transitions and $q > 4$ being first order transitions. This could help explain the microscopic origin of the weak first order transitions in the 1D quantum or 2D classical Potts model, which has been studied from the perspective of complex conformal field theories (Gorbenko et al., 2018). By switching off the matrix element of the transverse field in the Potts model which connects odd and even colors, all even color Potts models can be driven to exactly the limit described here. The classical Potts model has also been independently studied in terms of restricted partitions (Wu et al., 1996). Spin liquids with restricted dynamics have already been found to have similar features (Sikora et al., 2011), and we plan to develop a better understanding for this in analogy with our model in future work.

Transverse field Ising models also play a key role in adiabatic quantum computing (AQC), and we have also applied the QMC method to investigate the features of a simple system to test its viability for AQC. We introduced a statistical mechanics representation of the XORSAT problem that recasts each instance as a planar grid of reversible gates acting on bits that represent the Boolean variables of the problem. The reason we chose this particular embedding of XORSAT is that it lacks a classical thermodynamic phase transition. We studied this system with quantum annealing and showed that it does not suffer from the perturbation theory collapse found by Altshuler *et al.* (Altshuler et al., 2010) at small transverse field strengths. We found that 3-regular 3-XORSAT displays a first-order transition at intermediate values of the transverse field, implying that quantum annealing leads to a time-to-solution that scales exponentially with the size of the system. Our results also suggest that the physics of the phase transition is determined not only by the density of CNOT defects, but also by their correlations. Taken together, these results on this alternative embedding of XORSAT reinforce the conclusion that both thermal and quantum

annealing, which are intrinsically local approaches, can be inefficient in solving even simple problems (in computational complexity class P).

Appendix A

Other Numerical Methods

A.1 Exact Diagonalization

One of the most reliable techniques to study the physics of quantum systems made up of a small number of interacting bodies is exact diagonalization (ED), where the Hamiltonian is represented in a basis of choice, numerically diagonalized and all the features of interest calculated from the eigenvectors and eigenvalues. This method is often used when details of the entire eigenspectrum are desired, e.g. when studying the time evolution of quantum systems. In this thesis, exact diagonalization has mostly been used only to benchmark QMC simulations, by comparing the results from both methods to ensure accuracy of the QMC method. Once this benchmarking is done, the QMC simulations can be used to study larger system sizes.

Here we describe the ED method for a simple transverse field Ising model on a periodic chain, which is given by the following Hamiltonian:

$$H = -J \sum_i \sigma_i^z \sigma_{i+1}^z - h \sum_i \sigma_i^x. \tag{A.1}$$

We first choose a basis where each σ_i^z is diagonal and the spin on a particular site can take two values, labeled as 0 and 1. A particular product state can be written as a sequence of 0's and 1's. For an N-site system, this can be compressed to an integer whose bit-representation is the particular sequence. The space of all product states now spans an orthonormal vector space with 2^N dimensions. The Hamiltonian

can be written as a matrix in this space. The first operator in the Hamiltonian only contributes to the diagonal terms in the Hamiltonian, and can be evaluated by just counting the number of neighbors which have the same spin state, e.g. the state with all 0's has a matrix element of $-JN$. Off-diagonal matrix elements can have a non-zero value of $-h$ only when a single site has a differing spin value for the two states making up the matrix element. This is a consequence of the σ_i^x operator, which acts on a single site and flips its spin state. All other matrix elements vanish for this Hamiltonian. To get the features of this system, we can now numerically diagonalize this matrix using standard libraries such as LAPACK.

A.2 Parallel Tempering

One of the major road blocks which Monte Carlo simulations can suffer from is lack of ergodicity. This implies that one must wait a long time before the results of a Monte Carlo simulation can be trusted. In many cases the efficiency (or degree of ergodicity) can depend on the parameters used in the simulation. Certain regions in parameter space may be easier to sample than others. If the area of interest happens to fall in one of the hard regions, one can allow the simulation to move temporarily into an easy region so that the ergodicity allows for fast mixing. One of the ways of doing this, which we have used in this thesis, is called parallel tempering. This is usually done in the context of classical systems in the presence of temperature. This can be illustrated in a simple manner using the classical Ising model on a square lattice. A simple updating scheme for the Ising model is the Metropolis single spin flip. This works well in the paramagnetic phase, i.e. high temperature, but has poor ergodicity close to criticality and in the ordered phase. One can implement parallel tempering in this system by running simultaneous simulations at different temperatures and allowing simulations to exchange configurations between themselves. This allows a

simulation which is sampling configurations that are closely related to jump to a set of configurations which are different but have a similar weight in the probability distribution function. As the probability of a particular configuration changes with temperature, one must be careful about the acceptance probabilities when exchanging configurations between a pair of simulation threads. For the simple case of two threads, let us call them A and B, exchanging configurations C_A and C_B, the detailed balance condition implies

$$\frac{P_A(C_A \to C_B)}{P_A(C_B \to C_A)} = \frac{P_A(C_B)}{P_A(C_A)}, \tag{A.2}$$

and similarly for P_B. Taking a quotient of the forms of the above equations for P_A and P_B, we get

$$\frac{P_A(C_A \to C_B)P_B(C_B \to C_A)}{P_A(C_B \to C_A)P_B(C_A \to C_B)} = \frac{P_A(C_B)P_B(C_A)}{P_A(C_A)P_B(C_B)}. \tag{A.3}$$

Now, one can use the usual Metropolis method where the smaller of the conditional probabilities is set to one. In this way, the probability of swapping the configurations is found and this method maintains detailed balance across simulation threads. A simple way to test if parallel tempering is leading to an efficient mixing of configurations, is to track the movement of a particular thread as it is exchanged across simulations. If the thread moves across all simulations in the parameter range, one can be sure that the exchange rates are sufficiently high. The success of parallel tempering depends strongly on the density of threads in a particular parameter range, e.g. if the parameter values for different simulations are separated by a large gap, the exchange rate reduces. The required gaps vary with the rate of change of free energy with the parameters and as such, one must use a high density of threads close to critical points.

References

Affleck, I. (1985). *Physical Review Letters*, 55:1355.

Affleck, I. and Haldane, F. D. M. (1987). *Physical Review B*, 36:5291.

Altshuler, B., Krovi, H., and Roland, J. (2010). Anderson localization makes adiabatic quantum optimization fail. *Proceedings of National Academy of Science USA*, 107(28):12446–12450.

Andrews, G. E. (1994). *Number theory*. Courier Corporation.

Arita, C. and Motegi, K. (2011). Spin-spin correlation functions of the q-valence-bond-solid state of an integer spin model. *Journal of Mathematical Physics*, 52(6):063303.

Beach, K. S. D. (2009). *Physical Review B*, 79(22):224431.

Beach, K. S. D. and Sandvik, A. W. (2006). *Nuclear Physics B*, 750(3):142–178.

Belavin, A. A., Polyakov, A. M., and Zamolodchikov, A. B. (1984). *Nuclear Physics B*, 241:333–380.

Binder, K. (1981). Finite size scaling analysis of ising model block distribution functions. *Zeitschrift fr Physik B Condensed Matter*, 43(2):119–140.

Binder, K. (1987). Theory of first-order phase transitions. *Reports on Progress in Physics*, 50(7):783.

Biswas, S. and Damle, K. (2018). Singular ferromagnetic susceptibility of the transverse-field ising antiferromagnet on the triangular lattice. *Physical Review B*, 97(8):085114.

Boyanovsky, D. (1989). *Physical Review B*, 39:6744.

Brady, L. T. and van Dam, W. (2016). Quantum monte carlo simulations of tunneling in quantum adiabatic optimization. *Physical Review A*, 93(3):032304.

Calabrese, P. and Cardy, J. (2004). Entanglement entropy and quantum field theory. *Journal of Statistical Mechanics: Theory and Experiment*, 2004(06):P06002.

Campostrini, M., Hasenbusch, M., Pelissetto, A., Rossi, P., and Vicari, E. (2001). Critical behavior of the three-dimensional xy universality class. *Physical Review B*, 63(21):214503.

Cardy, J. L. (1987). Continuously varying exponents and the value of the central charge. *Journal of Physics A: Mathematical and General*, 20(13):L891.

Chamon, C., Mucciolo, E. R., Ruckenstein, A. E., and Yang, Z.-C. (2017). Quantum vertex model for reversible classical computing. *Nature Communications*, 8:15303.

Chandran, A. and Laumann, C. (2015). Semiclassical limit for the many-body localization transition. *Physical Review B*, 92(2):024301.

Chepiga, N. and Mila, F. (2017). Excitation spectrum and density matrix renormalization group iterations. *Physical Review B*, 96(5):054425.

Delfino, G. and Grinza, P. (2004). Universal ratios along a line of critical points. the ashkin–teller model. *Nuclear Physics B*, 682(3):521–550.

Delfino, G., Picco, M., Santachiara, R., and Viti, J. (2013). Spin clusters and conformal field theory. *Journal of Statistical Mechanics: Theory and Experiment*, 2013(11):P11011.

Di Francesco, P., Mathieu, P., and Sénéchal, D. (1997). Conformal field theory. *Springer Science & Business Media*.

Eggert, S. (1996). *Physical Review B*, 54(14):R9612.

Farhi, E., Goldstone, J., Gutmann, S., Lapan, J., Lundgren, A., and Preda, D. (2001). A Quantum Adiabatic Evolution Algorithm Applied to Random Instances of an NP-Complete Problem. *Science*, 292(5516):472–475.

Farhi, E., Goldstone, J., Gutmann, S., and Sipser, M. (2000). Quantum computation by adiabatic evolution. *arXiv:quant-ph/0001106*.

Farhi, E., Gosset, D., Hen, I., Sandvik, A. W., Shor, P., Young, A. P., and Zamponi, F. (2012). Performance of the quantum adiabatic algorithm on random instances of two optimization problems on regular hypergraphs. *Physical Review A*, 86(5):052334.

Fáth, G. (2003). Luttinger liquid behavior in spin chains with a magnetic field. *Physical Review B*, 68(13):134445.

Flory, P. J. and Rehner Jr, J. (1943). Statistical mechanics of cross-linked polymer networks i. rubberlike elasticity. *Journal of Chemical Physics*, 11(11):512–520.

Gorbenko, V., Rychkov, S., and Zan, B. (2018). Walking, weak first-order transitions, and complex cfts ii. two-dimensional potts model at $q > 4$. *arXiv preprint arXiv:1808.04380*.

Guidetti, M. and Young, A. P. (2011). Complexity of several constraint-satisfaction problems using the heuristic classical algorithm walksat. *Physical Review E*, 84(1):011102.

Haanpää, H., Järvisalo, M., Kaski, P., and Niemelä, I. (2006). Hard Satisfiable Clause Sets for Benchmarking Equivalence Reasoning Techniques. *Journal on Satisfiability, Boolean Modeling and Computation*, 2:27–46.

Haldane, F. (1980). General relation of correlation exponents and spectral properties of one-dimensional fermi systems: Application to the anisotropic s= 1 2 heisenberg chain. *Physical Review Letters*, 45(16):1358.

Haldane, F. D. M., Ha, Z. N. C., Talstra, J., Bernard, D., and Pasquier, V. (1992). *Physical Review Letters*, 69:2021–2025.

Hardy, G. (1999). Ramanjuan: Twelve lectures on subjects suggested by his life and work. 1940. *Providence, RI: AMS Chelsea Pub.*

Hastings, M. B., González, I., Kallin, A. B., and Melko, R. G. (2010). *Physical Review Letters*, 104:157201.

Heuer, H.-O. (1993). Critical crossover phenomena in disordered ising systems. *Journal of Physics A: Mathematical and General*, 26(6):L333.

Hukushima, K. and Nemoto, K. (1996). Exchange monte carlo method and application to spin glass simulations. *Journal of Physical Society of Japan*, 65(6):1604–1608.

Janke, W. and Villanova, R. (1997). Three-dimensional 3-state potts model revisited with new techniques. *Nuclear Physics B*, 489(3):679–696.

Jia, H., Moore, C., and Selman, B. (2005). From Spin Glasses to Hard Satisfiable Formulas. In *Theory and Applications of Satisfiability Testing, 7th International Conference, SAT 2004*, pages 199–210.

Jin, S., Sen, A., and Sandvik, A. W. (2012). Ashkin-teller criticality and pseudo-first-order behavior in a frustrated ising model on the square lattice. *Physical Review Letters*, 108(4):045702.

Johnson, D. S. and Garey, M. R. (1979). Computers and intractability: A guide to the theory of np-completeness. 1.

Jörg, T., Krzakala, F., Semerjian, G., and Zamponi, F. (2010). First-Order Transitions and the Performance of Quantum Algorithms in Random Optimization Problems. *Physical Review Letters*, 104(20):207206.

José, J. V., Kadanoff, L. P., Kirkpatrick, S., and Nelson, D. R. (1977). Renormalization, vortices, and symmetry-breaking perturbations in the two-dimensional planar model. *Physical Review B*, 16(3):1217.

Kato, T. (1950). On the adiabatic theorem of quantum mechanics. *Journal of Physical Society of Japan*, 5(6):435–439.

Khemani, V. and Nandkishore, R. (2019). Local constraints can globally shatter hilbert space: a new route to quantum information protection. *arXiv preprint arXiv:1904.04815*.

Knizhnik, V. G. and Zamolodchikov, A. B. (1984). *Nuclear Physics B*, 247:83–103.

Knysh, S. and Smelyanskiy, V. (2010). On the relevance of avoided crossings away from quantum critical point to the complexity of quantum adiabatic algorithm. *arXiv:1005.3011*.

Laflorencie, N., Affleck, I., and Berciu, M. (2005). *Journal of Statistical Mechanics*, page P12001.

Lake, B., Tennant, D. A., Frost, C. D., and Nagler, S. E. (2005). Quantum criticality and universal scaling of a quantum antiferromagnet. *Nature Materials*, 4(4):329.

Landau, L. D. (1937). On the theory of phase transitions. *Ukrainian Journal of Physics*, 11:19–32.

Laumann, C. R., Moessner, R., Scardicchio, A., and Sondhi, S. L. (2012). Quantum adiabatic algorithm and scaling of gaps at first-order quantum phase transitions. *Physical Review Letters*, 109(3):030502.

Léonard, F. and Delamotte, B. (2015). Critical exponents can be different on the two sides of a transition: A generic mechanism. *Physical Review Letters*, 115(20):200601.

Liang, S., Doucot, B., and Anderson, P. W. (1988). *Physical Review Letters*, 61:365.

Lin, Y.-C., Tang, Y., Lou, J., and Sandvik, A. W. (2012). *Physical Review B*, 86:144405.

Liu, C.-W., Polkovnikov, A., and Sandvik, A. W. (2013). Quasi-adiabatic quantum monte carlo algorithm for quantum evolution in imaginary time. *Physical Review B*, 87(17):174302.

Lou, J., Sandvik, A. W., and Balents, L. (2007). Emergence of u (1) symmetry in the 3d x y model with z q anisotropy. *Physical Review Letters*, 99(20):207203.

Luck, J. M. (1985). *Physical Review B*, 31:3069.

Nahum, A., Serna, P., Chalker, J., Ortuño, M., and Somoza, A. (2015). Emergent so (5) symmetry at the néel to valence-bond-solid transition. *Physical Review Letters*, 115(26):267203.

Newman, M. and Barkema, G. (1999). *Monte carlo methods in statistical physics chapter 1-4*. Oxford University Press: New York, USA.

Oshikawa, M. (2000). Ordered phase and scaling in z n models and the three-state antiferromagnetic potts model in three dimensions. *Physical Review B*, 61(5):3430.

Patil, P., Dasgupta, I., and Damle, K. (2014). *Physical Review B*, 90:245121.

Pfeuty, P. (1970). The one-dimensional ising model with a transverse field. *Annals of Physics*, 57(1):79–90.

Ricci-Tersenghi, F. (2010). Being Glassy Without Being Hard to Solve. *Science*, 330(6011):1639–1640.

Ricci-Tersenghi, F., Weigt, M., and Zecchina, R. (2001). Simplest random K-satisfiability problem. *Physical Review E*, 63(2):026702.

Sala, P., Rakovszky, T., Verresen, R., Knap, M., and Pollmann, F. (2019). Ergodicity-breaking arising from hilbert space fragmentation in dipole-conserving hamiltonians. *arXiv preprint arXiv:1904.04266*.

Sándor, C. (2004). Partitions of natural numbers and their representation functions. *Integers*, 4:A18.

Sandvik, A. W. (1999). Stochastic series expansion method with operator-loop update. *Physical Review B*, 59(22):R14157.

Sandvik, A. W. (2003). Stochastic series expansion method for quantum ising models with arbitrary interactions. *Physical Review E*, 68(5):056701.

Sandvik, A. W. (2006). Quantum criticality and percolation in dimer-diluted two-dimensional antiferromagnets. *Physical Review Letters*, 96(20):207201.

Sandvik, A. W. (2010a). *Physical Review Letters*, 104:137204.

Sandvik, A. W. (2010b). Computational studies of quantum spin systems. In *AIP Conference Proceedings*, volume 1297, pages 135–338. AIP.

Sandvik, A. W. and Evertz, H. G. (2010). *Physical Review B*, 82:024407.

Sanyal, S., Banerjee, A., and Damle, K. (2011). *Physical Review B*, 84(23):235129.

Senthil, T., Balents, L., Sachdev, S., Vishwanath, A., and Fisher, M. P. (2004). Quantum criticality beyond the landau-ginzburg-wilson paradigm. *Physical Review B*, 70(14):144407.

Senthil, T. and Sachdev, S. (1996). Higher dimensional realizations of activated dynamic scaling at random quantum transitions. *Physical Review Letters*, 77(26):5292.

Shao, H., Guo, W., and Sandvik, A. W. (2016). Quantum criticality with two length scales. *Science*, 352(6282):213–216.

Shao, H., Guo, W., and Sandvik, A. W. (2019). Monte carlo renormalization flows in the space of relevant and irrelevant operators: Application to three-dimensional clock models. *arXiv preprint arXiv:1905.13640*.

Sikora, O., Shannon, N., Pollmann, F., Penc, K., and Fulde, P. (2011). Extended quantum u (1)-liquid phase in a three-dimensional quantum dimer model. *Physical Review B*, 84(11):115129.

Sondhi, S. L., Girvin, S. M., Carini, J. P., and Shahar, D. (1997). Continuous quantum phase transitions. *Review of Modern Physics*, 69(1):315.

Suzuki, M. (1976). Generalized trotter's formula and systematic approximants of exponential operators and inner derivations with applications to many-body problems. *Communications in Mathematical Physics*, 51(2):183–190.

Suzuki, S., Inoue, J.-i., and Chakrabarti, B. K. (2012). *Quantum Ising phases and transitions in transverse Ising models*, volume 862. Springer.

Takahashi, J. and Hukushima, K. (2019). Phase transitions in quantum annealing of an np-hard problem detected by fidelity susceptibility. *Journal of Statistical Mechanics: Theory and Experiment*, 2019(4):043102.

Tang, Y. and Sandvik, A. W. (2011). *Physical Review Letters*, 107:157201.

Tsvelik, A. M. (2007). *Quantum field theory in condensed matter physics*. Cambridge university press.

Wang, C., Nahum, A., Metlitski, M. A., Xu, C., and Senthil, T. (2017). Deconfined quantum critical points: symmetries and dualities. *Physical Review X*, 7(3):031051.

Wannier, G. H. (1965). Probability of violation of the ehrenfest principle in fast passage. *Physics*, 1(5):251.

Wilson, K. G. (1971). Renormalization group and critical phenomena. i. renormalization group and the kadanoff scaling picture. *Physical Review B*, 4(9):3174.

Wu, F., Rollet, G., Huang, H., Maillard, J., Hu, C.-K., and Chen, C.-N. (1996). Directed compact lattice animals, restricted partitions of an integer, and the infinite-state potts model. *Physical Review Letters*, 76(2):173.

Xavier, J. C. and Alcaraz, F. C. (2012). *Physical Review B*, 85:024418.

Yang, Y. (2013). Polynomial curve fitting and lagrange interpolation. *Mathematics and Computer Education*, 47(3):224.

Zhang, L., Kourtis, S., Chamon, C., Mucciolo, E. R., and Ruckenstein, A. E. (2018). Ultra-slow dynamics in a translationally invariant spin model for multiplication and factorization. *preprint arXiv:1812.01621*.

Zhao, Y., Narayanan, R., and Cho, J. (2019). Signatures of many-body localization and metastability by weak perturbation. *arXiv preprint arXiv:1906.12020*.

CURRICULUM VITAE